CHAPTER 4

RESULTS AND DISCUSSION

Our previous study [10] have indicated that the flow characteristics associated with the air jet impinging onto the heated disk confined in the cylindrical space under investigation are relatively sensitive to the three relevant parameters—the jet inertia, buoyancy force due to the heated disk, and jet-to-disk separation distance. Thus some new vortex flow structures may appear when the experiment is conducted at wider range of the parameters. In the present experiment the air flow rate Q_j is varied from 0 to 12.0 slpm (standard liter per minute) and the temperature difference between the heated plate and injection air ΔT is varied from 0 to 25.0℃ for three jet-to-disk separation distances with H=10.0, 20.0 and 30.0 mm. The dimensionless groups governing the flow are the jet Reynolds number and the Rayleigh number. They are respectively defined as

$$\mathrm{Re}_j = \frac{V_j D_j}{\nu} = \frac{4}{\pi}\frac{Q_j}{\nu D_j} \tag{4.1}$$

$$\mathrm{Ra} = \frac{g\beta\Delta T H^3}{\alpha\nu} \tag{4.2}$$

The Grashof number is defined as

$$\mathrm{Gr} = \frac{g\beta\Delta T H^3}{\nu^2} \tag{4.3}$$

Thus the jet Reynolds number ranges from 0 to 1,623, the Rayleigh number from 0 to 63,420 and the Grashof number from 0 to 90,600. In what follows selected results from this study are presented to illustrate the possible existence of new vortex rolls and new time-dependent vortex flow patterns. Attention will be focused on the conditions leading to these new vortex flow structures and their characteristics affected by the governing diameters resulting from the air impinging jet in the processing chamber. The side view flow photos are taken at various cross planes to

obtain the possible circumferential variation of the vortex flow patterns. Meanwhile the top view flow photos are taken at the middle horizontal plane between the injection pipe exit and the upper surface of the heated disk to delineate the complete structure of the vortex flow.

4.1 New Steady Vortex Flow Pattern

At first, the typical steady vortex flow pattern observed in the cylindrical chamber with a larger jet-to-disk separation distance for H=30.0 mm for the case with a low buoyancy-to-inertia ratio Gr/Re_j^2 is illustrated in Fig. 4.1. The steady flow photos from the top and side view are shown along with the corresponding schematically sketched vortex flow pattern from the side view to indicate the actual direction of the flow recirculation, which is based on the detailed flow visualization. Since the flow is axisymmetric at this low buoyancy-to-inertia ratio (Re_j=270, Ra=63,420 and $Gr/Re_j^2 = 1.24$), only a half of the top view photo and the side view flow photo at the vertical plane $\theta = 0^o$ & 180^o are given here. The results indicate that only two circular vortex rolls are induced in the chamber. The inner circular roll directly surrounds the downward air jet and the outer circular roll is bigger and occupies the outer region of the chamber. They are in close contact. A close inspection of the successive top and side view flow photos in the video tapes taken during the transient stage of the flow formation reveals that immediately after the impinging, the jet is deflected by the heated disk to move obliquely upwards. Then, the oblique flow is divided into two streams as it encounters the chamber top. One stream moves radially inwards towards the low pressure region created by the viscous shearing of the surrounding fluid associated with the jet injection forming the inner roll, which is therefore considered as the inertia-driven or shear-driven vortex roll. Another stream

moves radially outwards along the chamber top, later turns to move downwards along the sidewall of chamber, and finally leaves the chamber through the outlets in the chamber bottom. Moreover, the outer roll near the chamber side is driven by the buoyancy force associated with the heated disk and is regarded as the buoyancy-induced roll. Note that at this larger jet-to-disk separation distance for H=30.0 mm both rolls are larger, no room is available for the appearance of the secondary inertia-driven roll which is often seen for H=20.0 and 10.0 mm at high Re_j.

Then, the typical steady vortex flow pattern at somewhat higher jet Reynolds number observed in the cylindrical chamber for the smaller jet-to-disk separation distances at H=20.0 and 10.0 mm are respectively shown in Figs. 4.2 and 4.3. The flow is also axisymmetric at this low buoyancy-to-inertia ratio with H=20.0 mm (Re_j=784, Ra=3,760 and $Gr/Re_j^2 = 8.74\times10^{-3}$) and H=10.0 mm ($Re_j$=1,150, Ra=470 and $Gr/Re_j^2 = 5.08\times10^{-4}$), and only the side view flow photos at the vertical plane $\theta = 0^o$ are given here. The results indicate that at this higher Re_j four circular vortex rolls are induced in the chamber for H=20.0 mm (Fig. 4.2), namely, the three inertia-driven and one buoyancy-driven rolls. More complete information on the characteristics of the primary inertia-driven roll, secondary inertia-driven roll and buoyancy-driven roll from the confined impinging gas jet at lower Re_j are already available from our previous study [10] and is not repeated here. The small tertiary circular roll above the large inner roll and adjacent to the chamber top is found to be induced through the viscous shearing effects produced by the strong inner vortex roll at high Re_j, which is termed as the tertiary inertia-driven roll. The tertiary roll was not reported in the literature. It should be observed that at H=20.0 mm the tertiary inertia-driven roll is induced only when the jet Reynolds number exceeds certain level around 676 when the disk is unheated with Ra=0. We further note from the results in

Fig. 4.3 for H=10.0 mm that five circular vortex rolls are induced in the chamber at the much higher Re_j of 1,150. More specifically, in addition to the primary, secondary and tertiary inertia-driven rolls and the buoyancy-induced roll, a quaternary roll appears near the top of the chamber. This roll is small and weak and found to result from viscous shearing effects produced by the relatively strong inner vortex roll at the very high Re_j, which is termed as the quaternary inertia-driven roll. Moreover, at H=10.0 mm the quaternary inertia-driven roll is induced only when the jet Reynolds number exceeds certain level around 1,014 for the unheated disk with Ra=0. Besides, a higher Re_j is needed for the onset of the tertiary inertia-driven roll in the chamber with the smaller H of 10.0 mm (Re_j=744 at Ra=0) when compared with that for H=20.0 mm.

The effects of the jet Reynolds number and Rayleigh number on the characteristics of the tertiary and quaternary inertia-driven rolls are examined next. The results shown in Figs. 4.4 and 4.5 indicate that both tertiary and quaternary rolls grow slightly in size at increasing Re_j, similar to primary and secondary rolls. However, Fig. 4.6 shows the significant decay of the tertiary roll at increasing Ra for Re_j=771 and H=20.0 mm. Note that at Ra=11,280 ($\Delta T = 15.0$℃) and H=20.0 mm the tertiary roll nearly disappears and at the higher Ra of 15,030 and 18,790 no tertiary roll is detected in the flow. The situation is somewhat different for the smaller H of 10.0 mm. Typical results given in Fig. 4.7 show that for H=10.0 mm the tertiary roll is only slightly affected by the Rayleigh number. But the decay of the quaternary roll with Ra is noticeable.

4.2 Onset of Vortex Rolls

The understanding of the critical conditions for the appearance of the tertiary and quaternary inertia-driven vortex rolls and the unsteady flow in the chamber are of

fundamental interest in the fluid flow study. The onset of the inertia-driven rolls and inertia-driven time-dependent flow is ascertained by carefully visualizing the flow in the processing chamber at increasing jet Reynolds number. The results suggest that as the jet Reynolds number exceeds certain higher levels the tertiary and quaternary inertia-driven vortex rolls and the inertia-driven time-dependent flow appear. More specifically, at increasing jet Reynolds number for given H and ΔT the primary, secondary, tertiary and the quaternary inertia-driven rolls appear in sequence, as evident from the data summarized in Table 4.1. So the quaternary inertia-driven roll is initiated at a higher Reynolds number than the other rolls. For a higher ΔT a higher Re_j is required to initiate the tertiary or quaternary roll. When the jet-to-disk separation distance is reduced, we also need a higher Re_j to initiate the inertia-driven rolls. It should be mentioned that for the range of the parameters covered here the quaternary inertia-driven roll does not appear at H=20.0 and 30.0 mm. Besides, at H=30.0 mm the tertiary inertia-driven roll only appears when $\Delta T = 0$℃.

Besides, according to Table 4.1 we can have different vortex flow patterns based on the number of rolls in the chamber. The flow regime map is shown in Fig. 4.8 in terms of the parameters chosen as $Ra(D_j/H)^{2.7}$ vs. $Re_j(D_j/H)^{-0.14}$. The results in this plot manifest that when the jet Reynolds number Re_j and/or the aspect ratio of the processing chamber D_j/H are high so that $Re_j(D_j/H)^{-0.14} \geq 1200$, the buoyancy-to-inertia ratio in the flow is low for the range of the Rayleigh number considered here and we find that the flow consisting of four inertia- and buoyancy-driven rolls. But when $Re_j(D_j/H)^{-0.14}$ is between 800 and 1000, the flow becomes three inertia- and buoyancy-driven rolls. Finally, for a high buoyancy-to-inertia ratio the flow shows two inertia- and buoyancy-driven rolls. More specifically, the boundary between two inertia-driven rolls and three inertia-driven

rolls for H=10.0 mm can be correlated as

$$\mathrm{Ra}\times\left(\frac{\mathrm{D_j}}{\mathrm{H}}\right)^{2.7}=-13416+18.2082\left[\mathrm{Re_j}\times\left(\frac{\mathrm{D_j}}{\mathrm{H}}\right)^{-0.14}\right] \tag{4.4}$$

The transitions from three inertia-driven rolls to four inertia-driven rolls occurs as

$$\mathrm{Ra}\times\left(\frac{\mathrm{D_j}}{\mathrm{H}}\right)^{2.7}=-16430+16.1048\left[\mathrm{Re_j}\times\left(\frac{\mathrm{D_j}}{\mathrm{H}}\right)^{-0.14}\right] \tag{4.5}$$

These two correlations (Equations (4.4) and (4.5)) are also shown in Fig. 4.8.

4.3 Instability of Vortex Flow

For the ranges of the parameters covered in the present study two types of vortex flow instability are identified. At a sufficiently high jet Reynolds number beyond the critical $\mathrm{Re_j}$ for the onset of the secondary, tertiary or quaternary roll depending on the jet-to-disk separation distance, the vortex flow does not reach any steady state at long time and in fact it becomes time-dependent. This is an inertia-driven flow instability. The flow experiences another instability when the buoyancy predominates over the inertia at a high buoyancy-to-inertia ratio $\mathrm{Gr}/\mathrm{Re_j}^2$. Obviously, this is a buoyancy-driven flow instability. In the experiment the critical conditions for the onsets of these two instabilities are obtained from inspecting a number of vedio tapes recording the time evolution of the vortex flow patterns from the side and top view for given H and ΔT at a small step increase of $\mathrm{Q_j}$ of 0.1 slpm.

The present data for the critical $\mathrm{Re_j}$ for the onset of the inertia-driven time-dependent flow for various H and ΔT are summarized in Table 4.2. Note that the critical $\mathrm{Re_j}$ increases slightly with ΔT for H=10.0 & 20.0 mm. While for the higher H of 30.0 mm an opposite trend is noted. This opposite trend results from the fact that for H=30.0 mm at given $\mathrm{Q_j}$ and ΔT, the inertia- and buoyancy-driven rolls

are in close contact such as that shown in Fig. 4.1. An increase in ΔT first causes the buoyancy-driven roll to grow, which in turn squeezes the inertia-driven roll. Then the inertia-driven roll pushes back. These two mechanisms result in the cyclic growth and decay of the two rolls and the vortex flow becomes unsteady. For a higher ΔT the buoyancy roll is bigger and the inertia-driven roll starts to push the bigger buoyancy roll at a lower Re_j. Thus at the higher H of 30.0 mm the critical Re_j is lower for a higher ΔT. While for the smaller H of 10.0 and 20.0 mm the inertia- and buoyancy-driven rolls are much smaller (Figs. 4.2-4.7). They are not in close contact and the squeezing and pushing mechanisms between the rolls do not exist. Note that the onset condition of the circumferential rotation of the deformed vortex rolls is the same as that for the onset of time-periodic flow given in Table 4.2. But at H=10.0 mm the deformed vortex rolls do not rotate circumferentially.

The present data for the vortex flow instability indicate that for the small H of 10.0 mm and large H of 30.0 mm the buoyancy-driven flow instability does not exist for all cases studied here. This unusual result requires some explanation. First, we note that the Rayleigh number is proportional to H^3 according to Equ. (4.2). Hence at H=10.0 mm the Rayleigh number (=2,350) is still low even for the highest ΔT (=25.0℃) tested in the present study. Apparently, this low Ra can not trigger flow instability. Now for H=30.0 mm the Rayleigh number (=63,420) is relatively high for $\Delta T = 25.0$ ℃. The buoyancy-driven roll is very large for this case. But it is rather stable even for the lowest Re_j tested with Q_j=0 slpm (Re_j=0), the pure natural convection case. Figure 4.9 shows that at Re_j=0 and $\Delta T = 25.0$ ℃ the chamber is completely filled with the buoyancy-driven roll for H=30.0 mm. Even for the higher H of 45.0 mm the buoyancy-driven roll is stable too (Fig. 4.9 (b)). A rise in Re_j causes the inertia-driven roll to grow and the buoyancy-driven to decay. But they are still in stable condition.

Finally, our data show that the buoyancy-driven instability does exist in the flow for H=20.0 mm when the buoyancy-to-inertia ratio is high. At this intermediate H the inertia- and buoyancy-driven rolls do not contact and some free space between the two rolls is available for the new buoyancy-driven rolls to be induced at certain high buoyancy-to-inertia ratio. These new rolls are undergoing growth, decay, disappearance and generation processes as the flow evolves. The characteristics of this buoyancy-driven time-dependent flow have been reported in the previous study [10].

4.4 Inertia-Driven Time-Dependent Vortex Flow

The characteristics of the inertia-driven vortex flow at supercritical jet Reynolds numbers are examined here. We first note that in the chamber with a small H of 10.0 mm the unsteady vortex flow at a supercritical Re_j is characterized by a small amplitude oscillation of the downstream tip of the primary inertia-driven roll near the chamber top. The portion of the secondary inertia-driven roll near this tip is also in slight oscillation. This region is indicated in the side view flow photos given in Fig. 4.10 for various Ra at Re_j=1,190. This slight unsteady flow oscillation distorts the downstream boundary of the primary roll to a certain degree, as evident from the top view flow photos given in Fig. 4.11. Note that the tertiary and quaternary rolls are not seen in Fig. 4.11 simply because they are small and close to the chamber top and cannot be captured by the top view photos taken at the middle horizontal plane. It is also observed from Fig. 4.10 that at H=10.0 mm the buoyancy-driven roll is rather small owing to the small Ra mentioned above.

For the larger H of 20.0 mm and at a supercritical Re_j, slight radial growth of the primary inertia-driven roll accompanying slight decay of the secondary inertia-driven roll takes place in a certain period of time near the inter-boundary between the two

rolls for $\Delta T = 0$℃ (Fig. 4.12). In the subsequent period of time the reverse process occurs with the growth of the secondary roll and the decay of the primary roll. The flow is thus time dependent. The deformed boundary now can be more clearly seen from the top view flow photo (Fig. 4.12(b)). Moreover, at this H the primary and secondary rolls are found to rotate in the same circumferential direction. This circumferential rotation of the rolls is found to result from the high jet inertia associated with a high Re_j. At the high ΔT of 25.0℃ Fig. 4.13 shows that the secondary roll merges with buoyancy-driven roll to form a big roll in the outer region of the chamber. This has been examined in our earlier study for a higher Re_j [10]. The cyclic growth and decay of the primary and the merged rolls around their inter-boundary are also seen for the case shown in Fig. 4.13. It should be mentioned that the time-dependent vortex flows shown in Figs. 4.12 and 4.13 are both axisymmetric essentially.

As the jet-to-disk separation distance is increased to 30.0 mm, the inertia-driven time-dependent vortex flow is dominated by the growth of the primary inertia-driven roll accompanying with the squeezing of the buoyancy-driven roll in the first half of a typical period, followed with a reverse process in the second half of the period. At this higher H the circumferential rotation of the two rolls is more significant. These unique features of the unsteady flow are shown in Figs. 4.14-4.18 for selected Q_j and ΔT. Note that the time-dependent flow shown in Fig. 4.17 begins to exhibit slight asymmetry in the vortex rolls at certain high buoyancy-to-inertia ratio. And the flow becomes more asymmetric for a higher Gr/Re_j^2 such as those presented in Figs. 4.19 and 4.20. Besides, at a higher Gr/Re_j^2 the rolls suffer from a move severe distortion. In fact, at this high buoyancy-to-inertia ratio the primary inertia-driven roll splits into a number of vortices, as schematically illustrated in Fig. 4.21. These

vortices also rotate circumferentially with the buoyancy-driven roll.

In addition to those presented above, a very important characteristic of the inertia-driven time-dependent vortex flow is shown in Fig. 4.22. It manifests that in the inertia-driven unsteady flow the dividing stream between the primary and buoyancy rolls, which directly comes from the jet injected into the chamber from the injection pipe exit, experiences a significant change in the flow direction with time. Sometime it is divided into two streams when it encounters the chamber top, as noted in the side flow photo at t=0.4 sec. One stream moves inwards to the jet axis and another move outwards to the side wall of the chamber. The other time it first moves towards the jet axis and then turns back and moves towards the chamber side, such as that at t=0 & 0.2 sec. Still the other time it moves towards the chamber side, for instance at t=0.6~1.6 sec.

The characteristics of the inertia-driven time-dependent flow are further illustrated by examining the data from the transient temperature measurement. First, it is noted that at H=10.0 and 20.0 mm the amplitude of the flow oscillation for the range of supercritical Re_j covered in this study is small. Hence the temperature oscillation in the flow is also very small and in fact it is at the same order of magnitude as the background disturbances. But for the high H of 30.0 mm the temperature oscillation can be significant. The time records of the nondimensional air temperature Φ defined as $(T-T_j)/(T_f-T_j)$ at selected locations for the case with Re_j=676 and Ra=63,420 are shown in Fig. 4.23. Note that the amplitude of the temperature oscillation varies substantially with the locations. More specifically, in the upper region of the chamber the air temperature oscillates in a larger amplitude (Fig. 4.23(c)), except in the side wall region. Elsewhere in the lower half of the chamber the temperature oscillation is rather small and its amplitude is very close to

the background disturbances (Figs. 4.23(a) and (b)). Similar results are obtained for other cases shown in Figs. 4.24 and 4.25. Moreover, Figs. 4.26-4.28 show that the frequency of the temperature oscillation is mainly affected by the jet Reynolds number. The Rayleigh number only exhibits a very slight effect. More precisely, the oscillation frequency increases with Re_j. The evolutions of the inertia-driven time periodic flow in a typical periodic cycle for selected cases are illustrated in Figs. 4.29-4.42. The mutual pushing and squeezing of the two rolls in the chamber are clearly seen. The size change of the rolls with time is noticeable according to the side view flow photos. Moreover, the mutual interaction of the rolls causes the vortex flow inside the rolls to become somewhat irregular, as evident from the top view flow photos. This vortex flow irregularity is more pronounced at a higher buoyancy-to-inertia ratio.

Finally, the effects of the Rayleigh number on the inertia-driven time-dependent flow require some further discussion. First, we already knew that for the small H of 10.0 and 20.0 mm the critical Re_j for the onset of the inertia-driven time-dependent flow is higher for a higher ΔT (Table 4.2). This suggests that an increase in ΔT can stabilize the inertia-driven time-dependent flow. It is important to elucidate why the inertia-driven time-dependent flow can be stabilized by raising the ΔT. A close inspection of the vortex flow at supercritical Re_j for various ΔT reveals that the buoyancy-driven roll is bigger and stronger at increasing ΔT. As the buoyancy-driven roll grows to a certain large size, it merges with the secondary inertia-driven roll and the larger merged roll is in close contact with the inertia-driven rolls and can retard the oscillation of the inertia rolls. Thus the time-dependent flow is stabilized. This is illustrated in Figs. 4.43 and 4.44 for H=20.0 mm at Q_j=6.5 slpm. Note that at $\Delta T = 0$ & 5.0℃ the flow is time periodic. But at the higher $\Delta T \geq 10.0$ ℃ steady flow prevails in the chamber. Next, an opposite trend is noted for the large

H of 30.0 mm (Table 4.2). At this high H both the inertia- and buoyancy-driven rolls are relatively large for given Re_j and ΔT (≥ 5.0℃). An increase in ΔT causes the buoyancy rolls to push and squeeze the inertia roll. The inertia roll then pushes back and initiates flow unsteadiness. This is shown is Figs. 4.45 and 4.46.

We also note that at the jet Reynolds number well above that for the onset of the inertia-driven time periodic flow listed in Table 4.2 the flow is no longer time periodic. The critical Re_j for the onset of the inertia-driven nonperiodic flow is also located in the present experiment. The results are given in Table 4.3. For H=10.0 & 20.0 mm this critical Re_j again increases with ΔT . But for the larger H of 30.0 mm an opposite trend is also noted. Selected results for this nonperiodic flow are shown in Figs. 4.47-4.55. The top view flow photos and the time records of the air temperature (Figs. 4.54 and 4.55) clearly illustrate the severe irregularity of the vortex flow at these high Re_j. The flow oscillation is very strong.

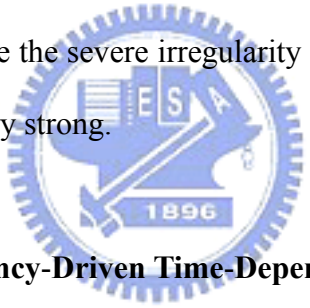

4.5 Characteristics of Buoyancy-Driven Time-Dependent Flow

It is observed in the present experiment that only for H=20.0 mm the vortex flow in the processing chamber does not reach steady state at long time when the buoyancy-to-inertia ratio Gr/Re_j^2 is raised to certain high level and the vortex flow gradually becomes time dependent. As mentioned earlier, at H=10.0 & 30.0 mm the buoyancy driven flow instability does not exist over the ranges of the parameters covered here. The characteristics of a typical time periodic vortex flow is demonstrated in Fig. 4.56 by showing selected cross plane flow photos at certain time instants and time records of air temperature at selected locations in the processing chamber in the statistical state for H=20.0 mm. The result clearly shows that two additional circular rolls are induced in the time periodic vortex flow. These two new

rolls are smaller and appear in the middle potion of the chamber right between the inner and outer rolls. It is noted that the time periodic vortex flow is slightly asymmetric. The data for the time records given in Fig. 4.56 indicate that only in the region dominated by the new rolls the air temperature oscillates significantly with time. The side view flow photos at the cross plane $\theta = 0°$ & $180°$ at selected time instants in a typical periodic cycle for the case with Re_j=135 and Ra=11,270 are shown in Fig. 4.57. This periodic flow evolution is similar to our previous study [10]. The evolution of the nonperiodic vortex flow at a higher buoyancy-to-inertia ratio Gr/Re_j^2 is illustrated in Fig. 4.58. The asymmetry in the flow is more pronounced. In fact, for this case the flow becomes quasi-periodic in time.

To further reveal the temporal characteristics of the time periodic vortex flow, the time records of the air temperature at a selected location and the corresponding power spectrum densities (PSD) are presented next in Fig. 4.59 for various Re_j at Ra=11,270. The PSD are evaluated from the Fourier analysis of the measured data. The results clearly manifest that the flow oscillates at a large amplitude and a slightly lower frequency for a lower Re_j at the fixed Ra. This trend is apparently owing to the accompanying rise in the buoyancy-to-inertia ration at reducing Re_j. Note that the time periodic flow prevails over a finite noticeable range of the jet Reynolds number (Figs. 4.59 (b)-(d)) and the flow oscillation is characterized by a single fundamental frequency. At certain low Re_j (high Gr/Re_j^2) the flow oscillation becomes nonperiodic in time (Fig. 4.59 (a)). When Re_j exceeds certain level, the flow becomes steady state in the chamber (Fig. 4.59 (e)).

Then, the effects of the Rayleigh number on the temporal characteristics of the time periodic vortex flow are illustrated in Fig. 4.60 by showing the time histories of the air temperature at a selected location for various Ra at fixed Re_j. Note that the

oscillation amplitude of the air temperature is only slightly affected by the variation in the Rayleigh number. This situation is the same as the effects of the Rayleigh number for inertia-driven time-dependent vortex flow.

4.6 Flow Regime Maps

Based on the present data, the flow regime maps delineating the temporal state of the inertia- and buoyancy-driven flow in the processing chamber are provided in Figs. 4.61-4.63 for various H. Note that at H=10.0 & 30.0 mm the buoyancy-driven unstable vortex flow do not exist. Besides, the inertia-driven time periodic vortex flow only exists in a very small region for H=10.0 mm. At H=20.0 mm both the inertia- and buoyancy-driven vortex flows instability take place. The buoyancy-driven unstable flow appears at very high buoyancy-to-inertia ratio (Fig. 4.62). The boundary between the stable vortex flow and the time periodic inertia-driven unstable vortex flow for H=10.0 mm can be correlated as

$$\mathrm{Ra} = -11{,}800 + 11.1\,\mathrm{Re}_j \tag{4.6}$$

for $0 \le \mathrm{Ra} \le 2{,}350$, $1{,}041 \le \mathrm{Re}_j \le 1{,}258$.

In addition, the transition from the time periodic inertia-driven vortex flow to the nonperiodic inertia-driven vortex flow occurs when

$$\mathrm{Ra} = -28{,}700 + 22.2\,\mathrm{Re}_j \tag{4.7}$$

for $0 \le \mathrm{Ra} \le 2{,}350$, $1{,}285 \le \mathrm{Re}_j \le 1{,}393$.

These two correlations are also shown in Fig. 4.61. The significant increase of the critical Ra with Re_j is clearly seen in the plot.

Next, the boundary between the nonperiodic buoyancy-induced vortex flow and the time periodic buoyancy-induced unstable vortex flow for H=20.0 mm can be

empirically correlated as

$$\mathrm{Ra} = 10{,}800 + 0.0568\,\mathrm{Re}_j^{\,2} \tag{4.8}$$

for $7{,}520 \le \mathrm{Ra} \le 18{,}790$, $189 \le \mathrm{Re}_j \le 379$.

The boundary between the time periodic buoyancy-induced unstable vortex flow and the stable vortex flow can be correlated as

$$\mathrm{Ra} = 4160 + 0.1\,\mathrm{Re}_j^{\,2} \tag{4.9}$$

for $11{,}270 \le \mathrm{Ra} \le 15{,}030$, $108 \le \mathrm{Re}_j \le 250$.

The transitions from the stable vortex flow to the time periodic inertia-driven vortex flow occurs as

$$\mathrm{Ra} = -74{,}300 + 92.6\,\mathrm{Re}_j \tag{4.10}$$

for $0 \le \mathrm{Ra} \le 18{,}790$, $798 \le \mathrm{Re}_j \le 987$.

The boundary between the time periodic inertia-driven vortex flow and the nonperiodic inertia-driven vortex flow can be correlated as

$$\mathrm{Ra} = -120{,}000 + 111.0\,\mathrm{Re}_j \tag{4.11}$$

for $0 \le \mathrm{Ra} \le 18{,}790$, $1{,}082 \le \mathrm{Re}_j \le 1{,}258$.

These four correlations are also indicated in Fig. 4.62.

Finally, the transitions from the stable vortex flow to the time periodic inertia-driven vortex flow for H=30.0 mm occurs as

$$\mathrm{Ra} = 102{,}000 - 0.149\,\mathrm{Re}_j^{\,2} \tag{4.12}$$

for $0 \le \mathrm{Ra} \le 63{,}420$, $473 \le \mathrm{Re}_j \le 788$.

The boundary between the time periodic inertia-driven vortex flow and the nonperiodic inertia-driven vortex flow can be correlated as

$$\mathrm{Ra} = 269{,}000 - 224.0\,\mathrm{Re}_j \qquad (4.13)$$

for $0 \le \mathrm{Ra} \le 63{,}420$, $947 \le \mathrm{Re}_j \le 1204$.

These two correlations are also shown in Fig. 4.63.

Finally, it is noted from the instability boundaries shown in Figs. 4.61-4.63 that the inertia-driven unstable flow at high Re_j for H=10.0 & 20.0 mm can be stabilized by increasing the buoyancy (ΔT). However, for H=30.0 mm a stable flow prevailed at low Re_j can be destabilized by an increase in ΔT due to the decrease of the critical Re_j at increasing ΔT (Fig. 4.63). We further note the simultaneous presence of the buoyancy- and inertia-driven flow instability in the chamber with H=20.0 mm. Thus for H=20.0 mm and a certain high ΔT the vortex flow can be time dependent at low Re_j resulting from the buoyancy-driven instability. For Re_j raised to some intermediate level, the buoyancy-to-inertia ratio is lower and the vortex flow is stable. But for a further increase of Re_j to a certain high level, the inertia-driven flow instability sets in and the flow becomes unstable. Hence for H=20.0 mm the vortex flow experiences a reverse flow transition at increasing Re_j. The changes of the vortex flow patterns at selected Re_j at which the reverse transition occurs are shown in Figs. 4.64 and 4.65. Obviously, at H=10.0 & 30.0 mm no reverse flow transition exists at increasing Re_j. The flow at a low Re_j is stable for all ΔT tested. At a supercritical Re_j for the onset of the inertia-driven instability the flow becomes unstable. The change in the vortex flow patterns at increasing Re_j for H=30.0 mm is illustrated in Fig. 4.66.

Table 4.1 Critical condition for appearance of the tertiary and quaternary inertia-driven rolls.

Vortex roll	Separation distance (H, mm)	Jet diameter (D_j, mm)	ΔT (℃)	Flowrate (Q_j, SLPM)	Gr	Ra	Re_j	Gr/Re_j^2
Tertiary inertia-driven roll	10.0	10.0	0	5.5	0	0	744	0
			5.0	5.6	670	470	757	0.0012
			10.0	5.8	1340	940	784	0.0022
			15.0	6.0	2010	1410	811	0.0031
			20.0	6.2	2680	1880	839	0.0038
			25.0	6.4	3360	2350	866	0.0045
	20.0	10.0	0	5.0	0	0	676	0
			5.0	5.2	5370	3760	703	0.0109
			10.0	5.4	10740	7520	730	0.0201
			15.0	5.6	16100	11270	757	0.0281
			20.0	5.8	21480	15030	784	0.0349
			25.0	6.0	26840	18790	811	0.0408
	30.0	10.0	0	4.6	0	0	622	0
Quaternary inertia-driven roll	10.0	10.0	0	7.5	0	0	1014	0
			5.0	7.8	670	470	1055	0.0048
			10.0	8.0	1340	940	1082	0.0092
			15.0	8.2	2010	1410	1109	0.0131
			20.0	8.4	2680	1880	1136	0.0166
			25.0	8.6	3360	2350	1163	0.0198

Table 4.2 Critical condition for onset of the inertia-driven time periodic flow for various H.

Separation distance (H, mm)	ΔT （℃）	Flowrate (Q_j, SLPM)	Re_j	Ra	Gr
10.0	0	7.7	1041	0	0
	5.0	8.6	1163	470	670
	10.0	8.6	1163	940	1340
	15.0	8.7	1177	1410	2010
	20.0	9.0	1217	1880	2680
	25.0	9.3	1258	2350	3360
20.0	0	5.9	798	0	0
	5.0	6.2	839	3760	5370
	10.0	6.6	893	7520	10740
	15.0	6.9	933	11270	16100
	20.0	7.2	974	15030	21480
	25.0	7.3	987	18790	26840
30.0	0	5.9	798	0	0
	5.0	5.7	771	12680	18120
	10.0	5.5	744	25370	36240
	15.0	5.0	676	38050	54360
	20.0	4.5	609	50730	72480
	25.0	3.5	473	63420	90600

Table 4.3 Critical condition for onset of the inertia-driven nonperiodic flow for various H.

Separation distance (H, mm)	ΔT (℃)	Flowrate (Q_j, SLPM)	Re_j	Ra	Gr
10.0	0	9.5	1285	0	0
	5.0	9.8	1325	470	670
	10.0	9.9	1339	940	1340
	15.0	10.0	1352	1410	2010
	20.0	10.2	1380	1880	2680
	25.0	10.3	1393	2350	3360
20.0	0	8.0	1082	0	0
	5.0	8.3	1123	3760	5370
	10.0	8.5	1150	7520	10740
	15.0	8.8	1190	11270	16100
	20.0	9.0	1217	15030	21480
	25.0	9.3	1258	18790	26840
30.0	0	8.9	1204	0	0
	5.0	8.4	1136	12680	18120
	10.0	7.9	1068	25370	36240
	15.0	7.4	1001	38050	54360
	20.0	7.1	960	50730	72480
	25.0	7.0	947	63420	90600

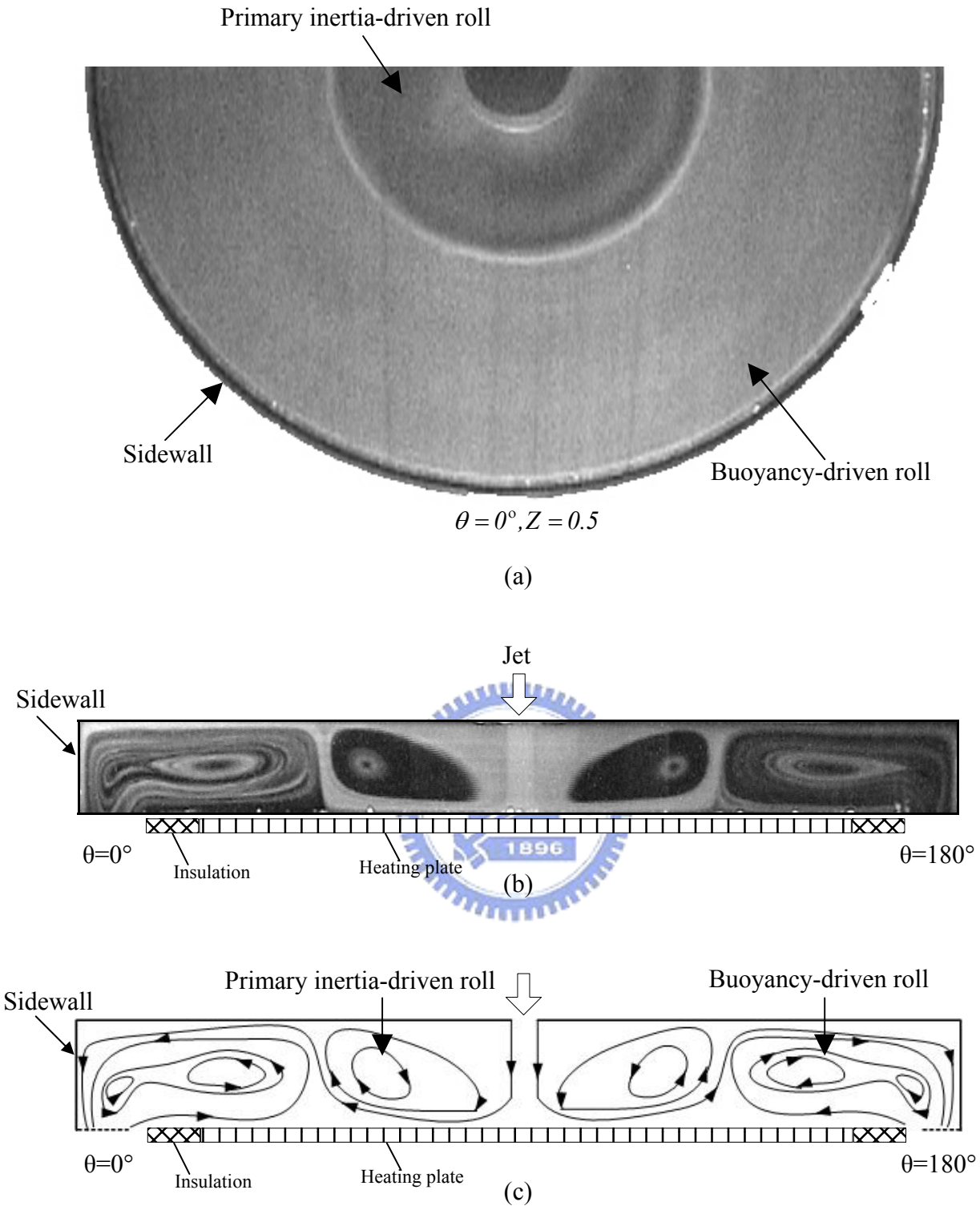

Fig. 4.1 Steady side view flow pattern in the chamber with H=30.0 mm for Re_j=270 (Q_j=2.0 slpm) and Ra=63,420 (ΔT = 25.0℃): (a)top view flow photo taken at middle horizontal plane halfway between the pipe exit and heated disk, (b) side view flow photo taken at the vertical plane $\theta = 0^o$ & $\theta = 180^o$ and (c) the corresponding schematically sketched cross plane vortex flow.

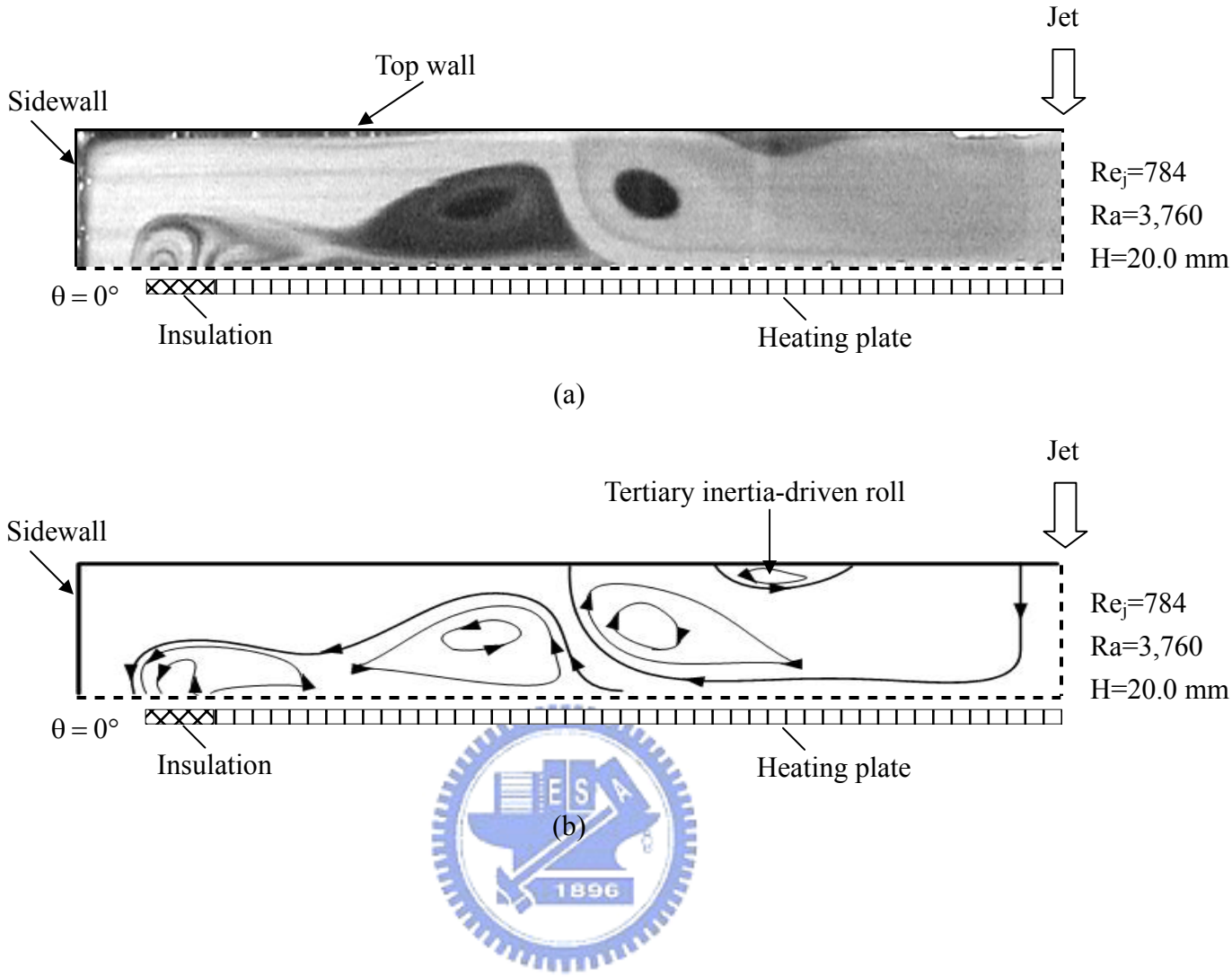

Fig. 4.2 Steady vortex flow pattern in the chamber with H=20.0 mm for Re_j=784 (Q_j=5.8 slpm) and Ra=3,760 ($\Delta T = 5.0$℃): (a) side view flow photo taken at the vertical plane $\theta = 0^o$ and (b) the corresponding schematically sketched cross plane vortex flow.

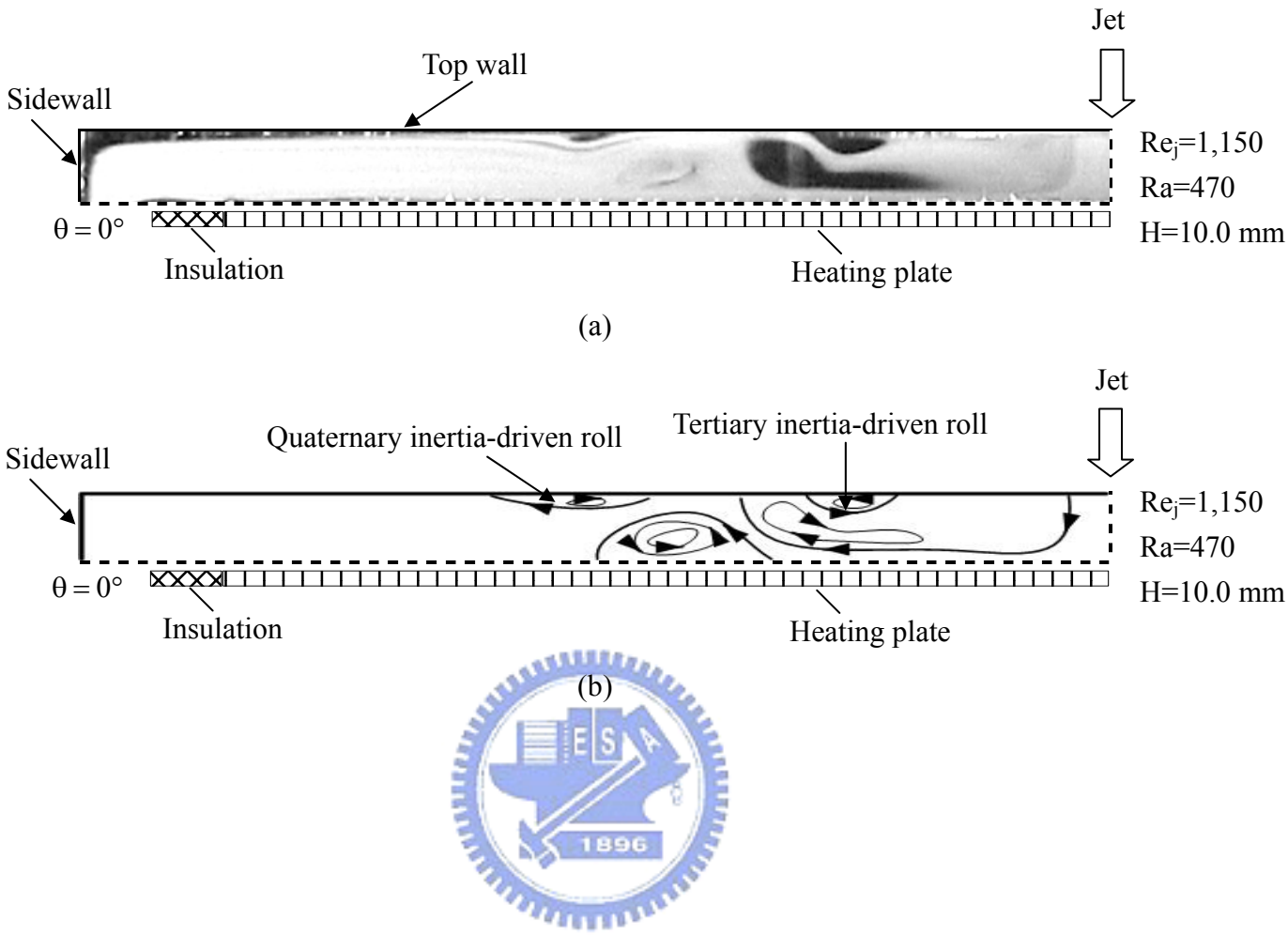

Fig. 4.3 Steady vortex flow pattern in the chamber with H=10.0 mm for Re_j=1,150 (Q_j=8.5 slpm) and Ra=470 ($\Delta T = 5.0$℃): (a) side view flow photo taken at the vertical plane $\theta = 0^o$ and (b) the corresponding schematically sketched cross plane vortex flow.

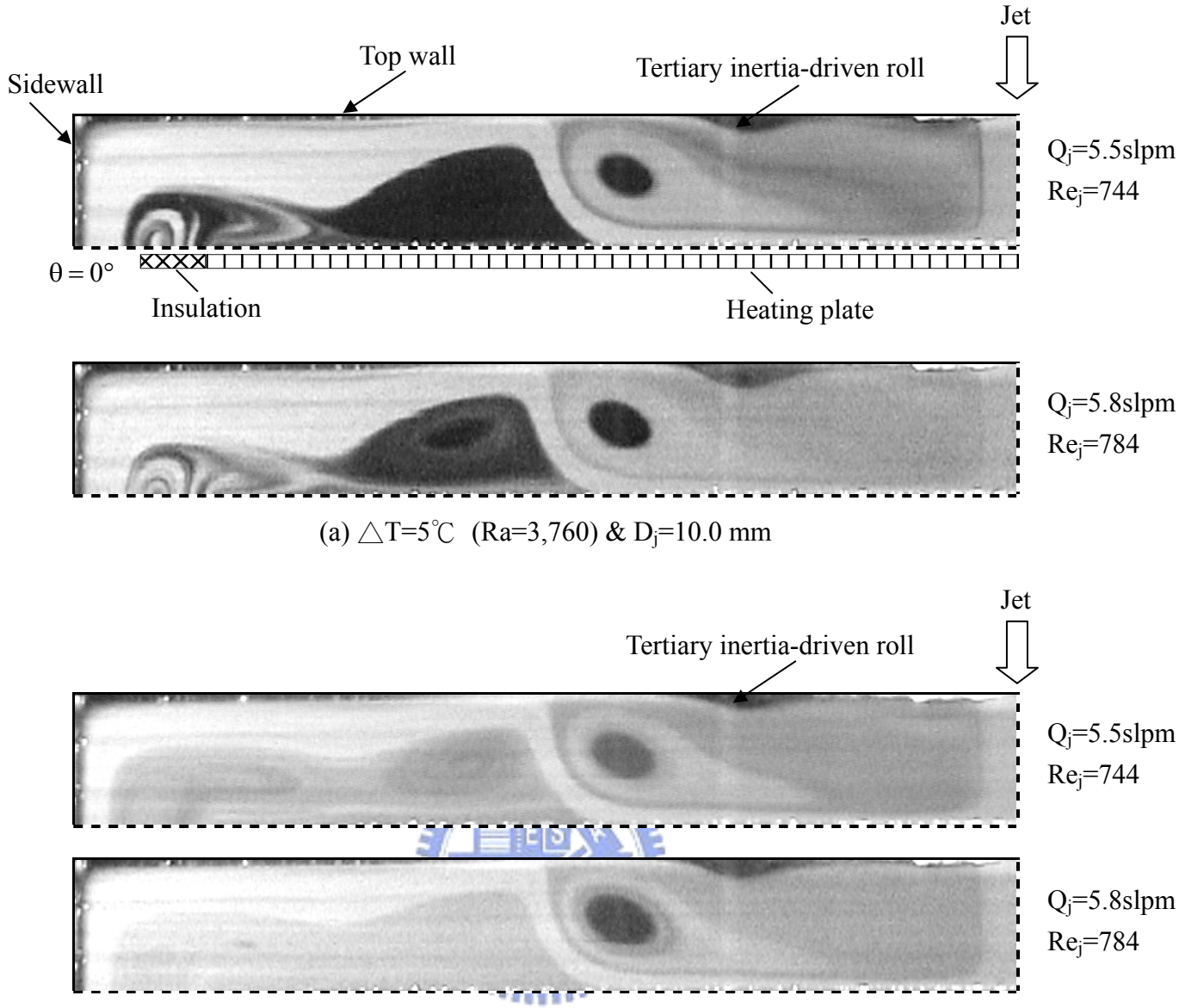

Fig. 4.4 Steady side view flow photos taken at the cross plane $\theta = 0°$ for various Reynolds numbers at H=20.0 mm for Ra= (a) 3,760 (△T=5.0℃) and (b) 7,520 (△T=10.0℃).

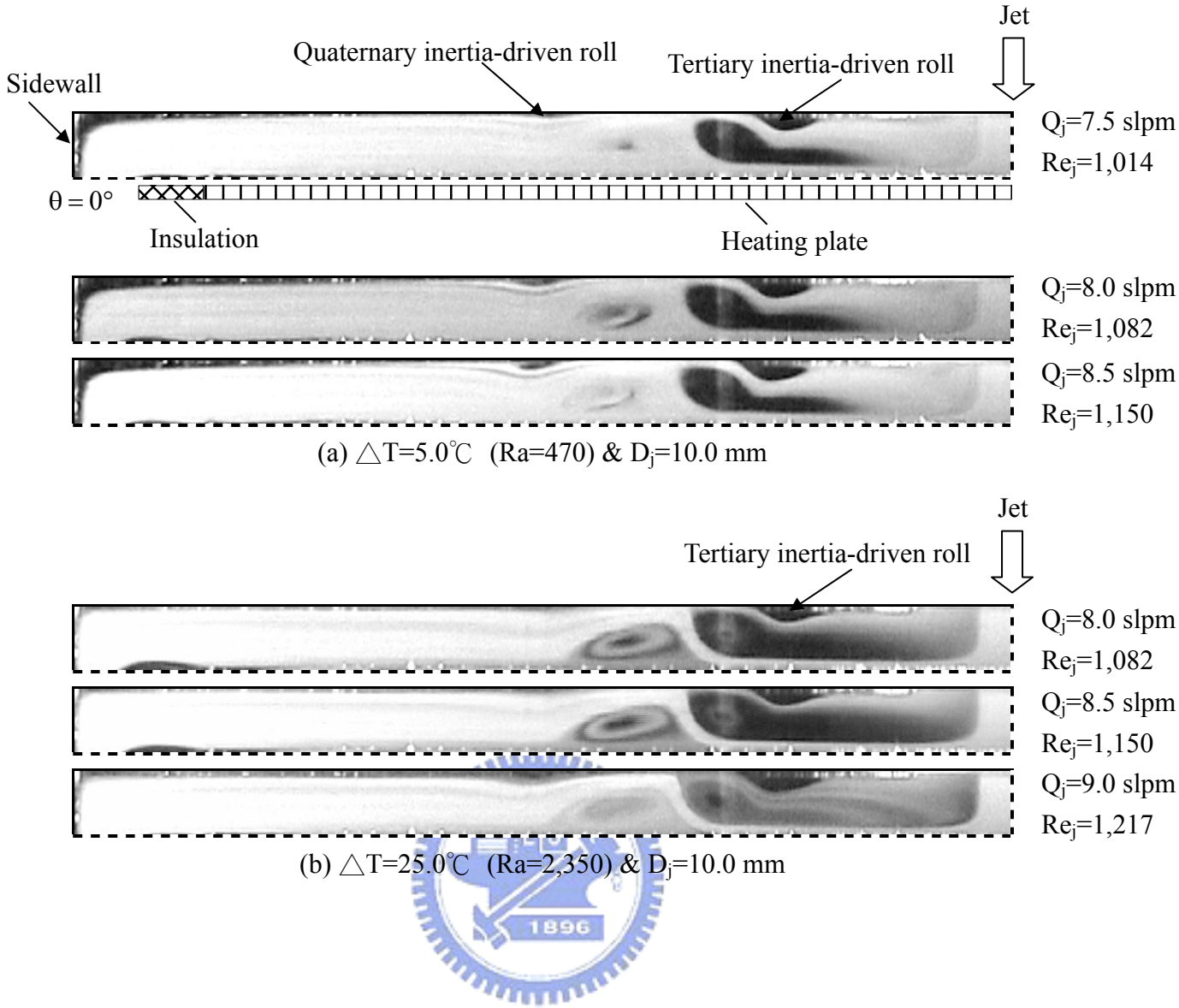

Fig. 4.5 Steady side view flow photos taken at the cross plane $\theta = 0°$ for various jet Reynolds numbers at H=10.0 mm for Ra= (a) 470 (△T=5.0℃) and (b) 2,350 (△T=25.0℃).

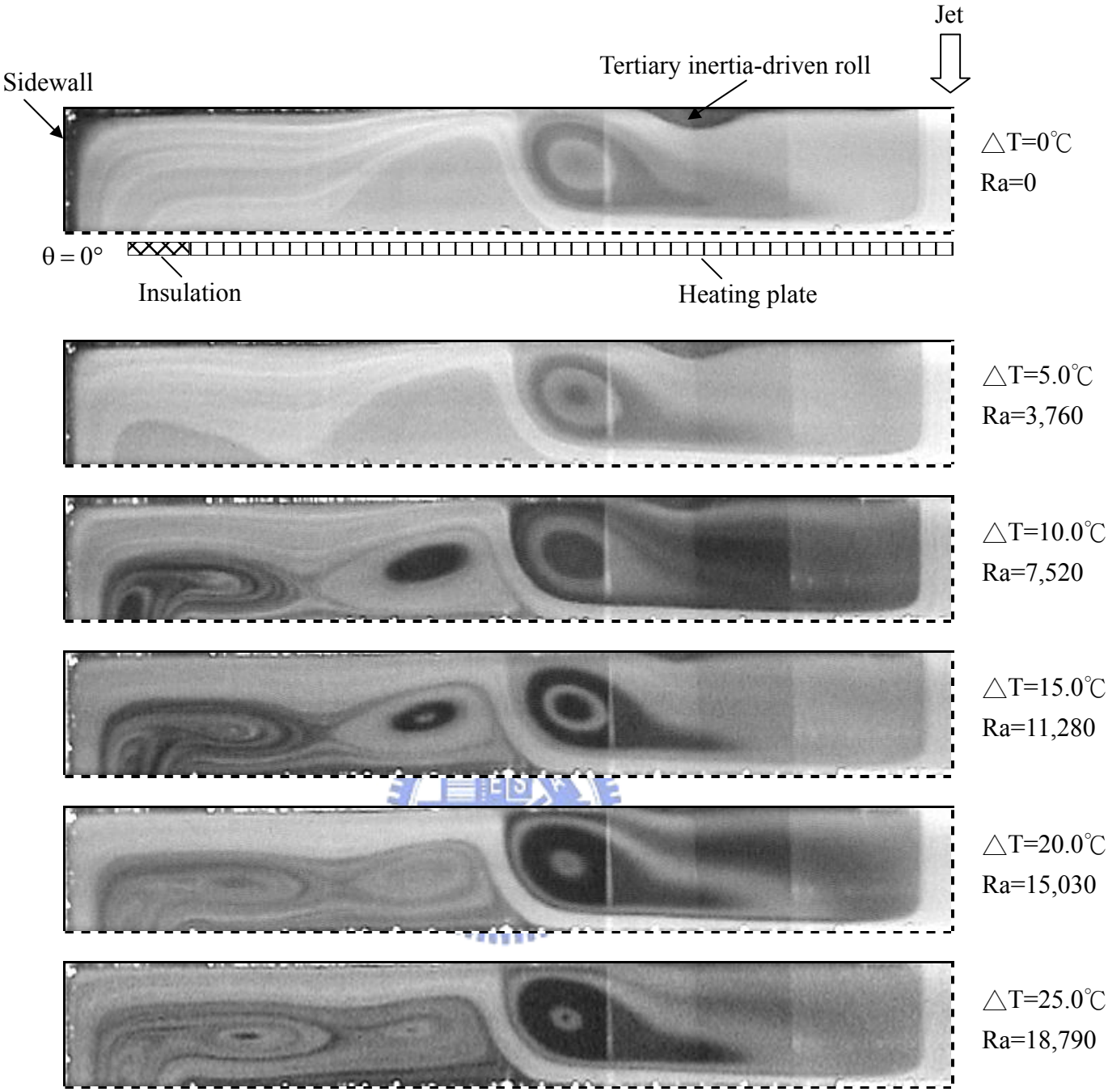

Fig. 4.6 Steady side view flow photos taken at the cross plane θ =0° for various Rayleigh numbers at Re_j=771 (Q_j=5.7 slpm) and H=20.0 mm.

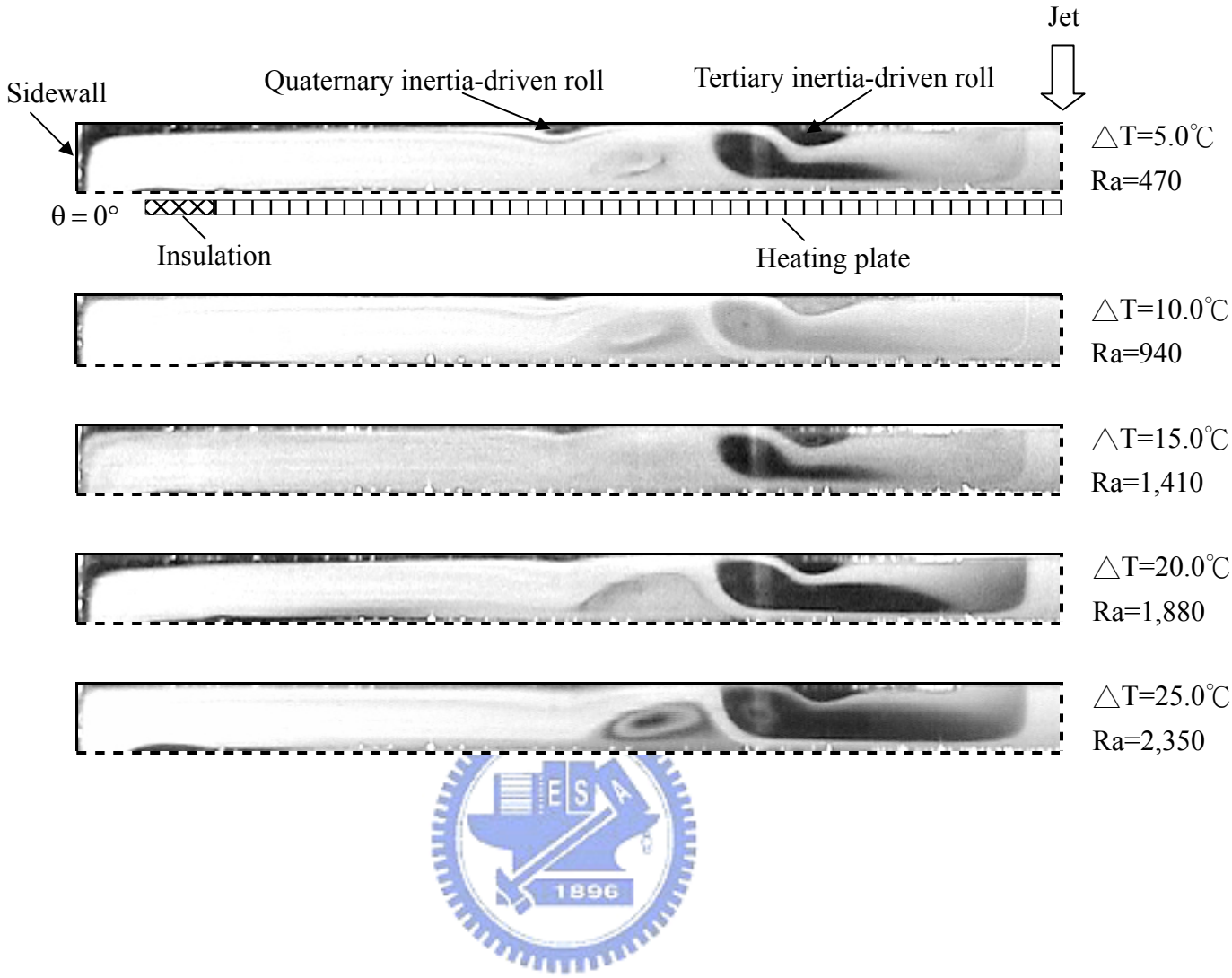

Fig. 4.7 Steady side view flow photos taken at the cross plane θ =0° for various Rayleigh numbers at Re_j=1,150 (Q_j=8.5 slpm) and H=10.0 mm.

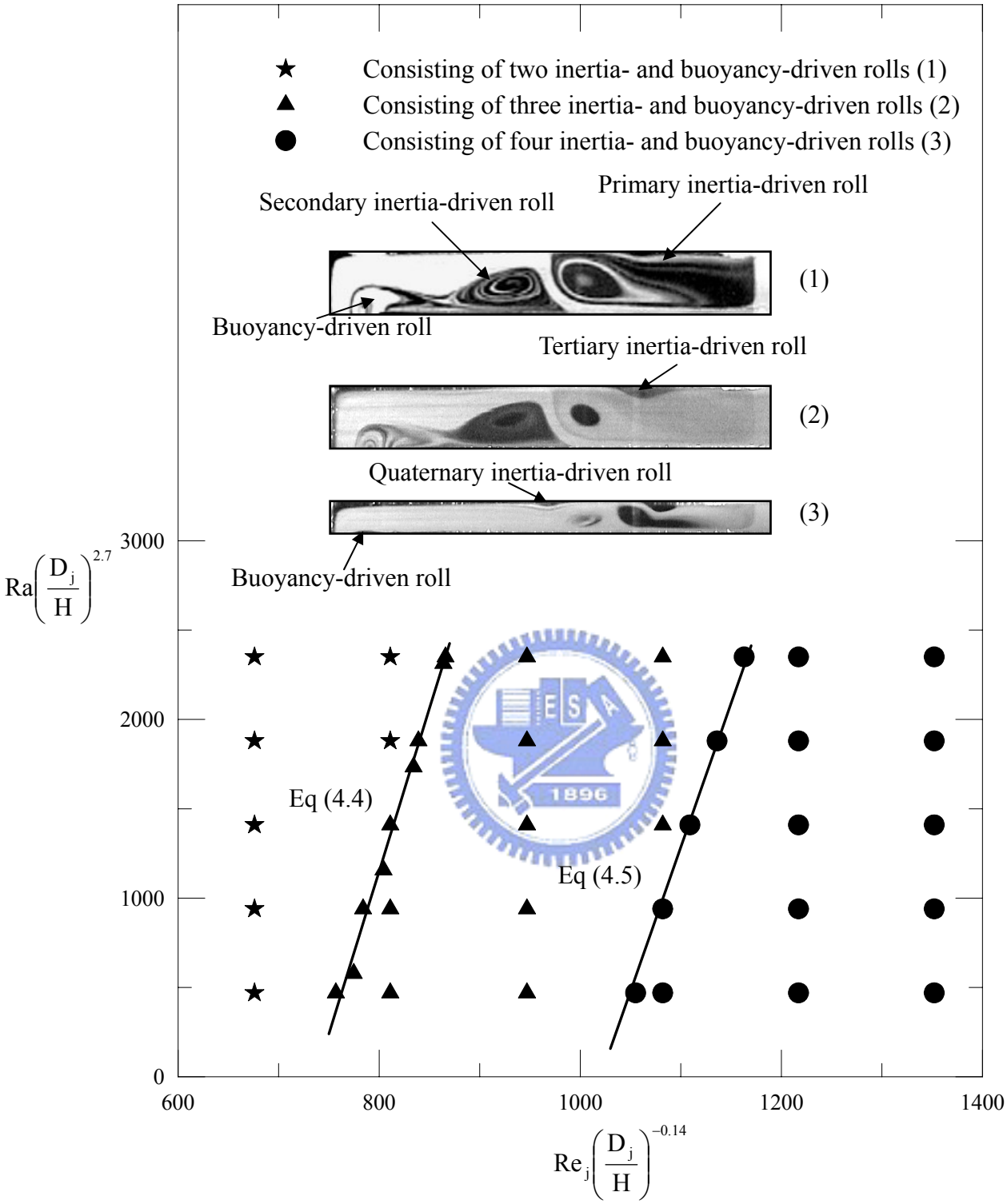

Fig. 4.8 Flow region map delineating the number of rolls.

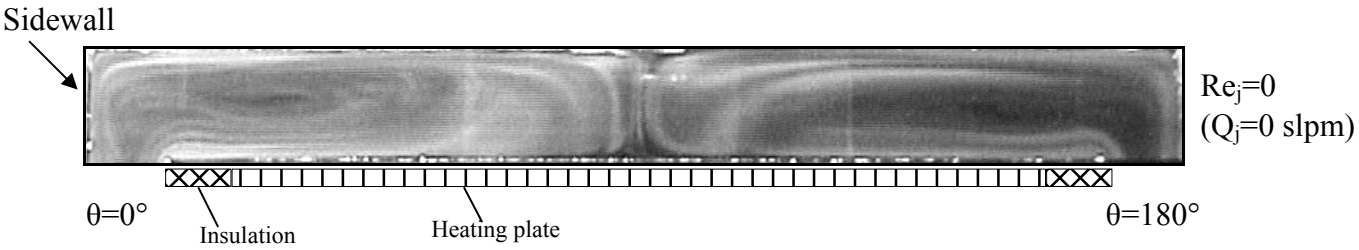

(a) H=30.0 mm & ΔT = 25.0 ℃(Ra=63,420)

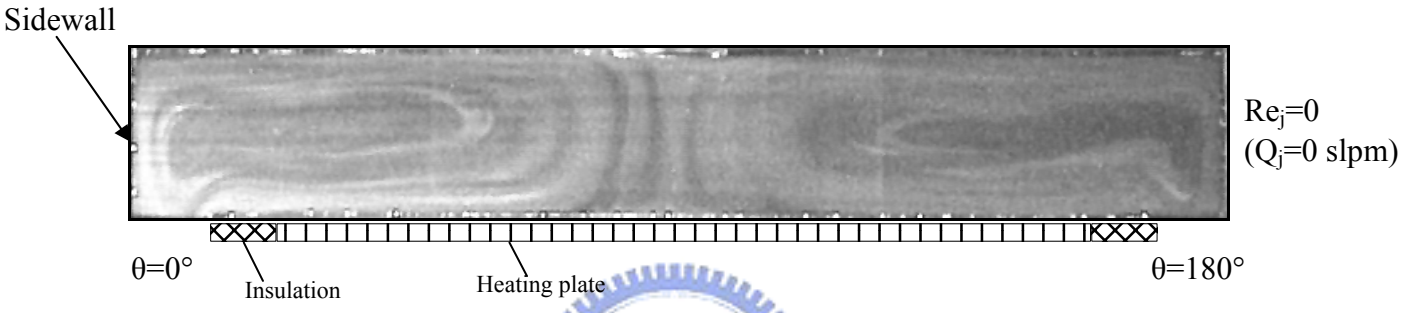

(b) H=45.0 mm & ΔT = 25.0 ℃(Ra=214,040)

Fig. 4.9 Steady vortex flow patterns in the chamber at Re$_j$=0 for (a) H=30.0 mm and Ra=63,420 (ΔT = 25.0 ℃) and (b) H=45.0 mm and Ra=214,040 (ΔT = 25.0 ℃).

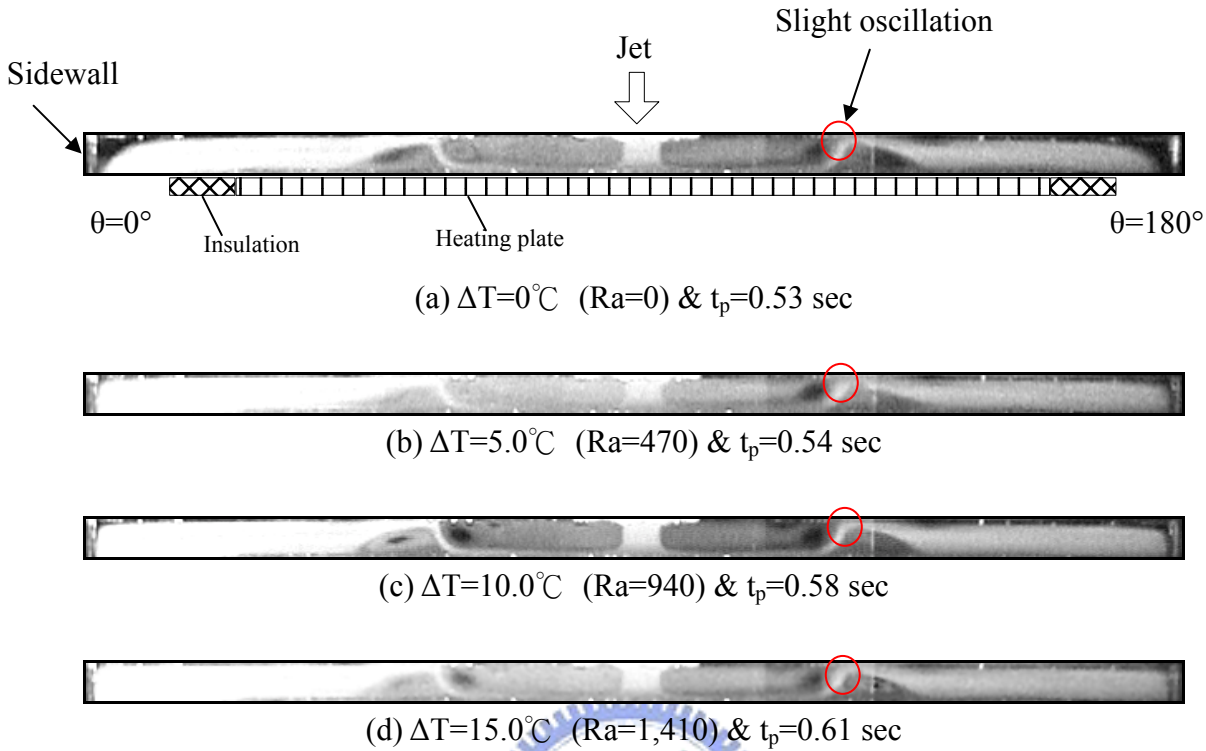

Fig. 4.10 Side view flow photos taken at the cross plane $\theta = 0°$ & 180° at certain instants in a time periodic flow for various Rayleigh numbers at Re_j=1,190 (Q_j=8.8 slpm) and H=10.0 mm.

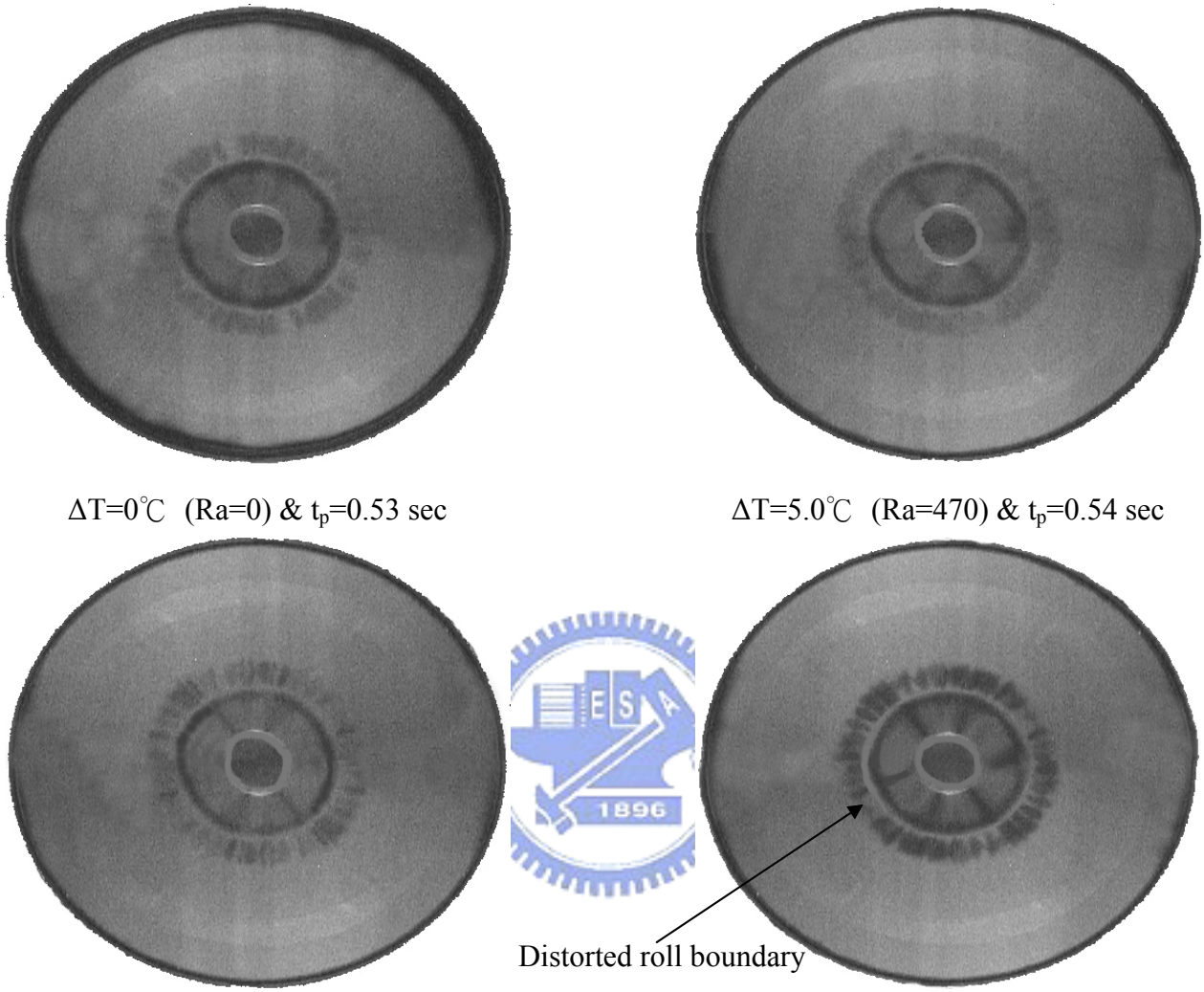

Fig. 4.11 Top view flow photos at certain instants in statistical states taken at middle horizontal plane halfway between the pipe exit and heated disk for various Rayleigh numbers at Re_j=1,190 (Q_j=8.8 slpm) and H=10.0 mm.

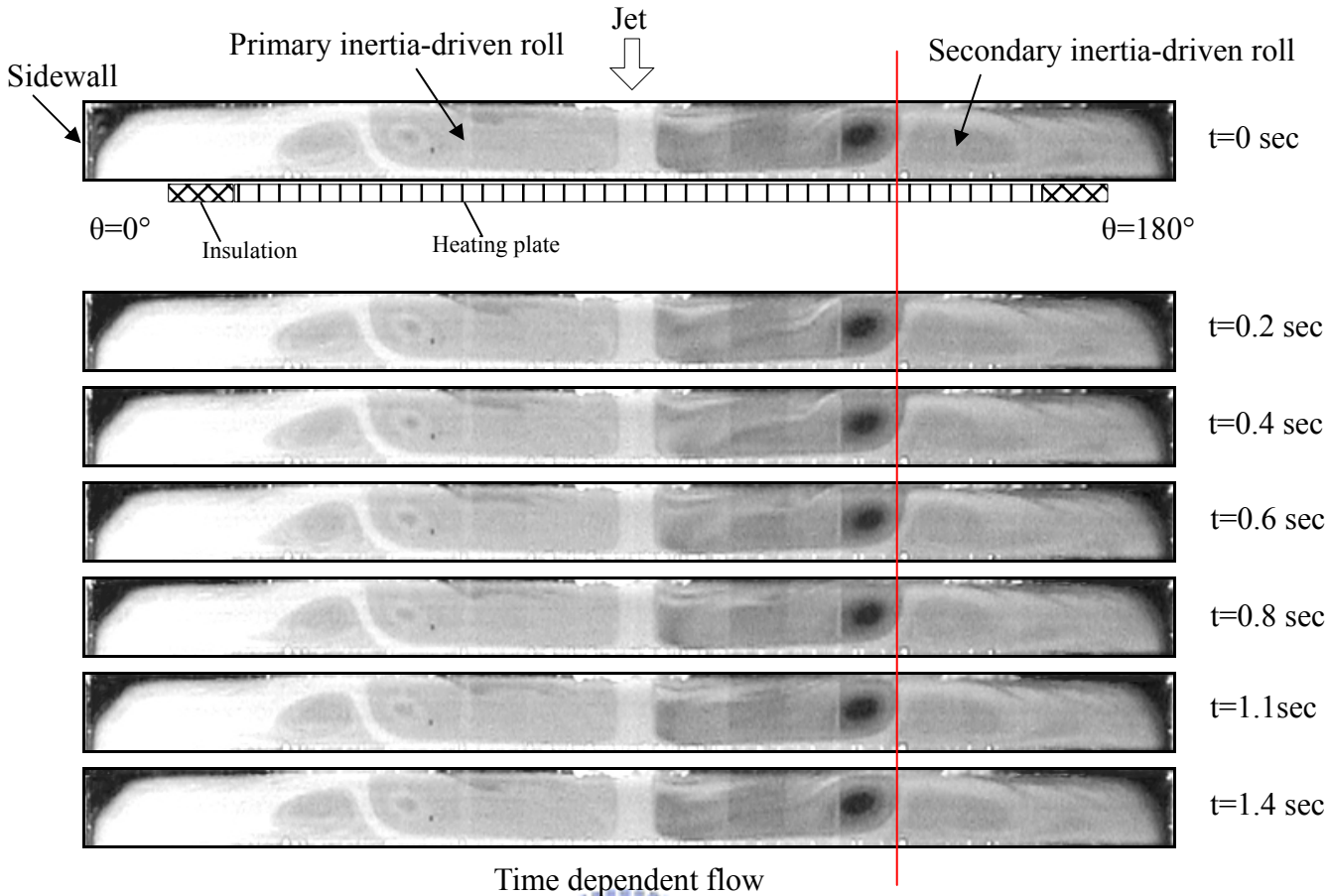

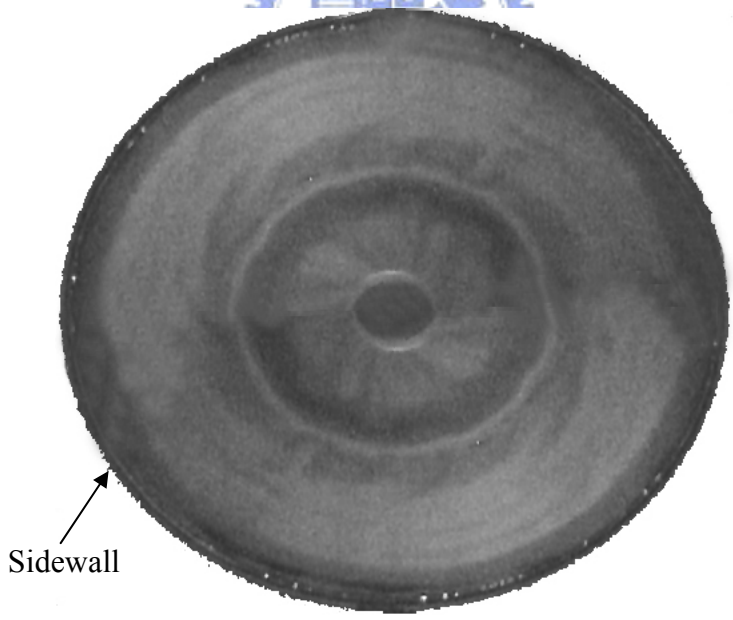

Fig. 4.12 Time-periodic vortex flow for H=20.0 mm and Ra=0 ($\Delta T = 0$℃) at Re_j=839 (Q_j=6.2 slpm) illustrated by (a) side view flow photos taken at the vertical plane $\theta = 0°$ & $\theta = 180°$ at selected time instants in a typical periodic cycle and (b) top view flow photo taken at middle horizontal plane halfway between the pipe exit and heated disk at certain time instant in the cycle (t_p=1.45 sec).

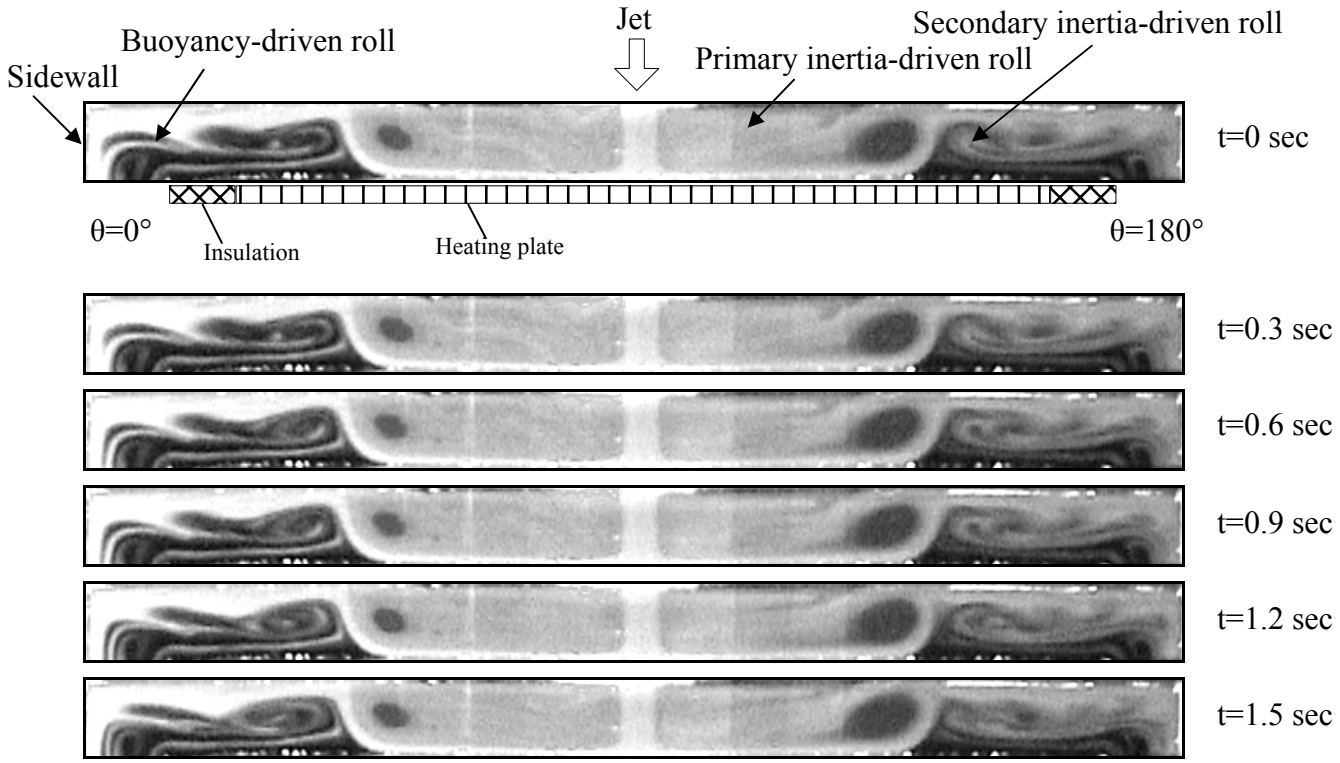

Time dependent flow

(a)

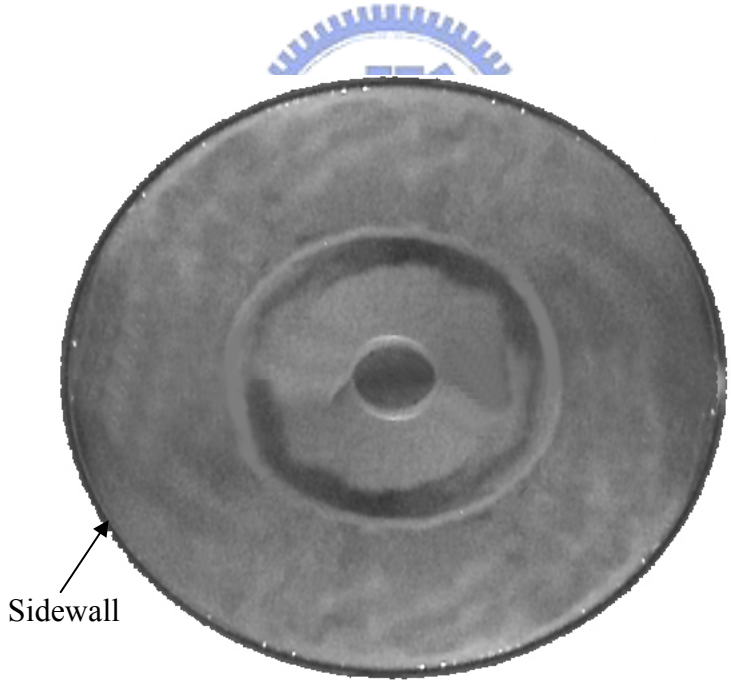

(b)

Fig. 4.13 Time-periodic vortex flow for H=20.0 mm and Ra=18,790 ($\Delta T = 25.0℃$) at Re_j=1,028 (Q_j=7.6 slpm) illustrated by (a) side view flow photos taken at the vertical plane $\theta = 0°$ & $\theta = 180°$ at selected time instants in a typical periodic cycle and (b) top view flow photo taken at middle horizontal plane halfway between the pipe exit and heated disk at certain time instant in the cycle (t_p=1.58 sec).

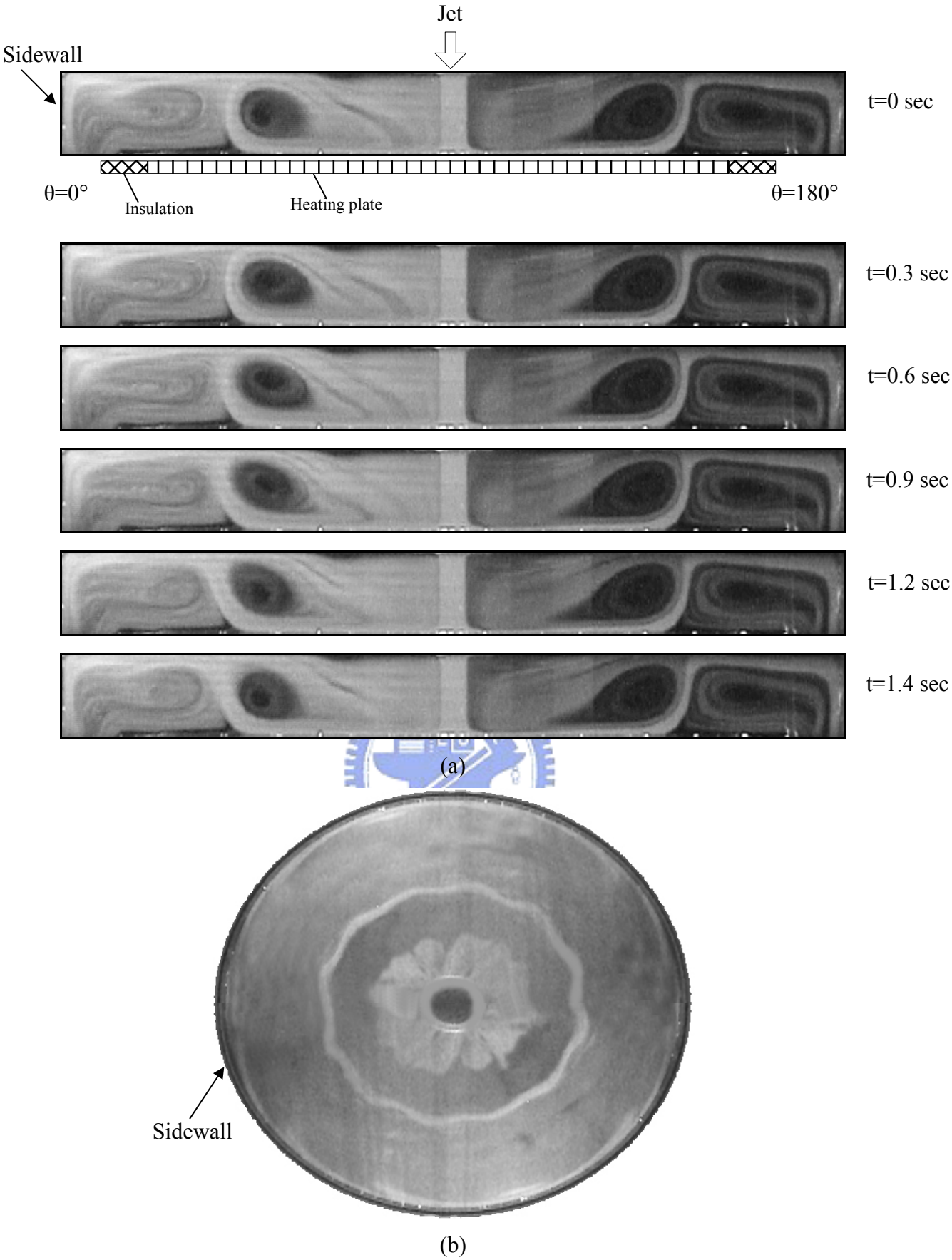

Fig. 4.14 Time-periodic vortex flow for H=30.0 mm and Ra=38,050 ($\Delta T = 15.0$℃) at Re_j=676 (Q_j=5.0 slpm) illustrated by (a) side view flow photos taken at the vertical plane $\theta = 0°$ & $\theta = 180°$ at selected time instants in a typical periodic cycle and (b) top view flow photo taken at middle horizontal plane halfway between the pipe exit and heated disk at certain time instant in the cycle (t_p=1.43 sec).

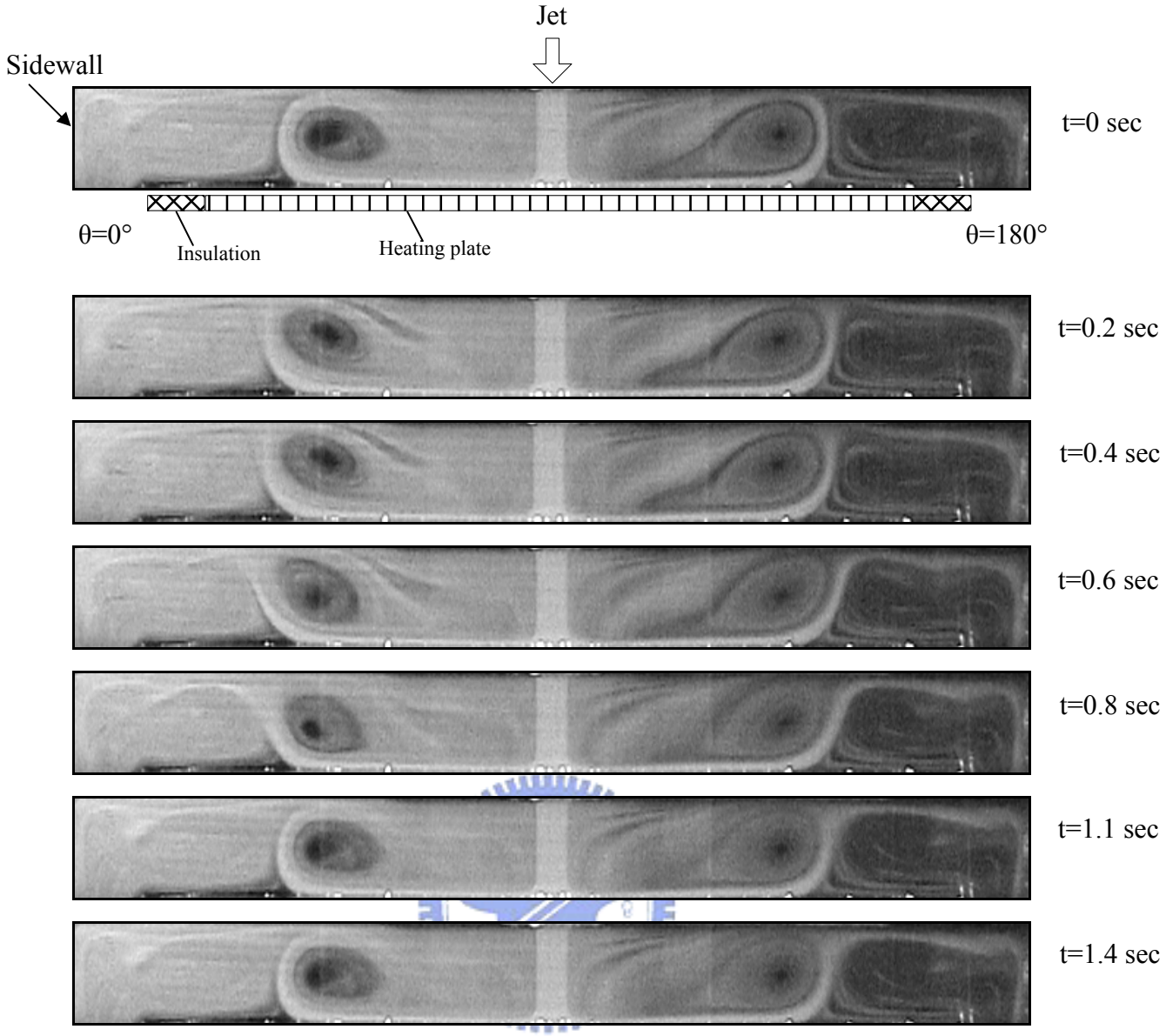

Fig. 4.15 Time-periodic vortex flow for H=30.0 mm and Ra=50,730 ($\Delta T = 20.0$℃) at Re_j=676 (Q_j=5.0 slpm) illustrated by side view flow photos taken at the vertical plane $\theta = 0°$ & $\theta = 180°$ at selected time instants in a typical periodic cycle (t_p=1.43 sec).

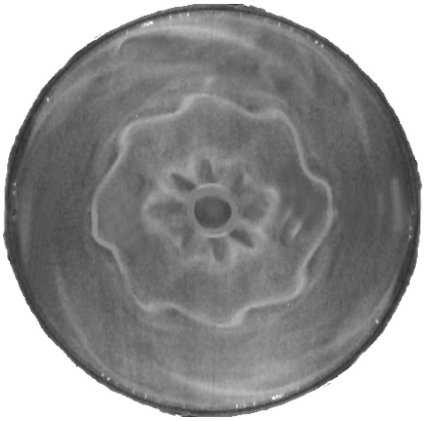

(a)t=0 sec

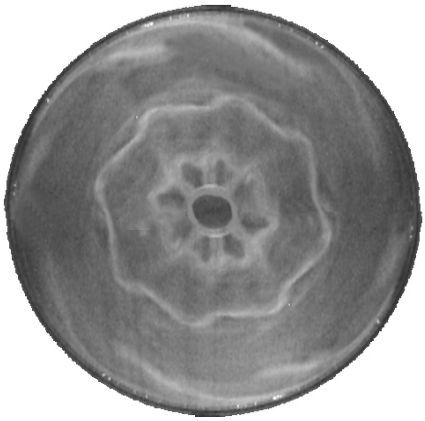

(b)t=0.2 sec

(c)t=0.4 sec

(d)t=0.6 sec

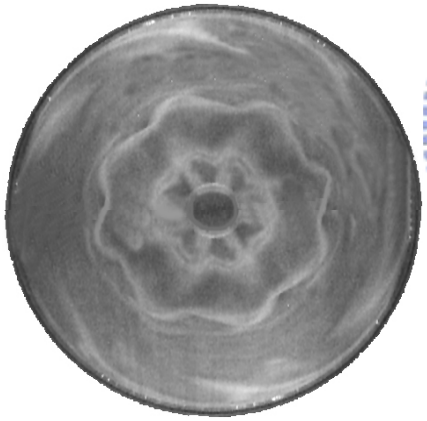

(e)t=0.8 sec

(f)t=1.1 sec

(g)t=1.4 sec

Fig. 4.16 Top view flow photos taken at selected time instants in a typical periodic cycle with Ra=50,730 (ΔT=20.0℃), Q=5.0 slpm (Re_j=676) and H=30.0 mm (t_p=1.43 sec).

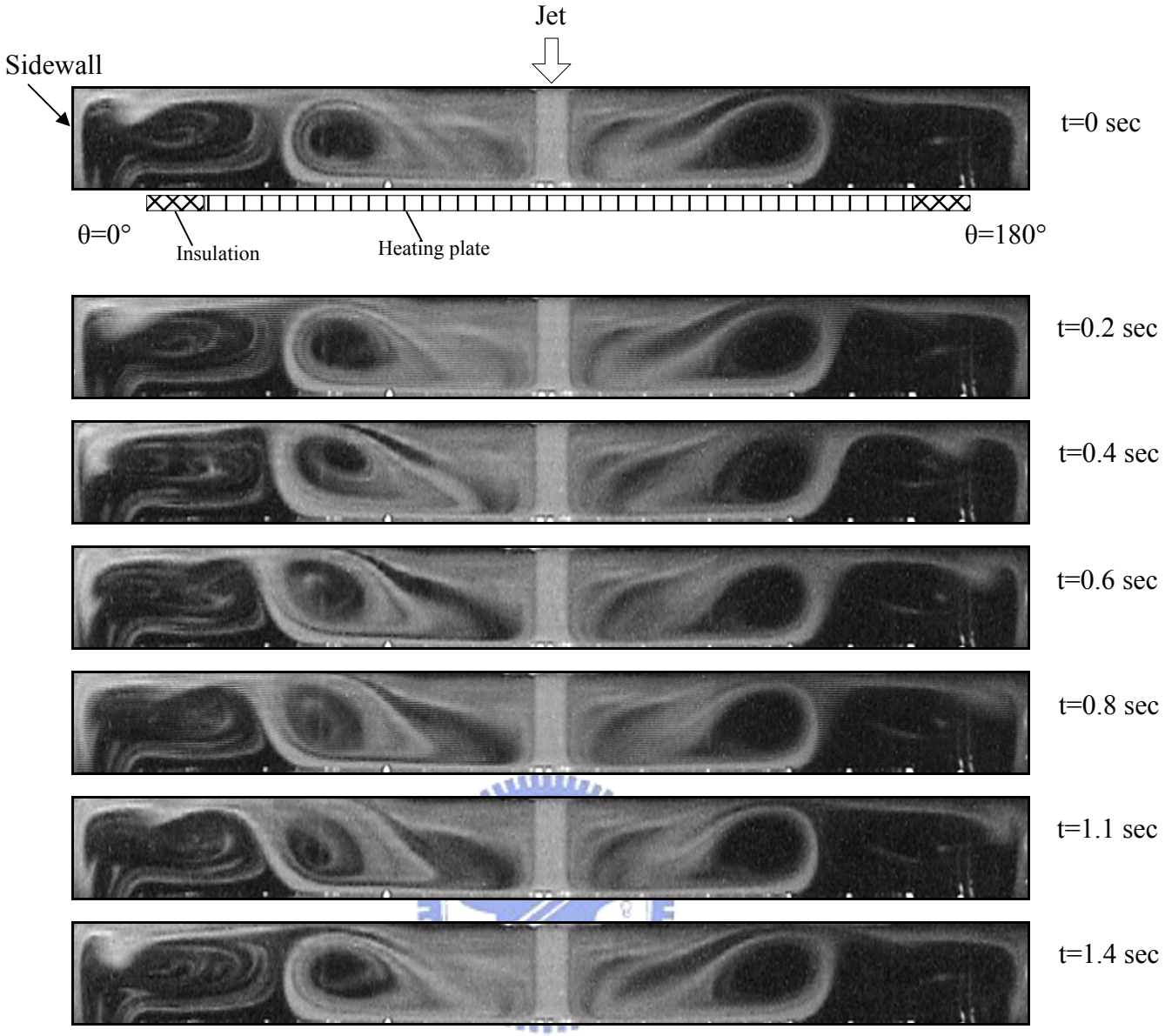

Time dependent flow

Fig. 4.17 Time-periodic vortex flow for H=30.0 mm and Ra=63,420 ($\Delta T = 25.0$℃) at Re_j=676 (Q_j=5.0 slpm) illustrated by side view flow photos taken at the vertical plane $\theta = 0°$ & $\theta = 180°$ at selected time instants in a typical periodic cycle (t_p=1.43 sec).

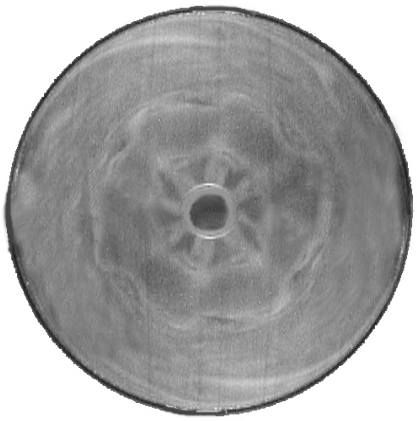

(a) t=0 sec

(b) t=0.2 sec

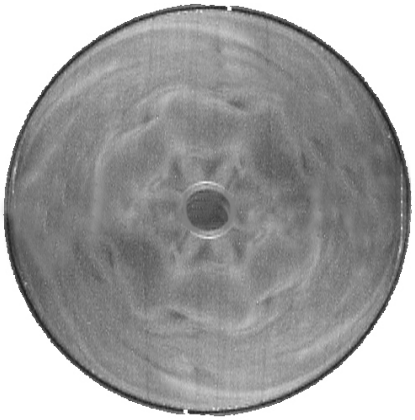

(c) t=0.4 sec

(d) t=0.6 sec

(e) t=0.8 sec

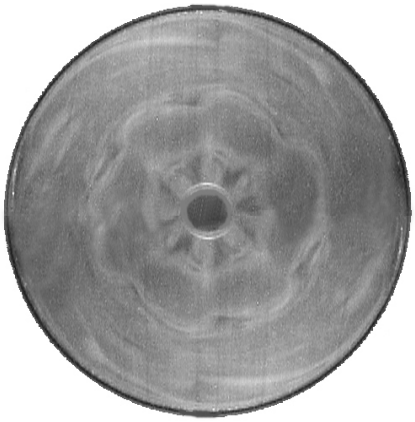

(f) t=1.1 sec

(g) t=1.4 sec

Fig. 4.18 Top view flow photos taken at selected time instants in a typical periodic cycle with Ra=63,420 (ΔT=25.0℃), Q=5.0 slpm(Re_j=676) and H=30.0 mm (t_p=1.43 sec).

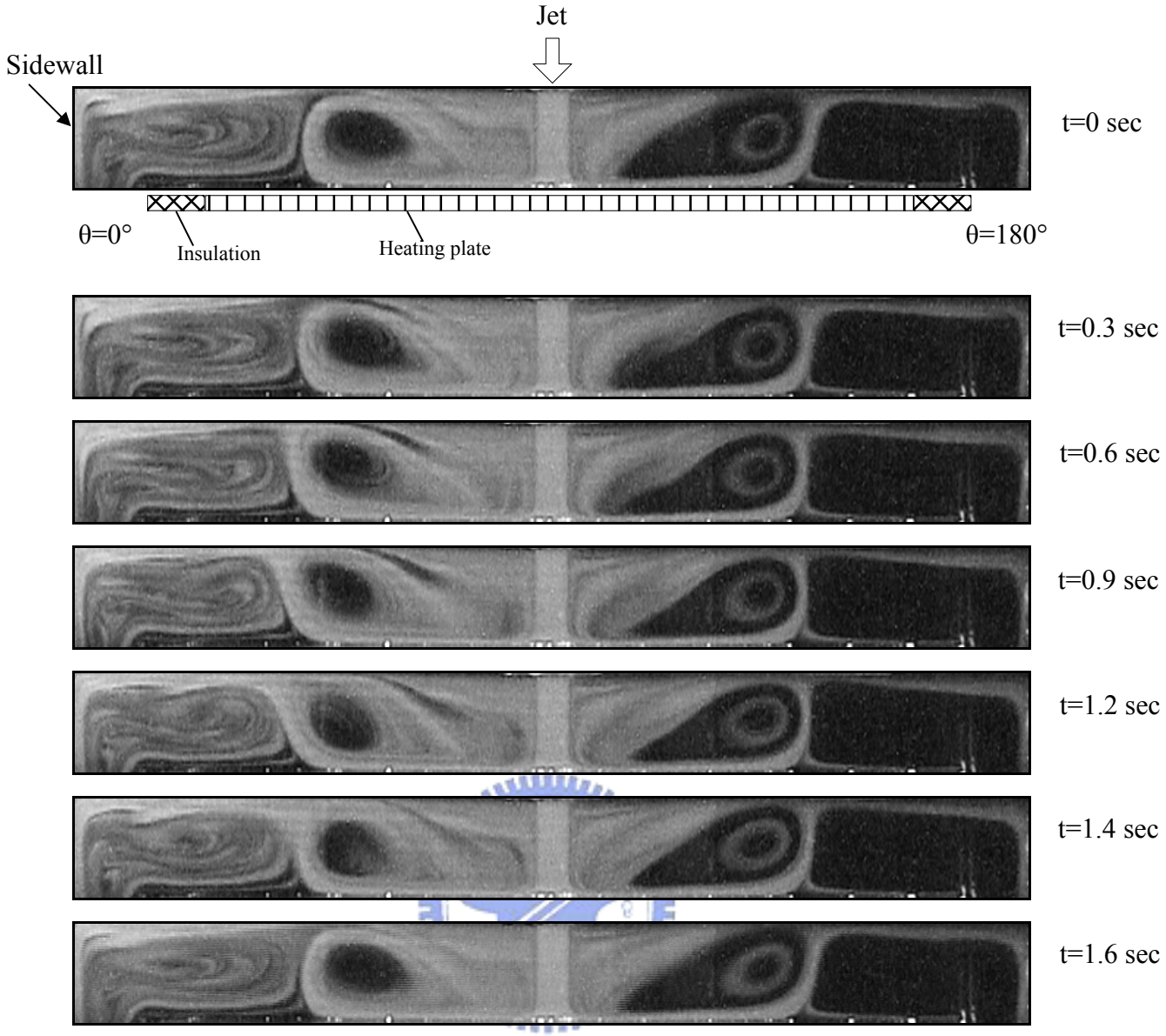

Time dependent flow

Fig. 4.19 Time-periodic vortex flow for H=30.0 mm and Ra=63,420 ($\Delta T = 25.0℃$) at Re_j=541 (Q_j=4.0 slpm) illustrated by side view flow photos taken at the vertical plane $\theta = 0°$ & $\theta = 180°$ at selected time instants in a typical periodic cycle (t_p=1.67 sec).

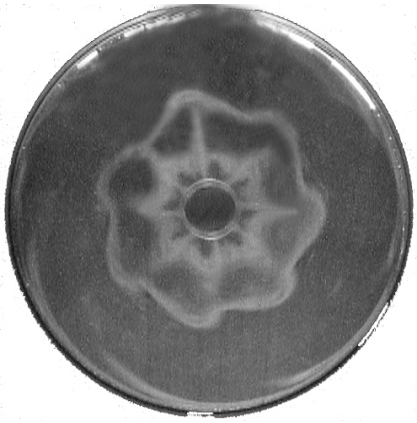

(a) t=0 sec

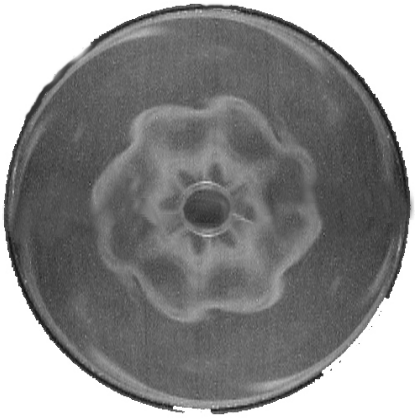

(b) t=0.3 sec

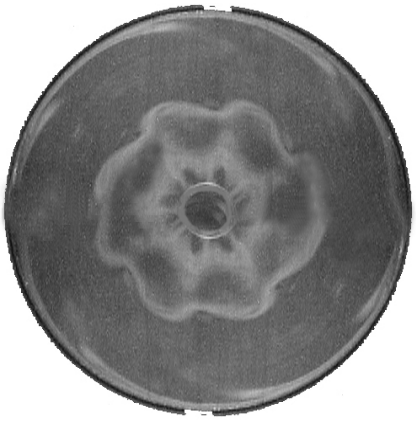

(c) t=0.6 sec

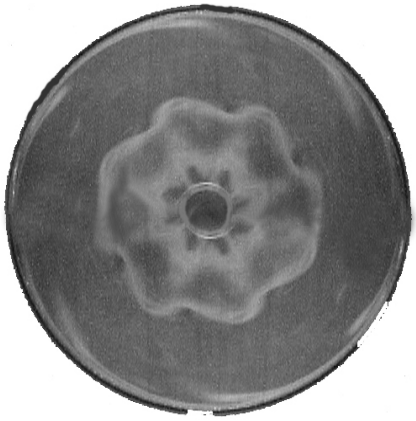

(d) t=0.9 sec

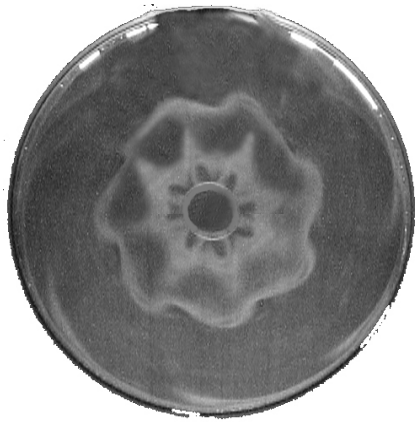

(e) t=1.2sec

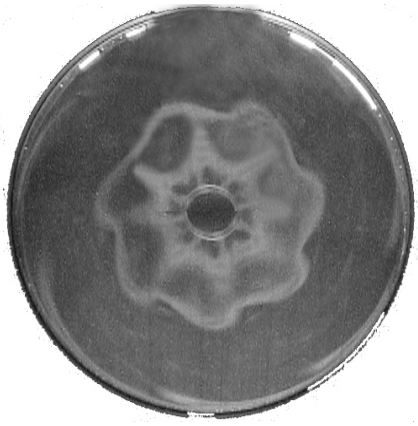

(f) t=1.4 sec

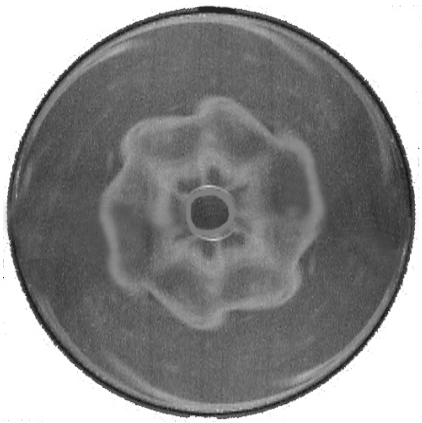

(g) t=1.6 sec

Fig. 4.20 Top view flow photos taken at selected time instants in a typical periodic cycle with Ra=63,420 (ΔT=25.0℃), Q=4.0 slpm(Re_j=541) and H=30.0 mm (t_p=1.67 sec).

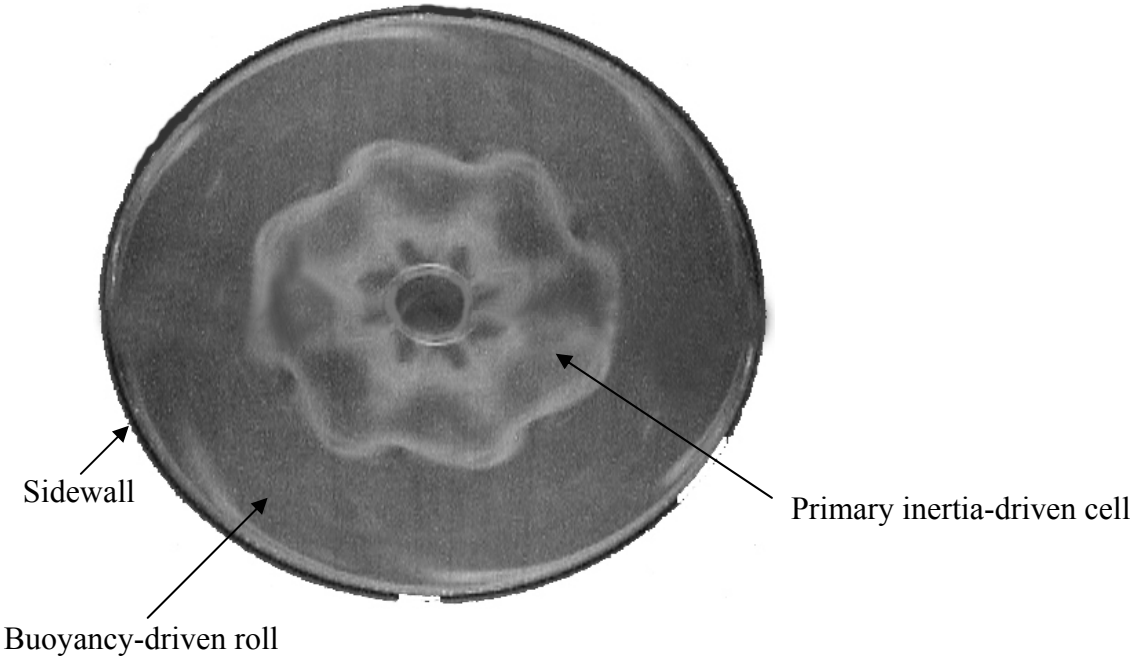

(a)

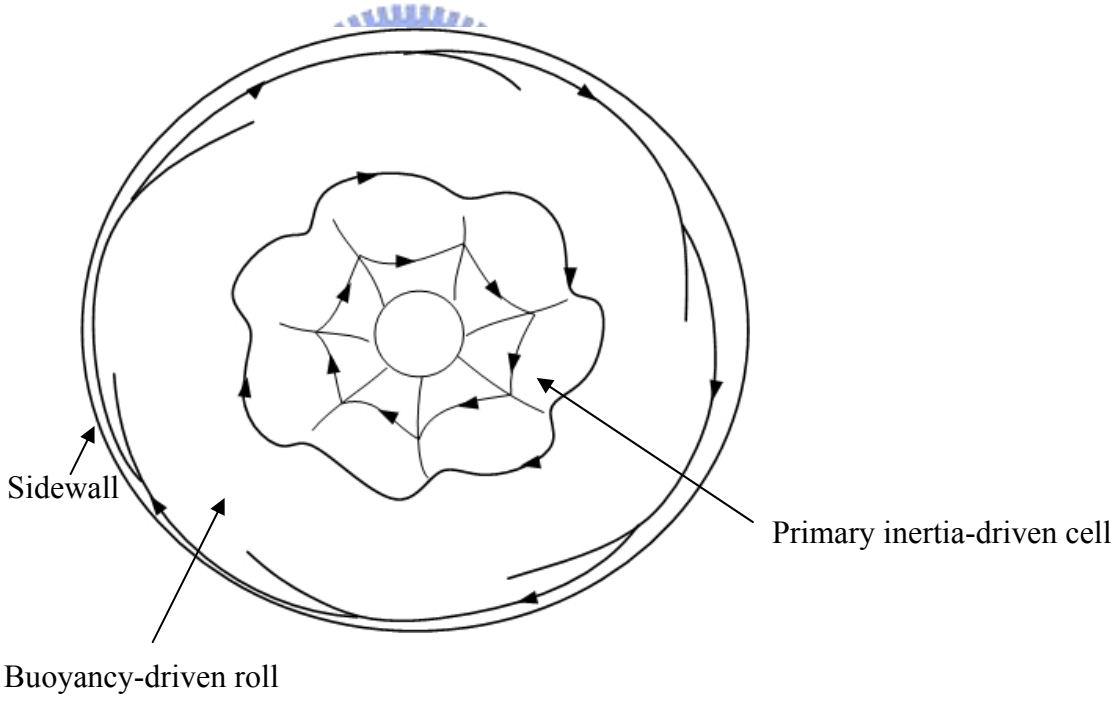

(b)

Fig. 4.21 Top view flow photo taken at the middle horizontal plane for Q_j=4.0 slpm (Re_j=541) and ΔT=25.0℃ (Ra=63,420) with H=30.0 mm at certain time instant (a) and the corresponding schematically sketched cross plane flow (b) in a typical periodic cycle.

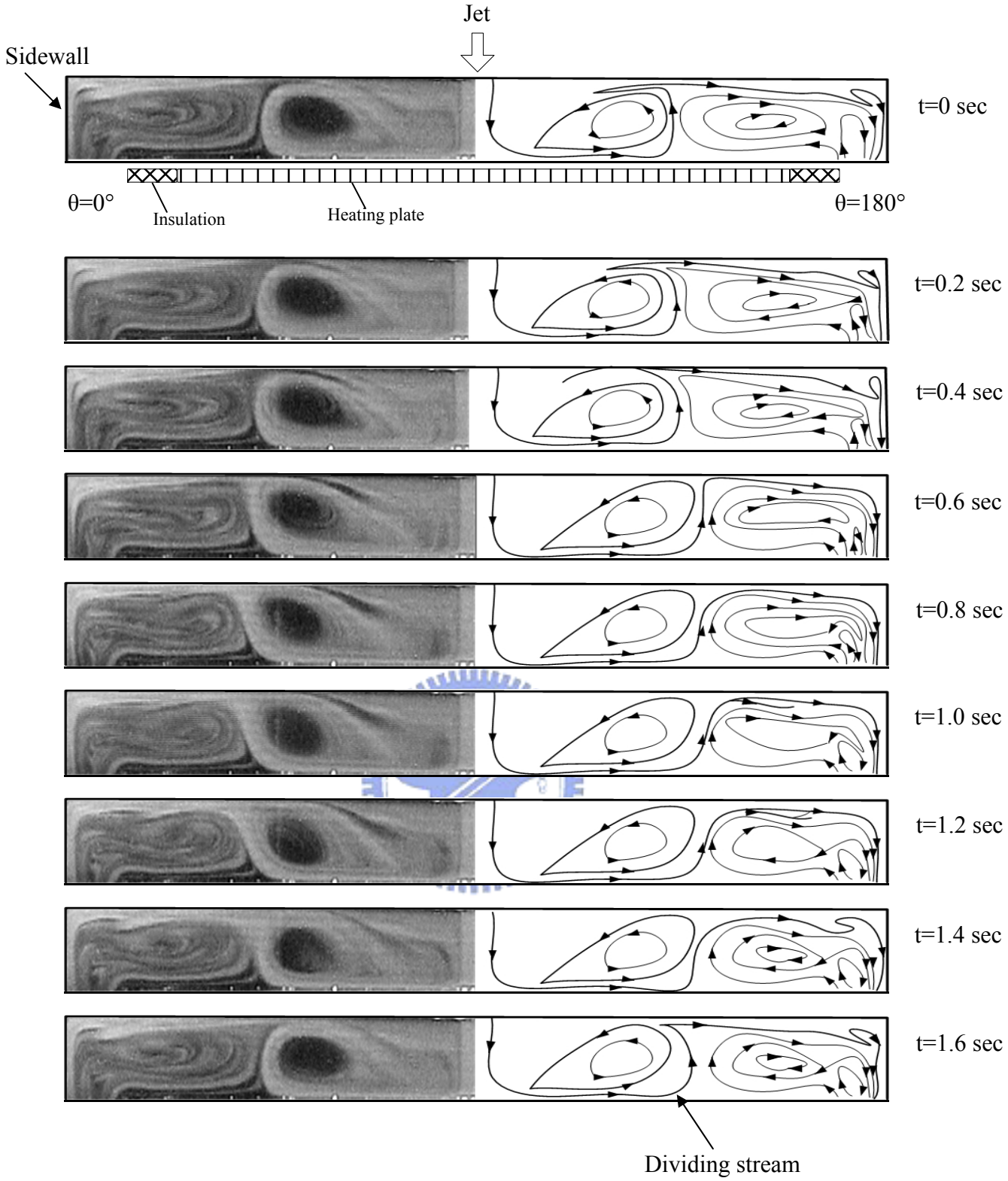

Fig. 4.22 Side view flow photos taken at the cross plane θ =0° for Q_j=4.0 slpm (Re_j=541) and ΔT=25.0℃ (Ra=63,420) with H=30.0 mm at selected time instants (left) and the corresponding schematically sketched cross plane flow (right) in a typical periodic cycle (t_p=1.67 sec).

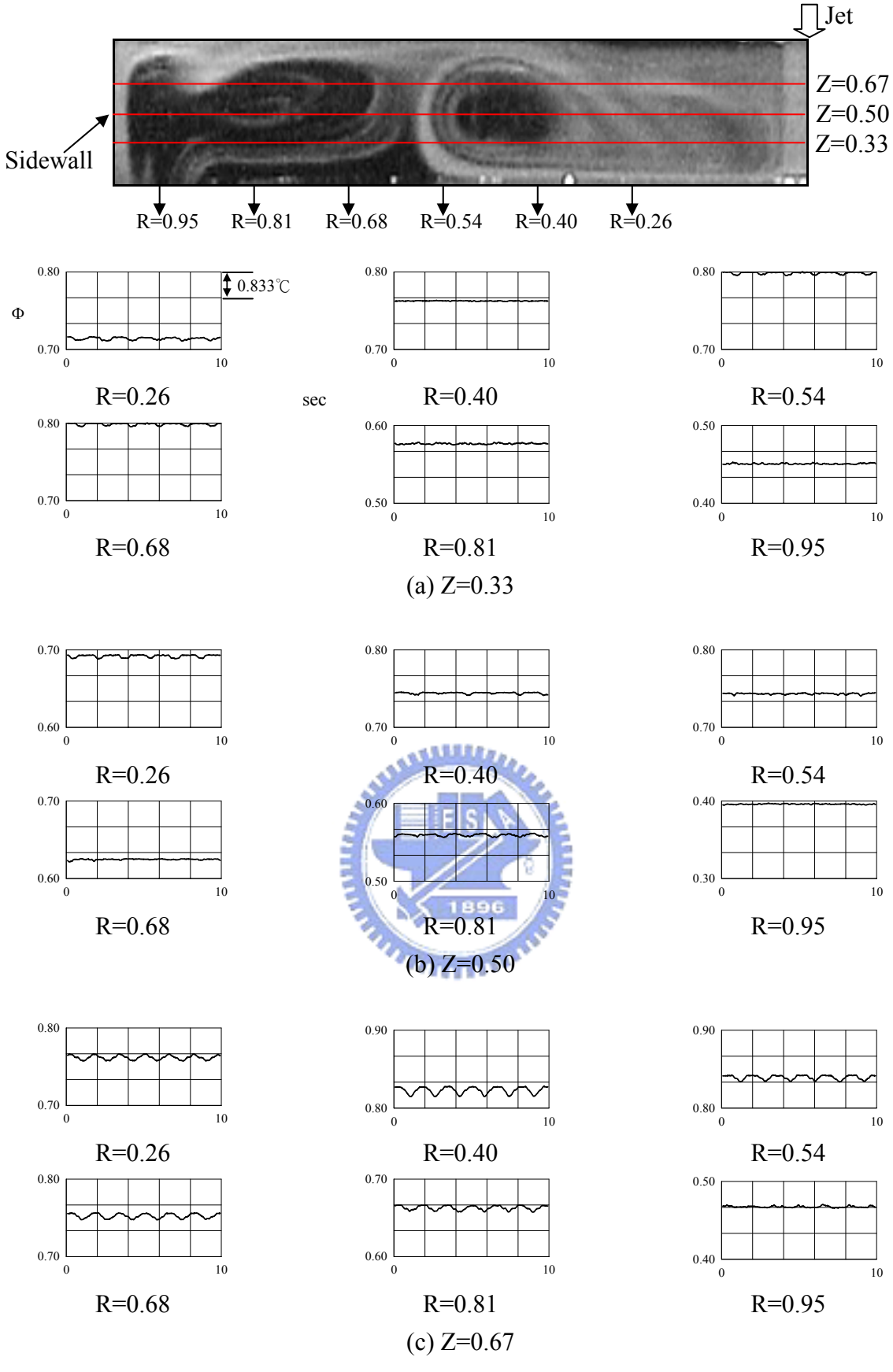

Fig. 4.23 The time records of non-dimensional air temperature for Ra=63,420 ($\Delta T = 25.0℃$) and Re_j=676 (Q_j=5.0 slpm) with H=30.0 mm at selected locations for (a) Z=0.33, (b) Z=0.50 and (c) Z=0.67 on the cross plane $\theta = 0°$ (t_p=1.43 sec).

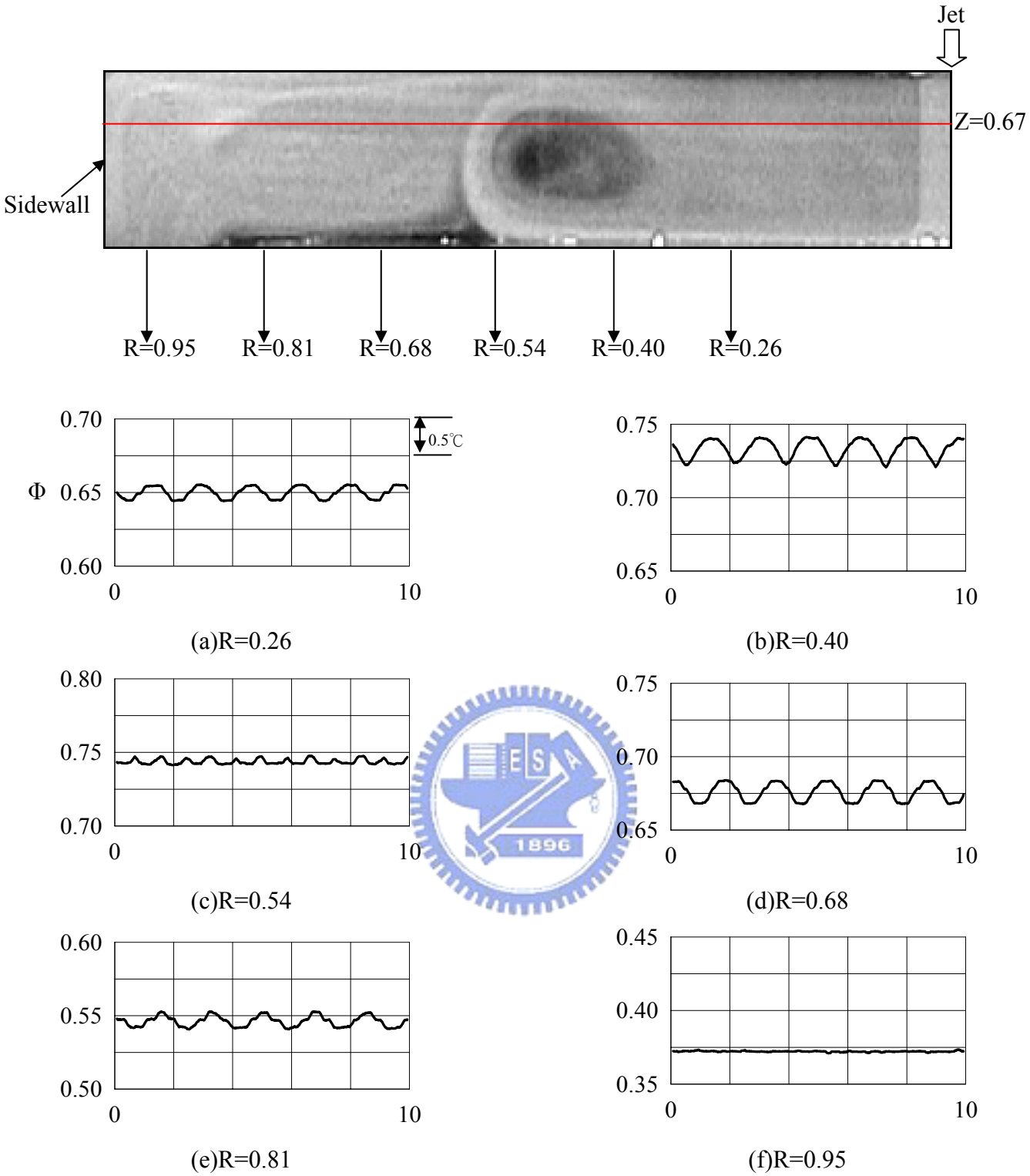

Fig. 4.24 The time records of non-dimensional air temperature for Ra=50,730 ($\Delta T = 20.0℃$) and Re_j=676 (Q_j=5.0 slpm) with H=30.0 mm measured at selected locations on the vertical plane $\theta = 0°$ at Z=0.67 (t_p=1.43 sec).

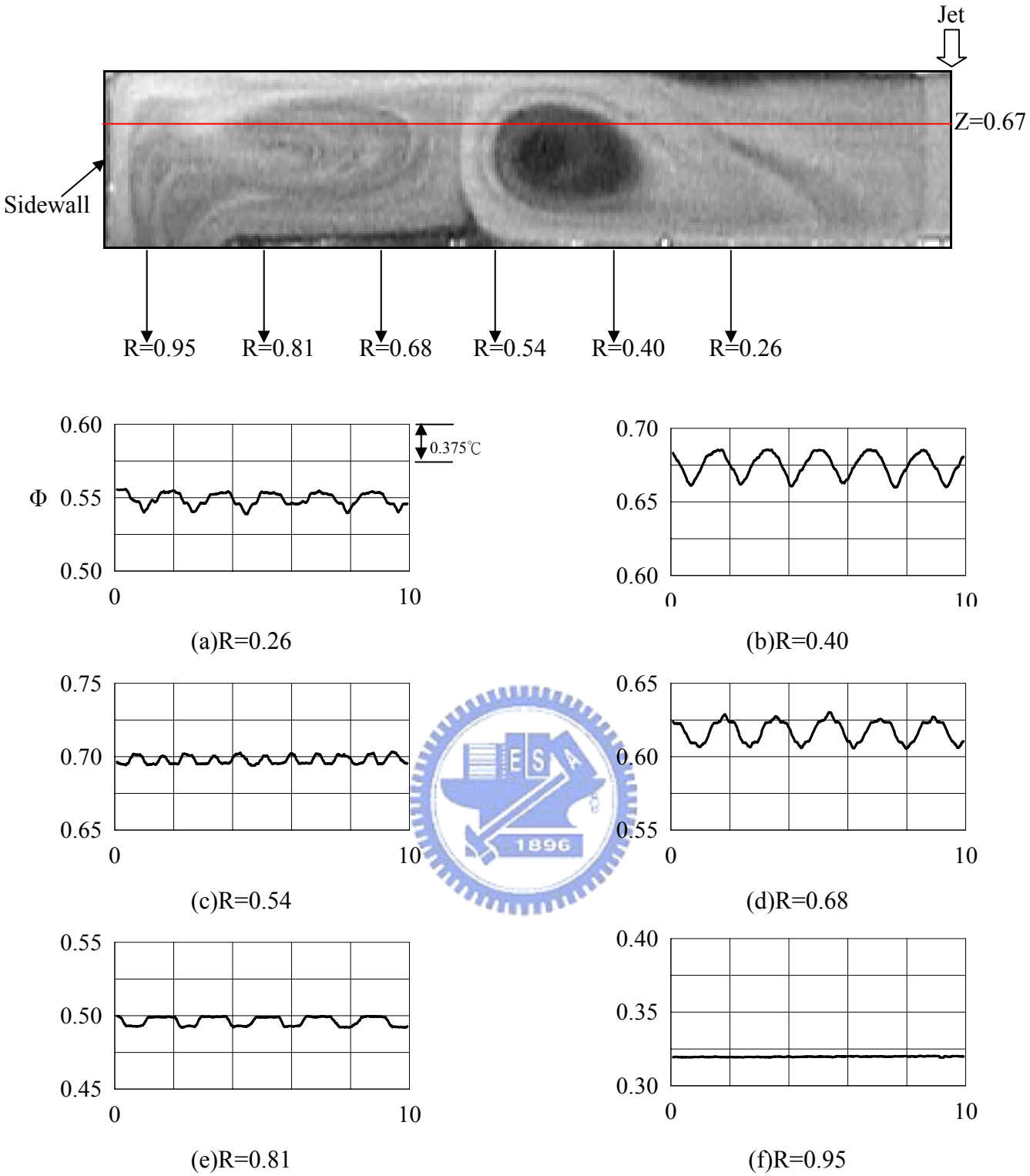

Fig. 4.25 The time records of non-dimensional air temperature for Ra=38,050 ($\Delta T = 15.0$℃) and Re_j=676 (Q_j=5.0 slpm) with H=30.0 mm measured at selected locations on the vertical plane $\theta = 0°$ at Z=0.67 (t_p=1.43 sec).

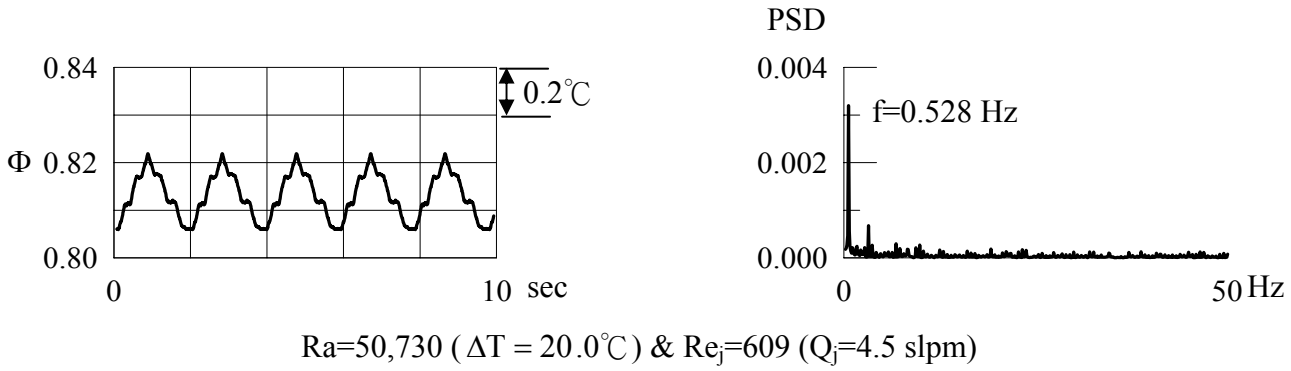

Ra=50,730 ($\Delta T = 20.0℃$) & Re_j=609 (Q_j=4.5 slpm)

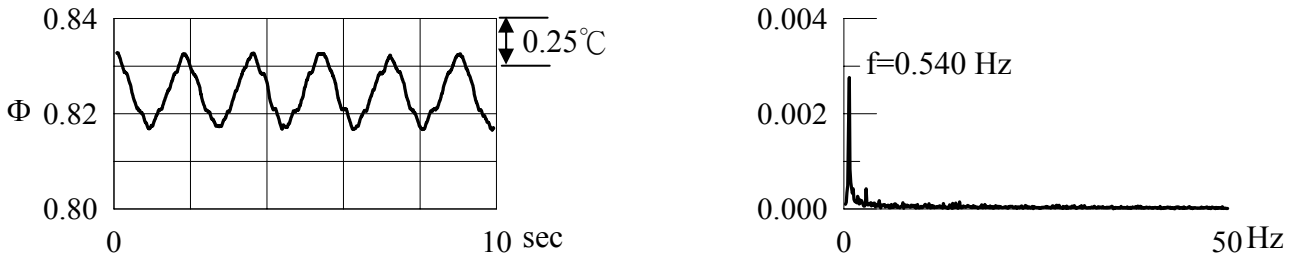

Ra=63,420 ($\Delta T = 25.0℃$) & Re_j=609 (Q_j=4.5 slpm)

(a)

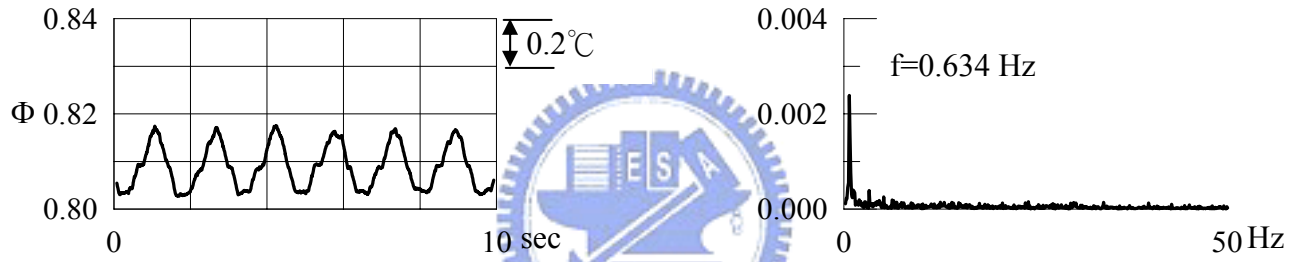

Ra=50,730 ($\Delta T = 20.0℃$) & Re_j=744 (Q_j=5.5 slpm)

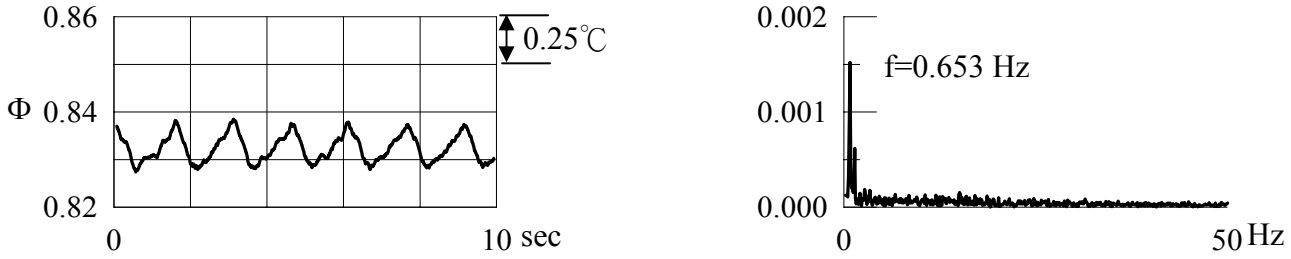

Ra=63,420 ($\Delta T = 25.0℃$) & Re_j=744 (Q_j=5.5 slpm)

(b)

Fig. 4.26 The time records of non-dimensional air temperature and the corresponding power spectrum densities for fixed Re_j for various Rayleigh numbers with H=30.0 mm at location (R, Z) = (0.58, 0.67) on the vertical plane $\theta = 0°$.

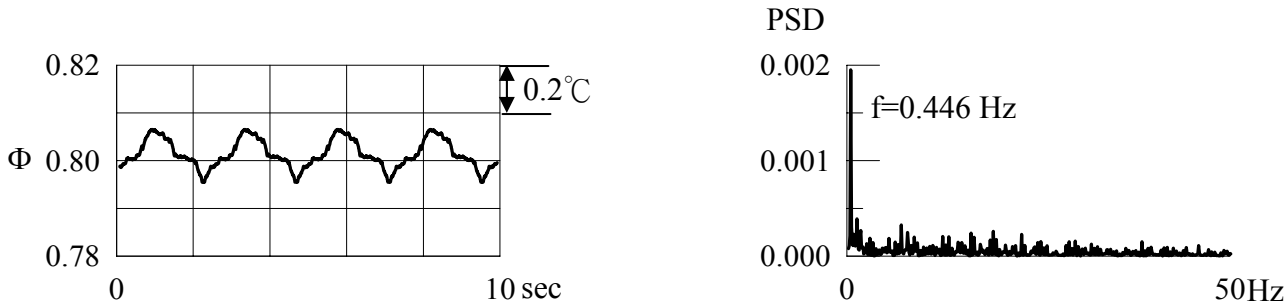

(a) Q_j=4.0 slpm

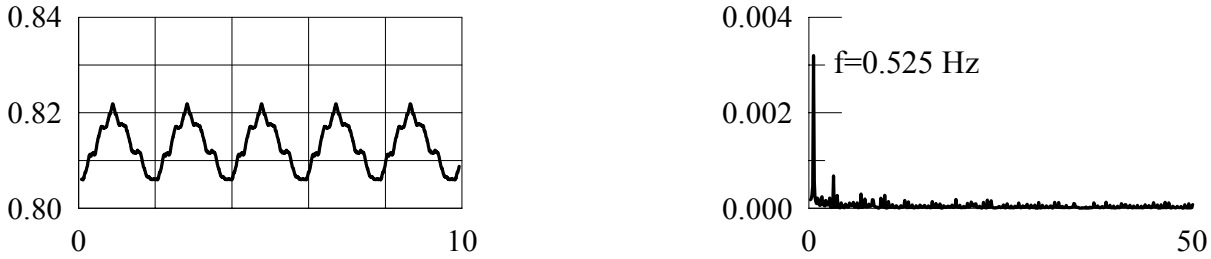

(b) Q_j=4.5 slpm

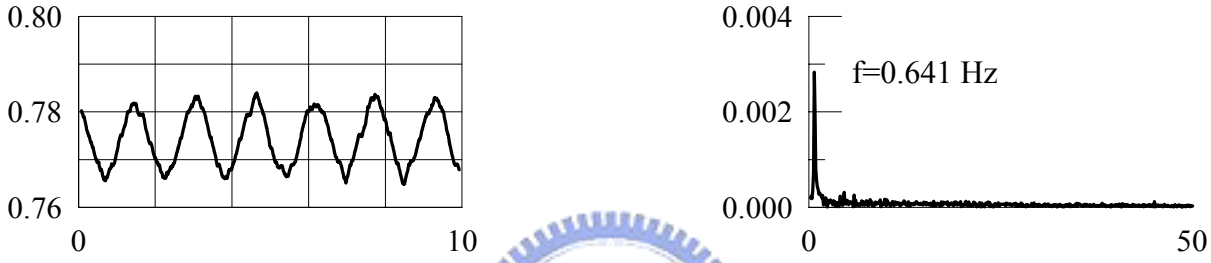

(c) Q_j=5.0 slpm

(d) Q_j=5.5 slpm

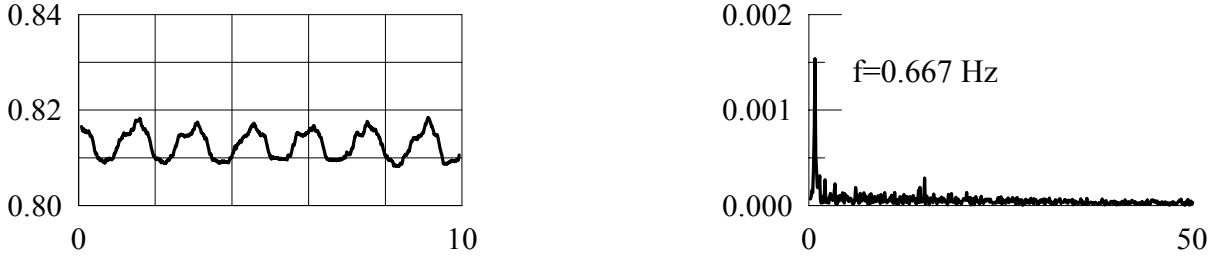

(e) Q_j=6.0 slpm

Fig. 4.27 The time records of non-dimensional air temperature and the corresponding power spectrum densities for Ra=50,730 and H=30.0 mm at location (R, Z)=(0.58, 0.67) on the vertical plane $\theta = 0°$ for various jet Reynolds numbers Re_j= (a)541, (b)609, (c)676, (d)744 and (e)811.

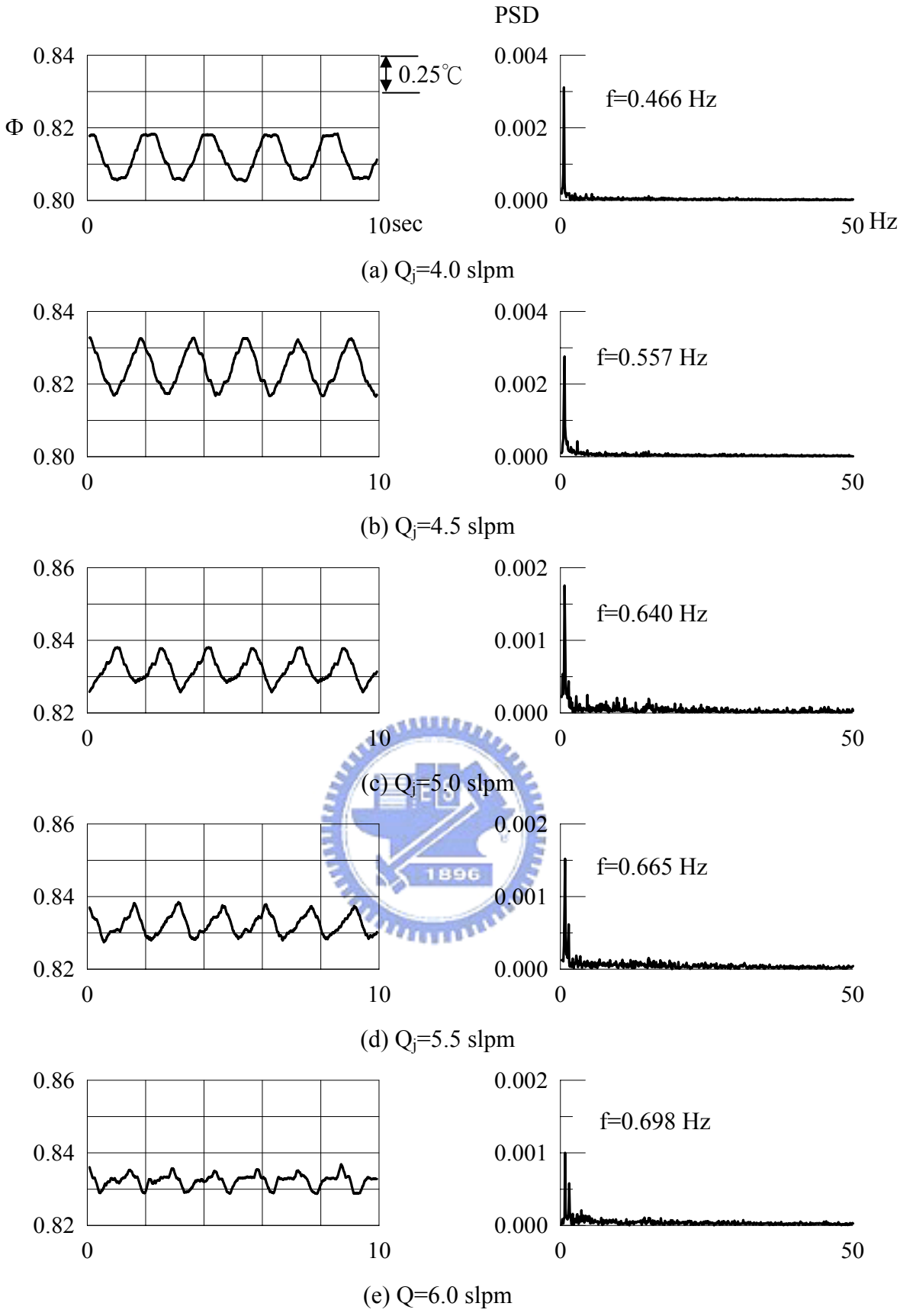

Fig. 4.28 The time records of non-dimensional air temperature and the corresponding power spectrum densities for Ra=63,420 and H=30.0 mm at location (R, Z)=(0.58, 0.67) on the vertical plane $\theta = 0°$ for various jet Reynolds numbers Re_j= (a)541, (b)609, (c)676, (d)744 and (e)811.

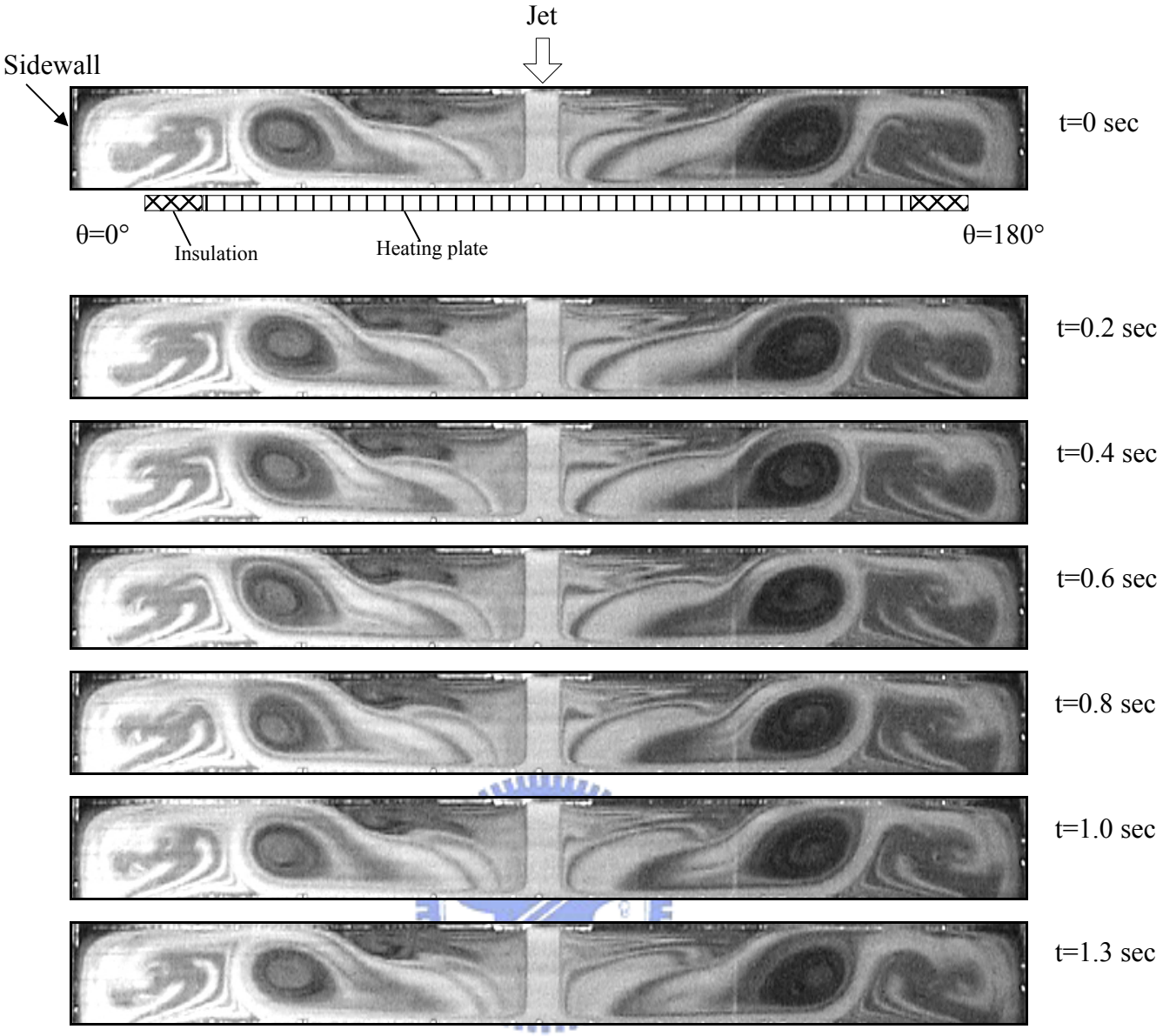

Time dependent flow

Fig. 4.29 Time-periodic vortex flow for H=30.0 mm and Ra=0 ($\Delta T = 0$℃) at Re_j=879 (Q_j=6.5 slpm) illustrated by side view flow photos taken at the vertical plane $\theta = 0°$ & $\theta = 180°$ at selected time instants in a typical periodic cycle (t_p=1.33 sec).

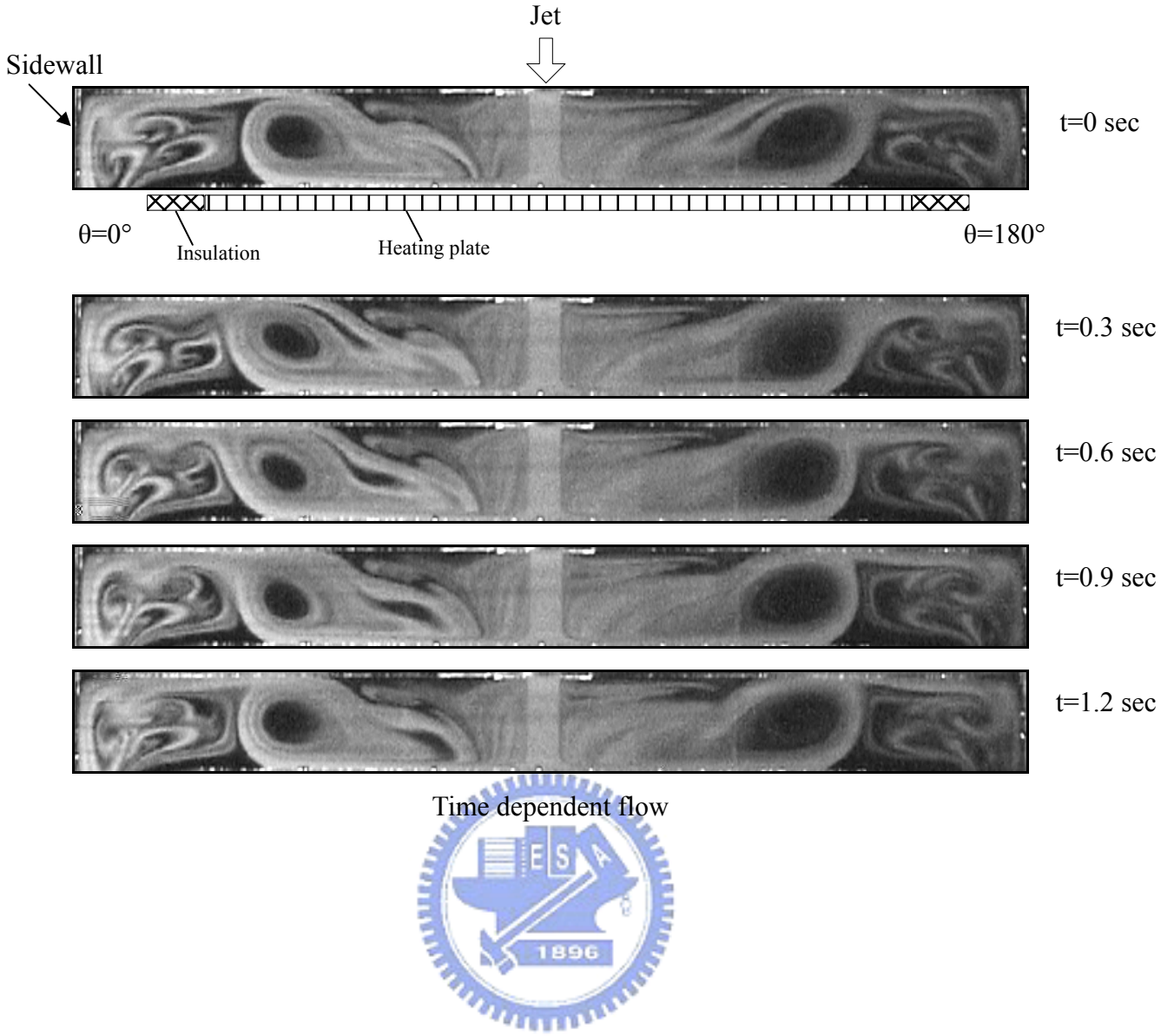

Fig. 4.30 Time-periodic vortex flow for H=30.0 mm and Ra=12,680 ($\Delta T = 5.0$℃) at Re_j=879 (Q_j=6.5 slpm) illustrated by side view flow photos taken at the vertical plane $\theta = 0°$ & $\theta = 180°$ at selected time instants in a typical periodic cycle (t_p=1.23 sec).

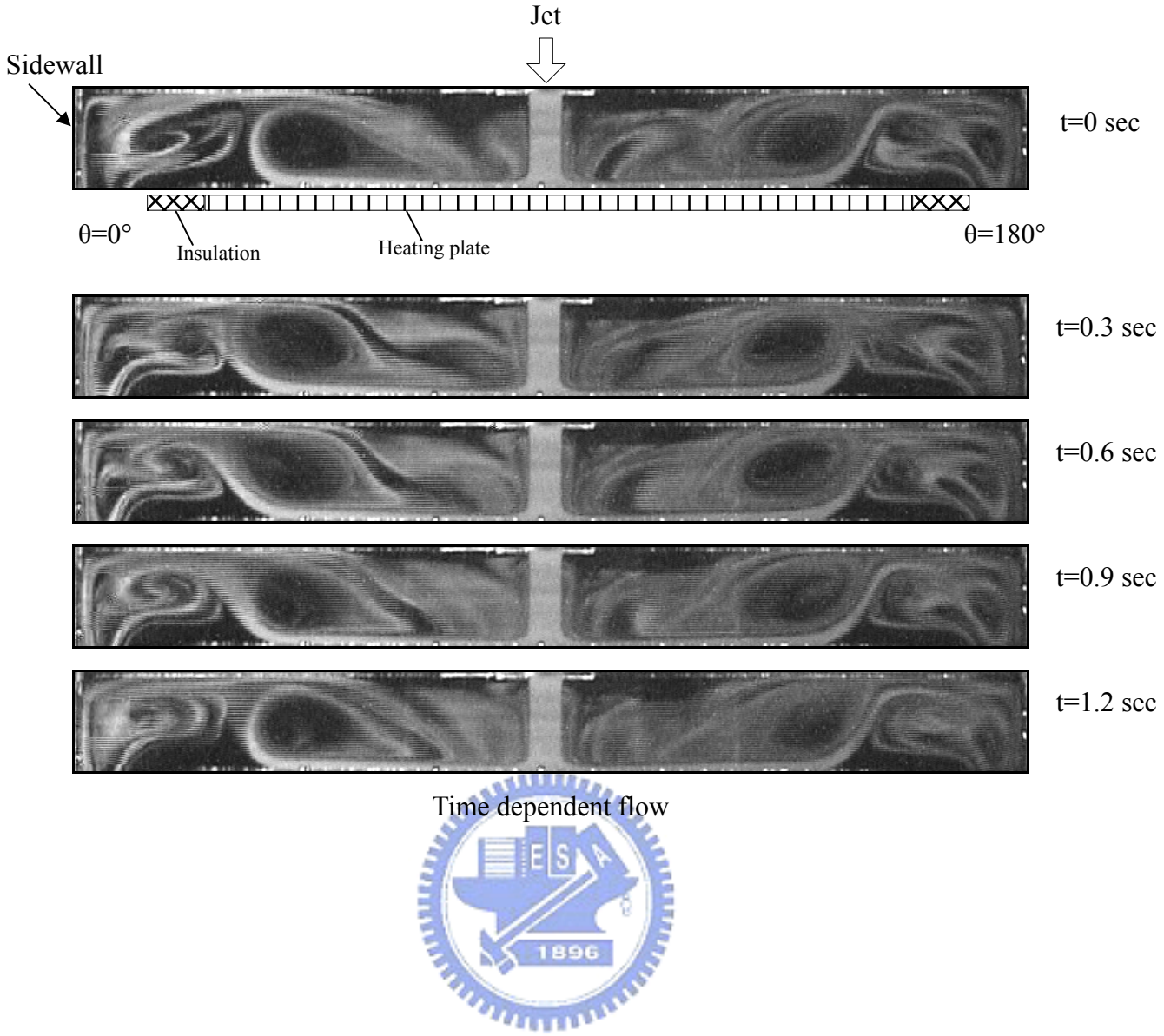

Fig. 4.31 Time-periodic vortex flow for H=30.0 mm and Ra=25,370 ($\Delta T = 10.0$℃) at Re_j=879 (Q_j=6.5 slpm) illustrated by side view flow photos taken at the vertical plane $\theta = 0°$ & $\theta = 180°$ at selected time instants in a typical periodic cycle (t_p=1.23 sec).

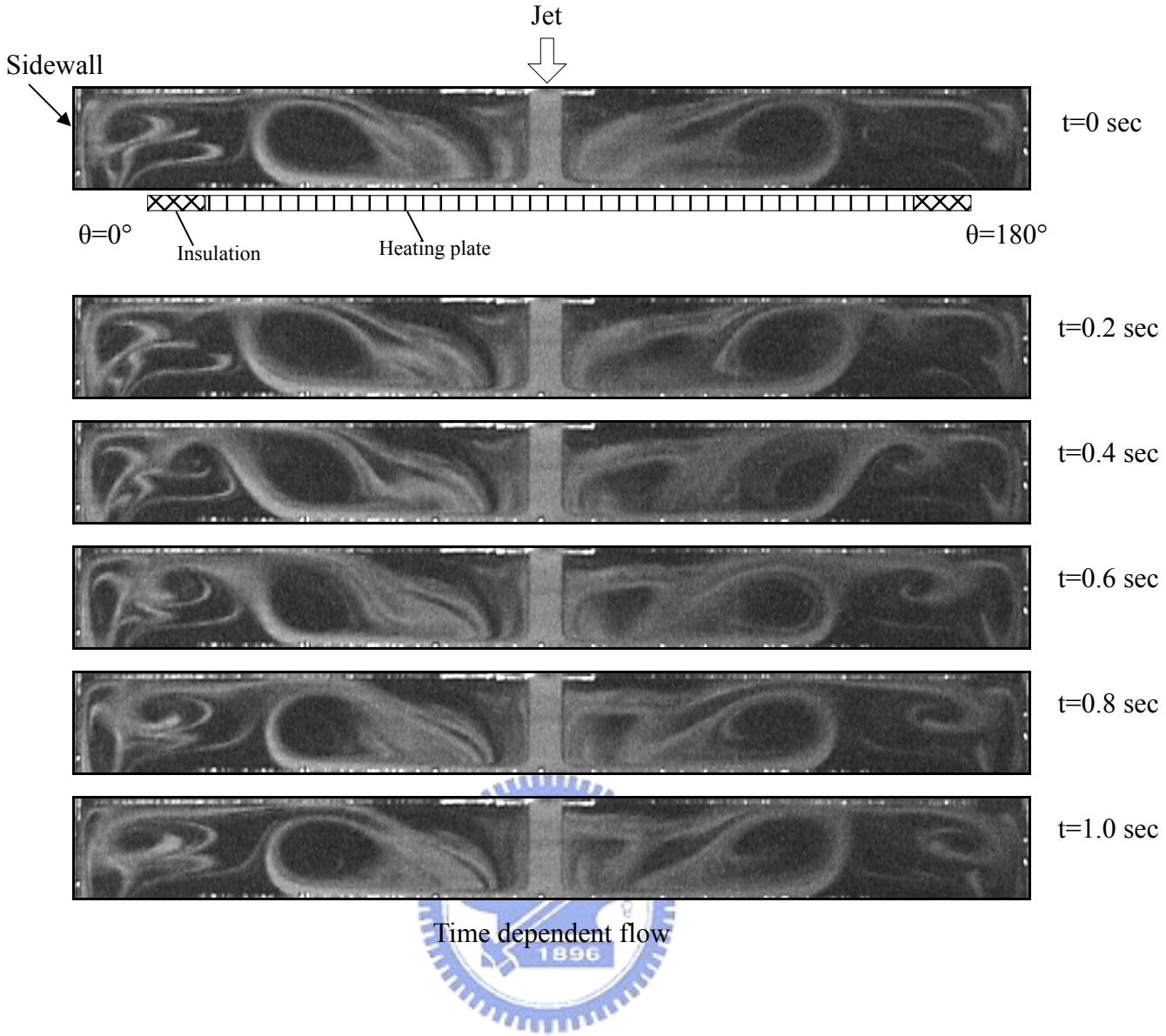

Fig. 4.32 Time-periodic vortex flow for H=30.0 mm and Ra=38,050 ($\Delta T = 15.0$℃) at Re_j=879 (Q_j=6.5 slpm) illustrated by side view flow photos taken at the vertical plane $\theta = 0°$ & $\theta = 180°$ at selected time instants in a typical periodic cycle (t_p=1.17 sec).

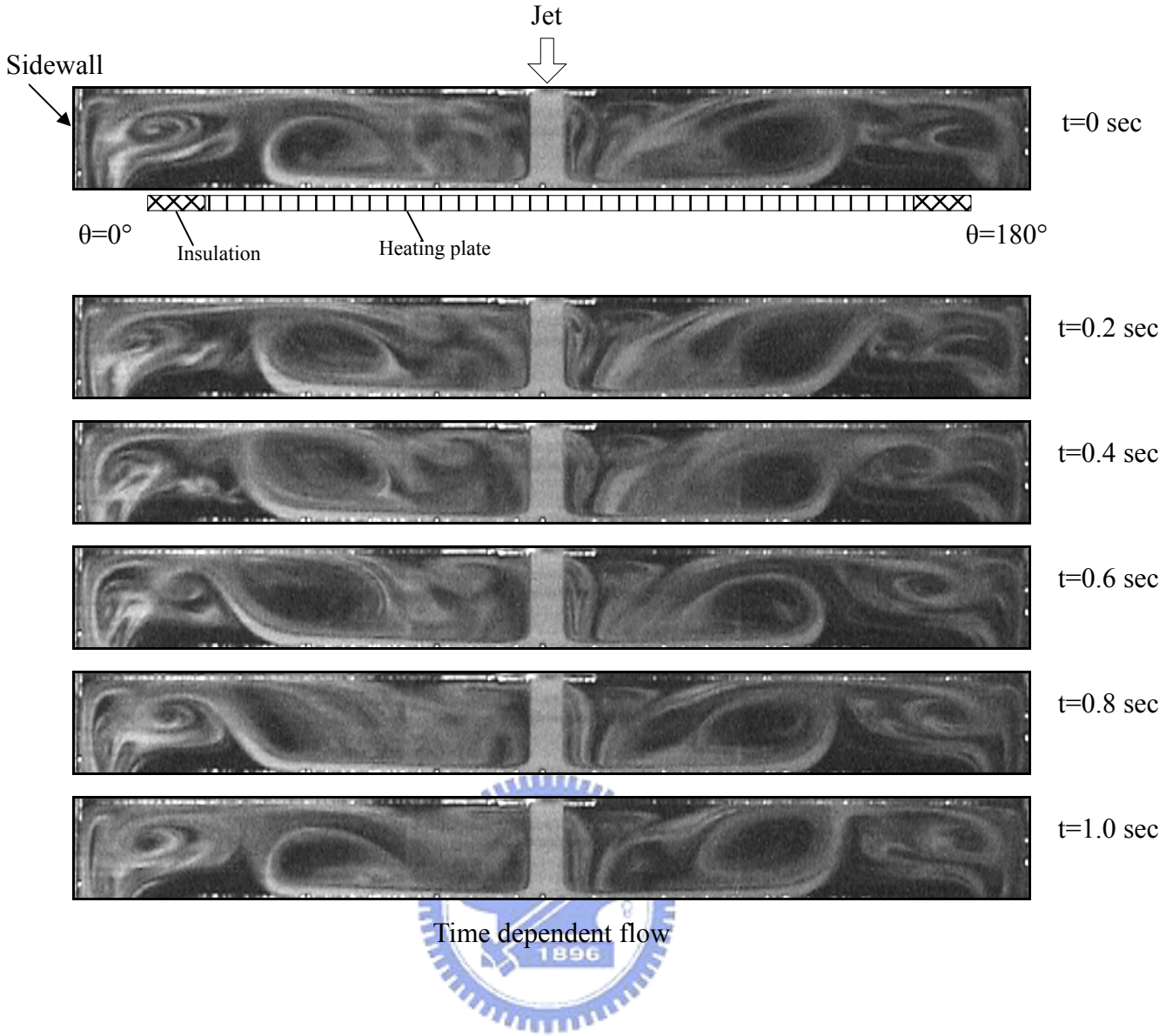

Fig. 4.33 Time-periodic vortex flow for H=30.0 mm and Ra=50,730 ($\Delta T = 20.0$℃) at Re_j=879 (Q_j=6.5 slpm) illustrated by side view flow photos taken at the vertical plane $\theta = 0°$ & $\theta = 180°$ at selected time instants in a typical periodic cycle (t_p=1.11 sec).

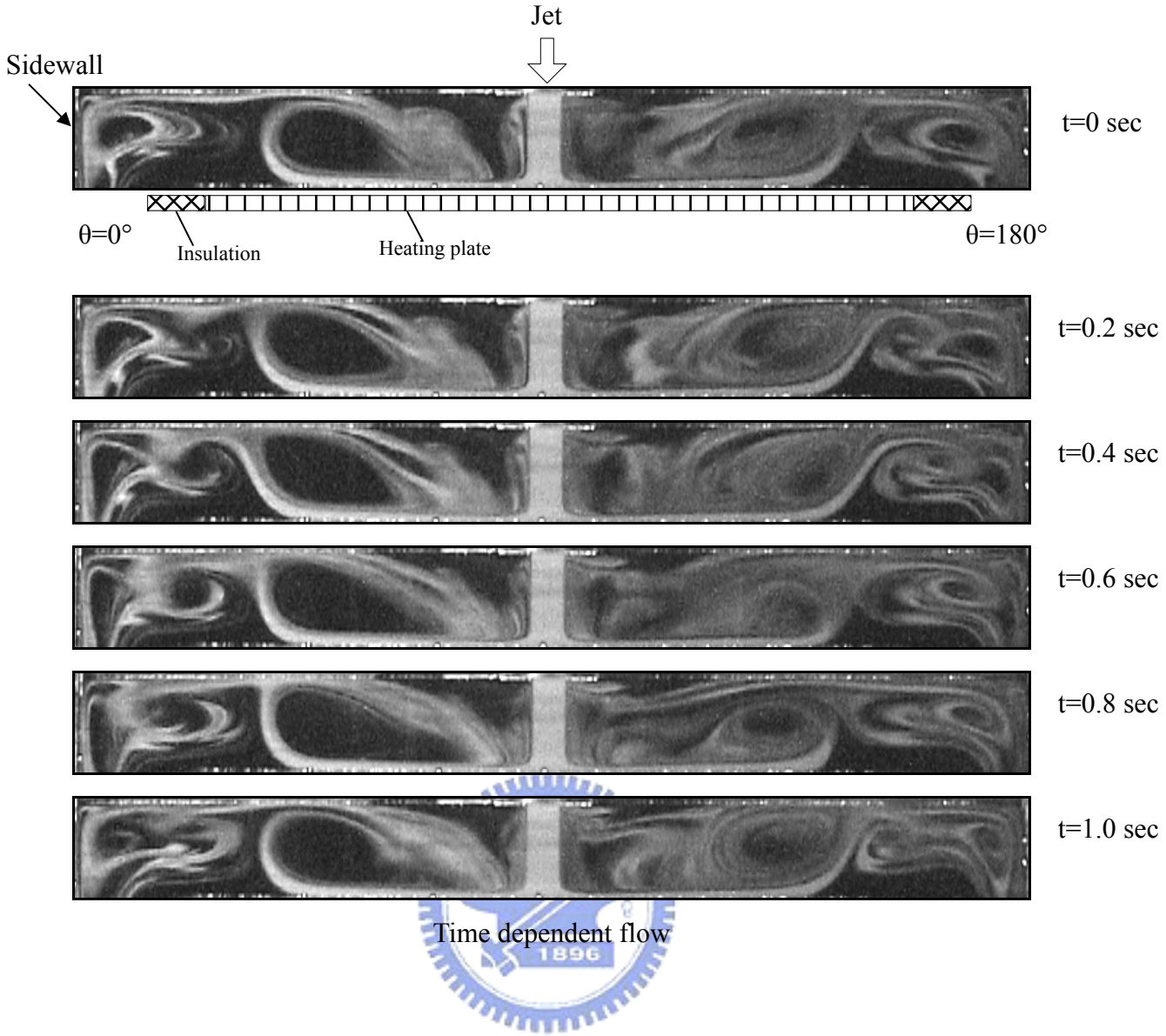

Fig. 4.34 Time-periodic vortex flow for H=30.0 mm and Ra=63,420 ($\Delta T = 25.0$℃) at Re_j=879 (Q_j=6.5 slpm) illustrated by side view flow photos taken at the vertical plane $\theta = 0°$ & $\theta = 180°$ at selected time instants in a typical periodic cycle (t_p=1.11 sec).

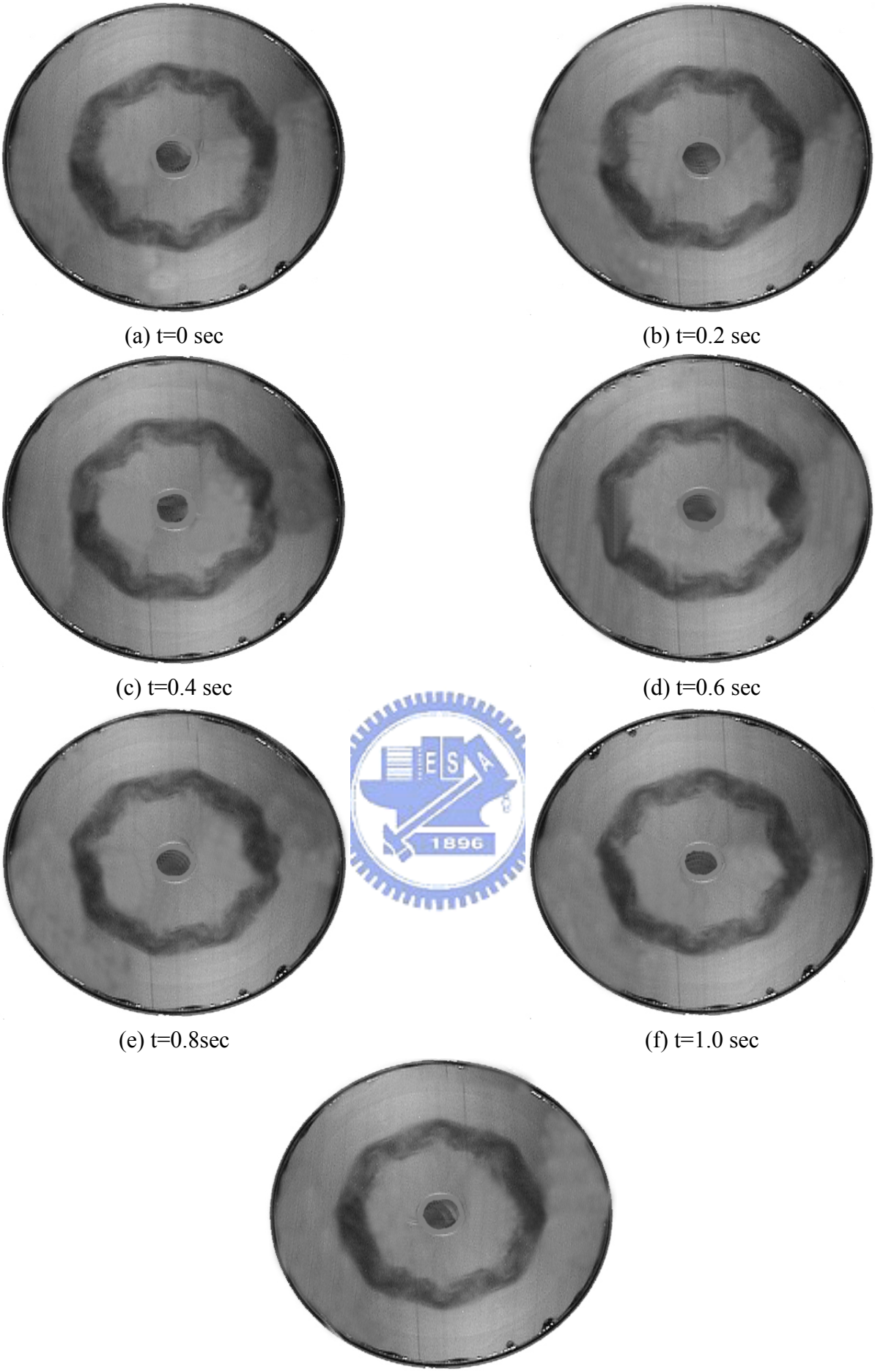

(a) t=0 sec (b) t=0.2 sec

(c) t=0.4 sec (d) t=0.6 sec

(e) t=0.8sec (f) t=1.0 sec

(g) t=1.3 sec

Fig. 4.35 Top view flow photos taken at selected time instants in a typical periodic cycle for Ra=0 (ΔT=0 ℃), Q=6.5 slpm (Re_j=879) and H=30.0 mm (t_p=1.33 sec).

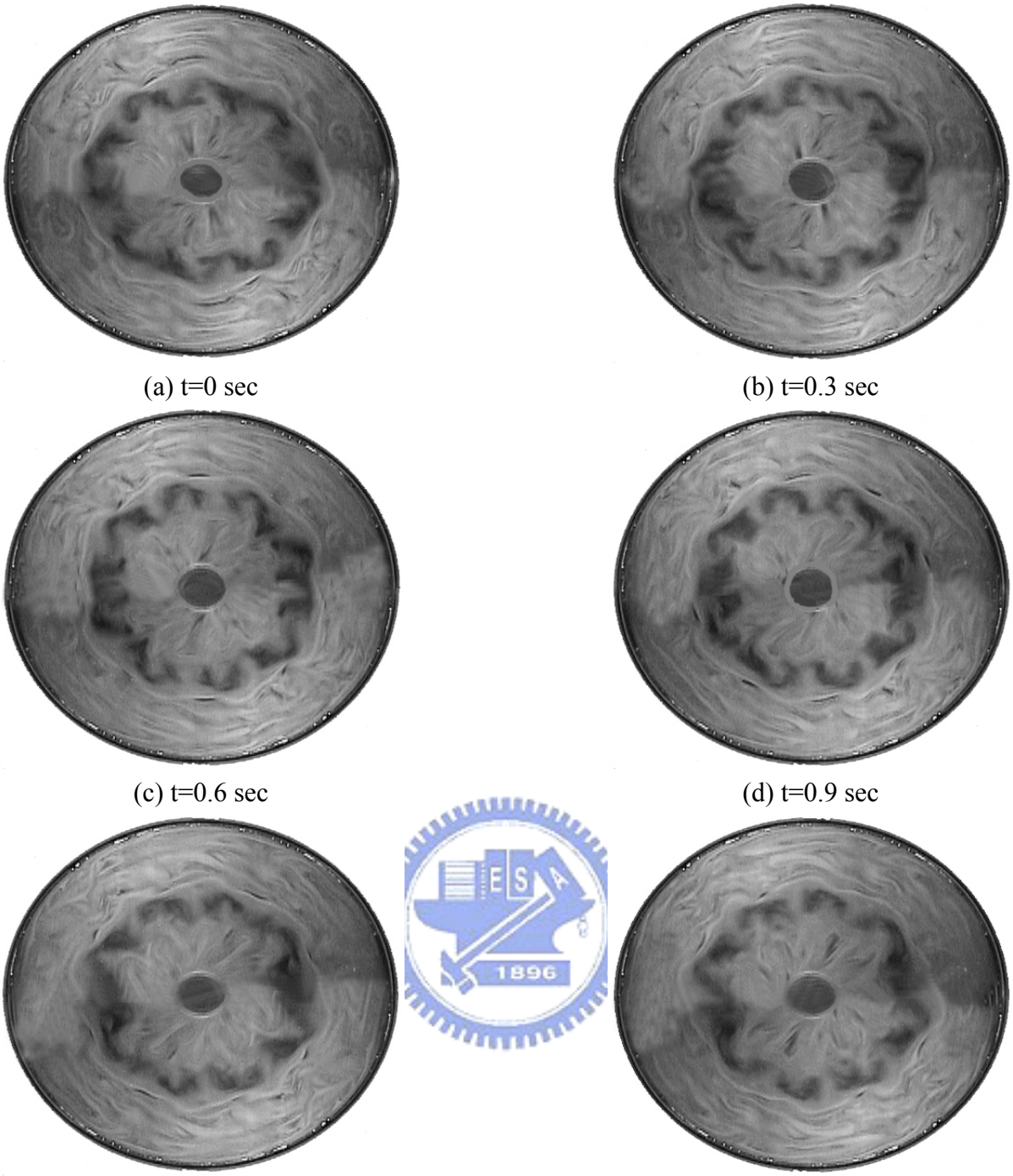

(a) t=0 sec (b) t=0.3 sec

(c) t=0.6 sec (d) t=0.9 sec

(e) t=1.0 sec (f) t=1.2 sec

Fig. 4.36 Top view flow photos taken at selected time instants in a typical periodic cycle for Ra=12,680 (ΔT=5.0℃), Q=6.5 slpm (Re_j=879) and H=30.0 mm (t_p=1.23 sec).

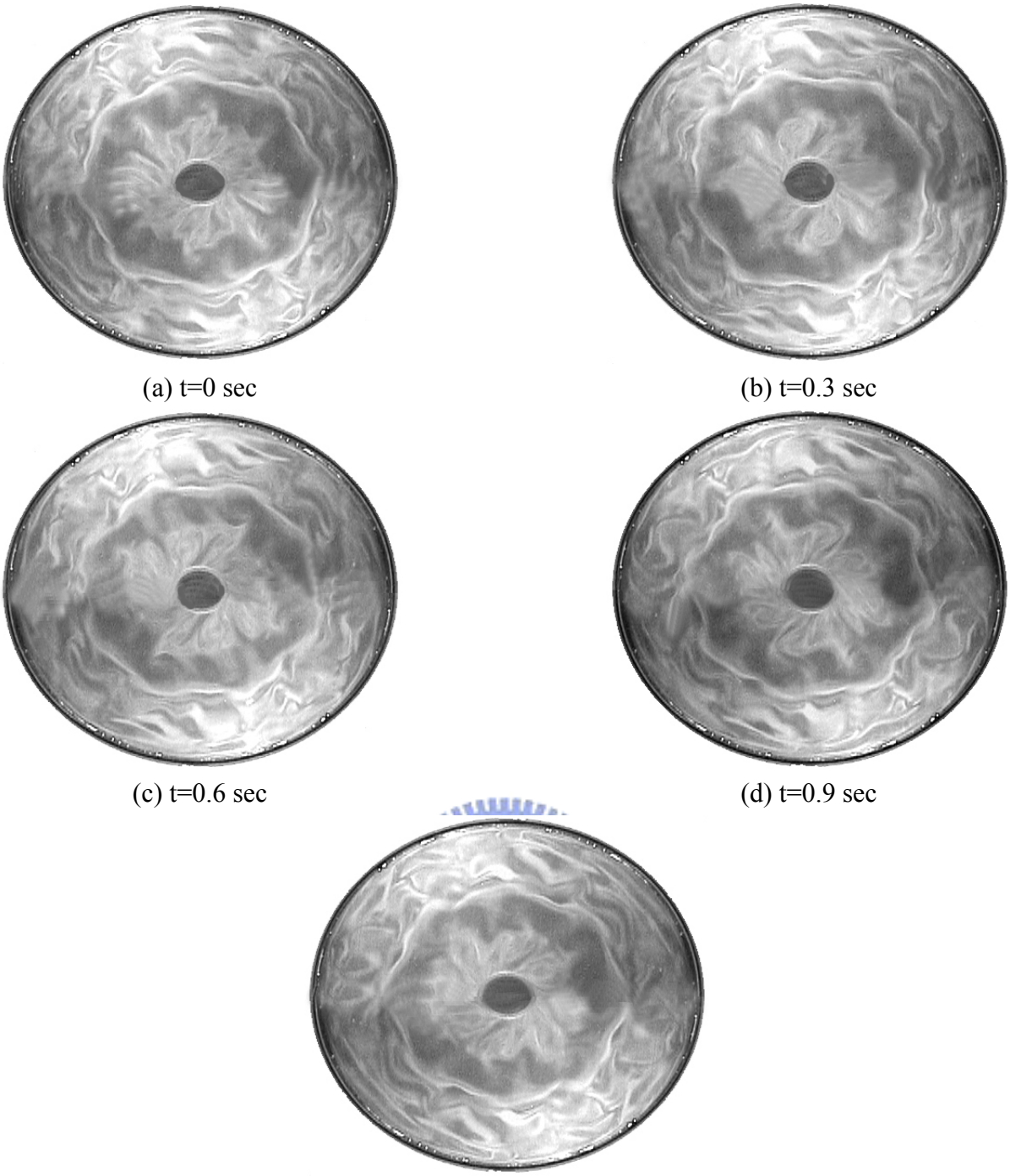

(a) t=0 sec (b) t=0.3 sec

(c) t=0.6 sec (d) t=0.9 sec

(e) t=1.2 sec

Fig. 4.37 Top view flow photos taken at selected time instants in a typical periodic cycle for Ra=25,370 (ΔT=10.0℃), Q=6.5 slpm (Re_j=879) and H=30.0 mm (t_p=1.23 sec).

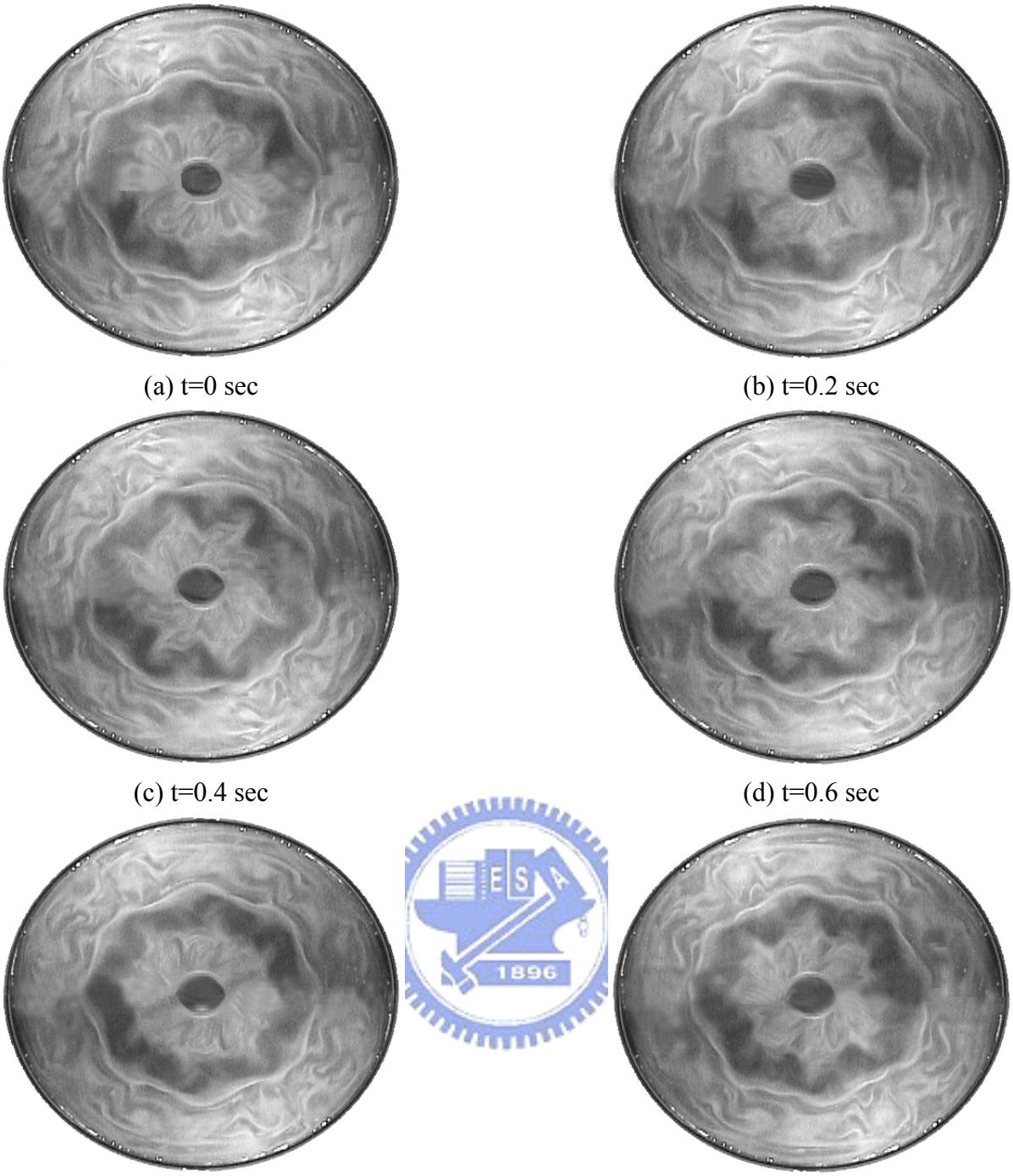

(a) t=0 sec (b) t=0.2 sec

(c) t=0.4 sec (d) t=0.6 sec

(e) t=0.8 sec (f) t=1.0 sec

Fig. 4.38 Top view flow photos taken at selected time instants in a typical periodic cycle for Ra=38,050 (ΔT=15.0℃), Q=6.5 slpm (Re_j=879) and H=30.0 mm (t_p=1.17 sec).

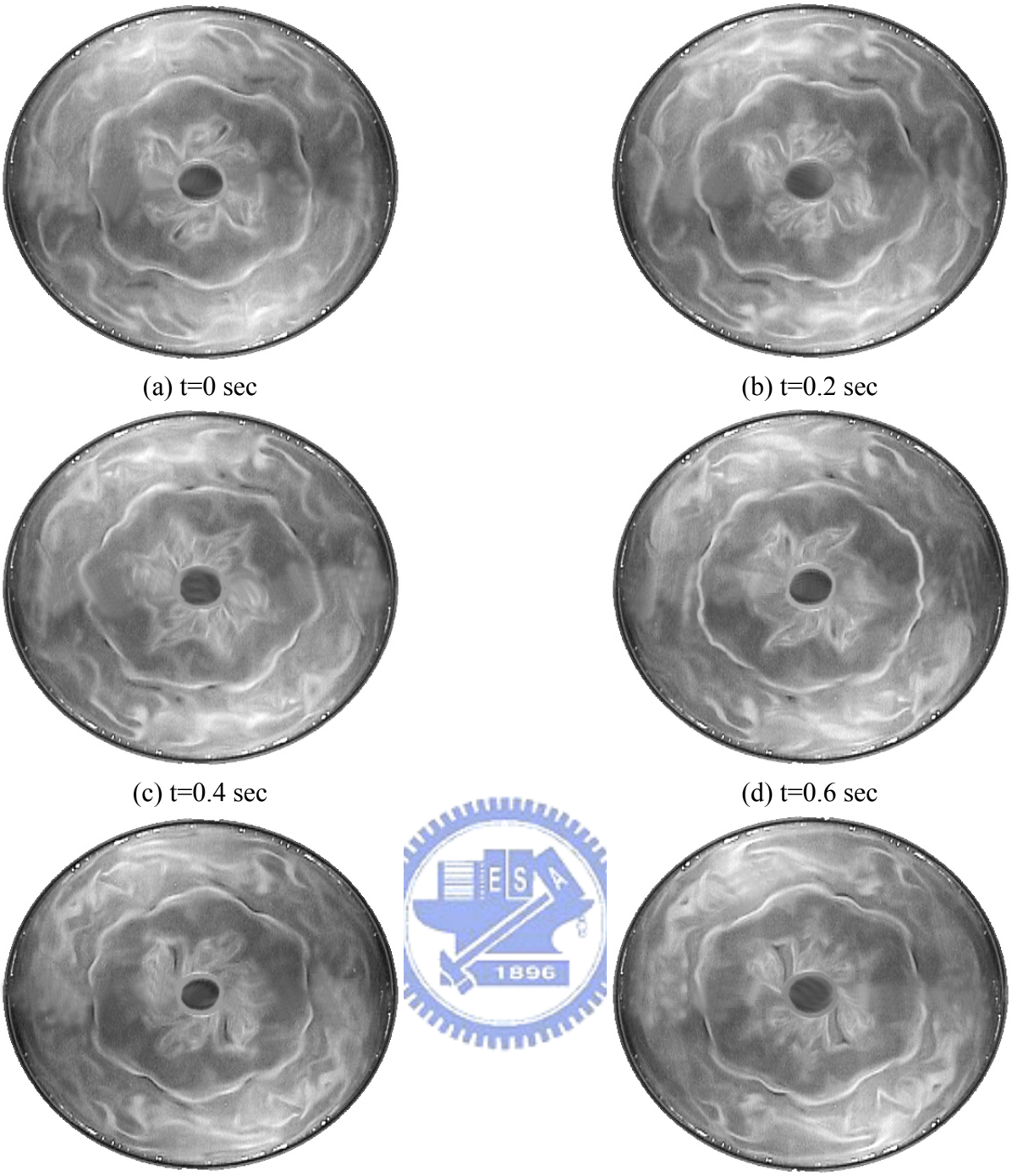

(a) t=0 sec (b) t=0.2 sec

(c) t=0.4 sec (d) t=0.6 sec

(e) t=0.8 sec (f) t=1.0 sec

Fig. 4.39 Top view flow photos taken at selected time instants in a typical periodic cycle for Ra=50,730 (ΔT=20.0℃), Q=6.5 slpm (Re_j=879) and H=30.0 mm (t_p=1.11 sec).

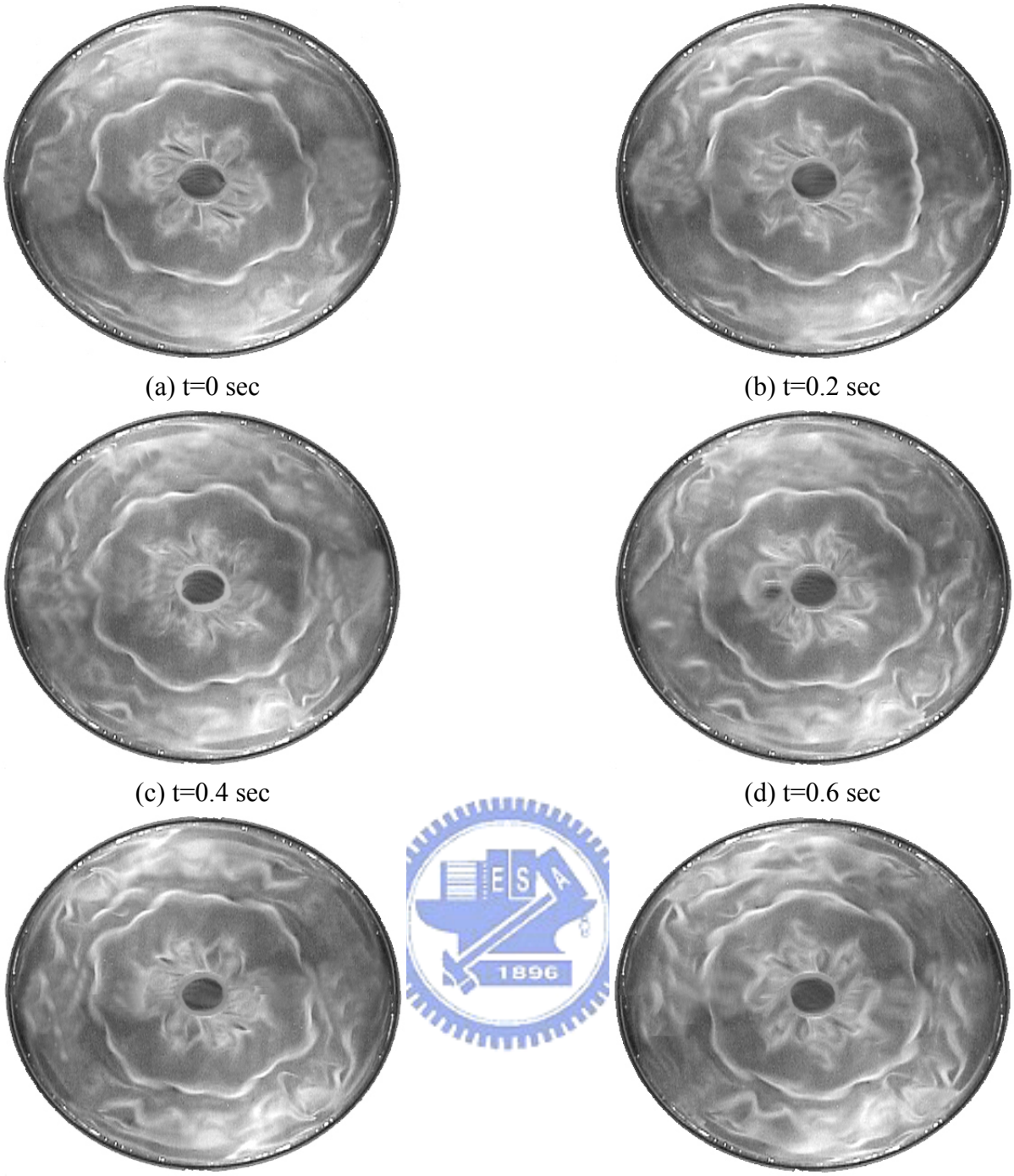

(a) t=0 sec (b) t=0.2 sec

(c) t=0.4 sec (d) t=0.6 sec

(e) t=0.8 sec (f) t=1.0 sec

Fig. 4.40 Top view flow photos taken at selected time instants in a typical periodic cycle for Ra=63,420 (ΔT=25.0℃), Q=6.5 slpm (Re_j=879) and H=30.0 mm (t_p=1.11 sec).

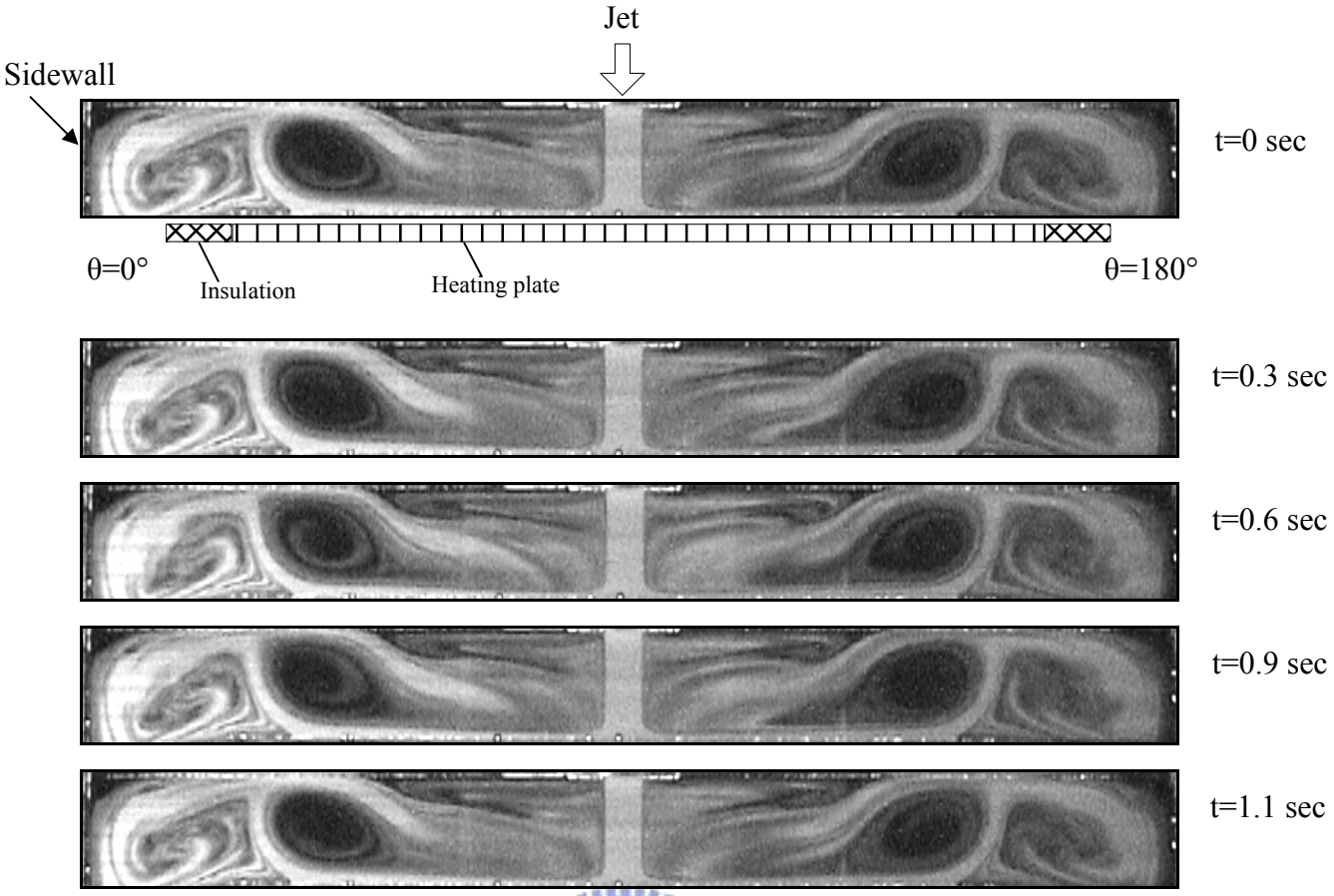

Fig. 4.41 Time-periodic vortex flow for H=30.0 mm and Ra=0 ($\Delta T = 0$℃) at Re_j=947 (Q_j=7.0 slpm) illustrated by side view flow photos taken at the vertical plane $\theta = 0°$ & $\theta = 180°$ at selected time instants in a typical periodic cycle (t_p=1.17 sec).

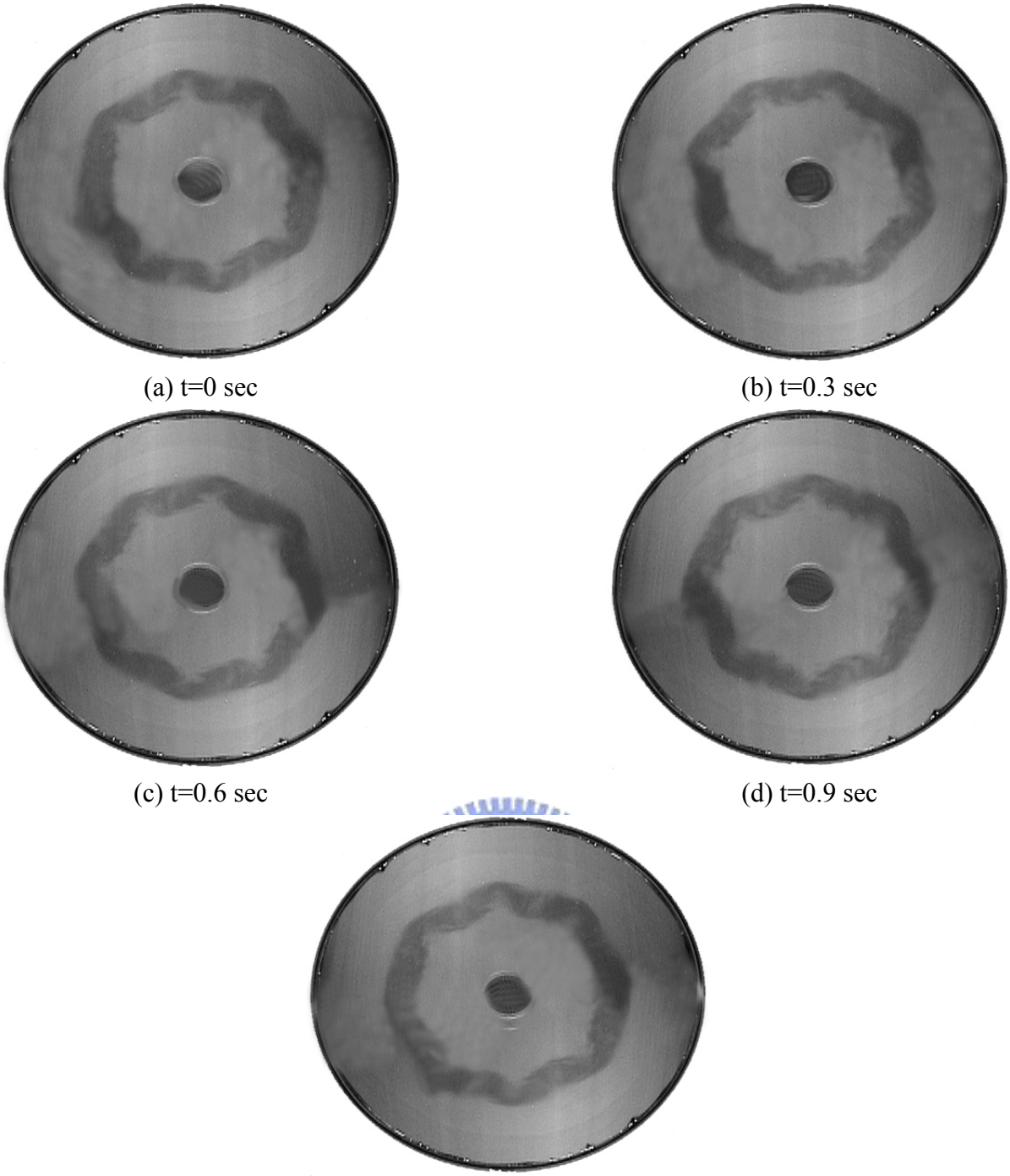

(a) t=0 sec (b) t=0.3 sec

(c) t=0.6 sec (d) t=0.9 sec

(g) t=1.1 sec

Fig. 4.42 Top view flow photos taken at selected time instants in a typical periodic cycle for Ra=0 (ΔT=0 ℃), Q=7.0 slpm (Re_j=947) and H=30.0 mm (t_p=1.17 sec).

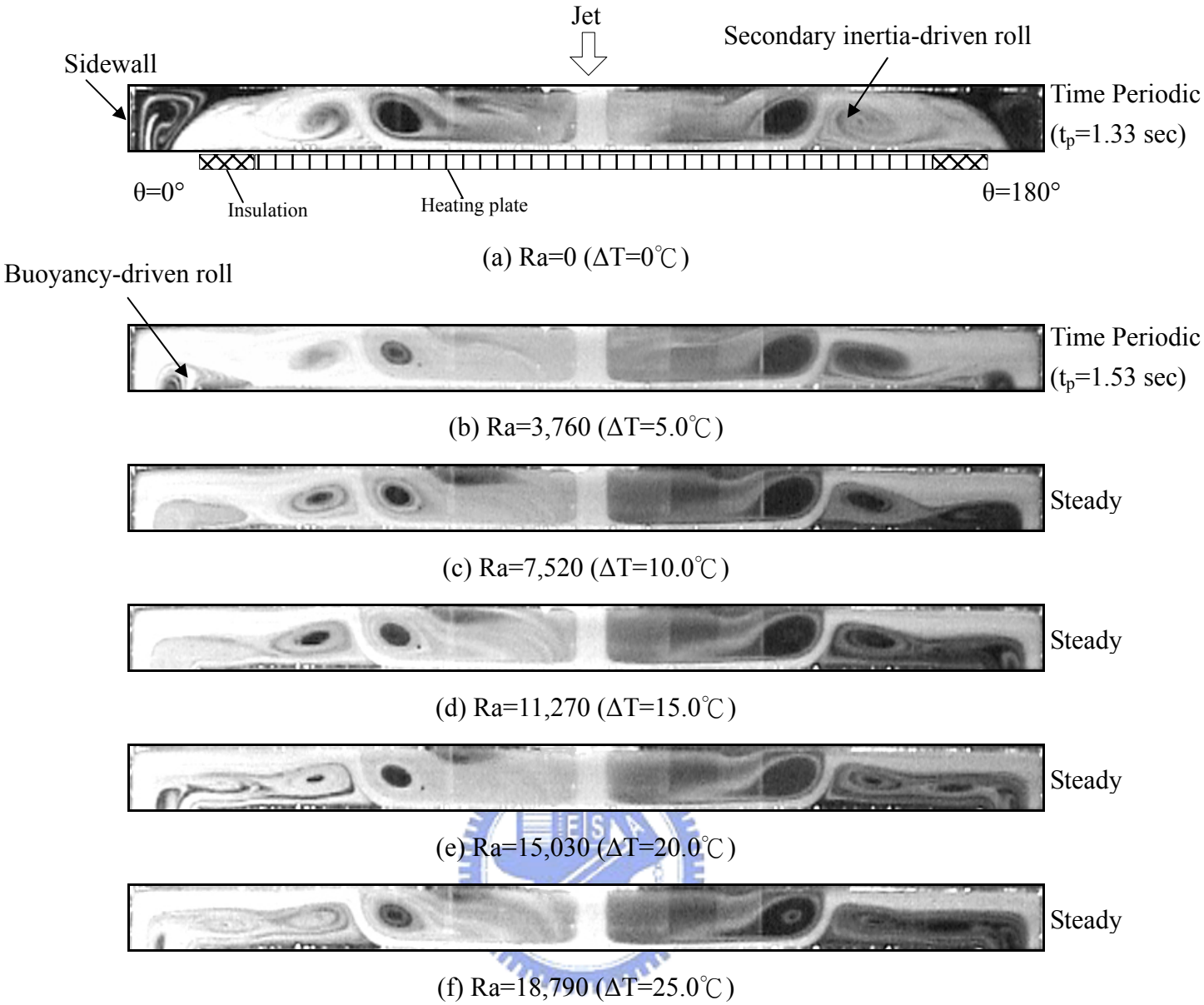

Fig. 4.43 Side view flow photos taken at the cross plane θ=0° & 180° at steady state or at certain instant in the statistical state for Re_j=879 (Q_j=6.5 slpm) with various Ra at H=20.0mm.

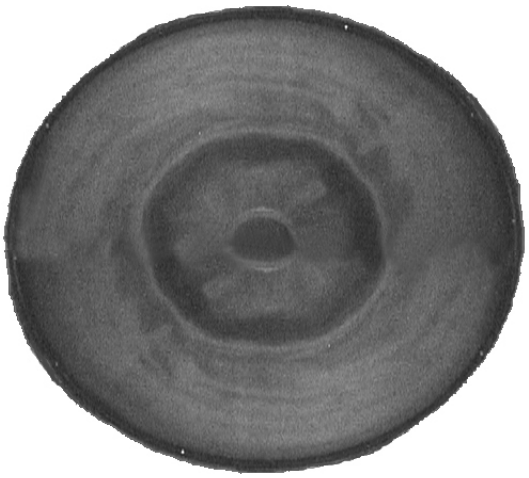

(a) Ra=0 (ΔT=0℃) & Time Periodic (t_p=1.33 sec)

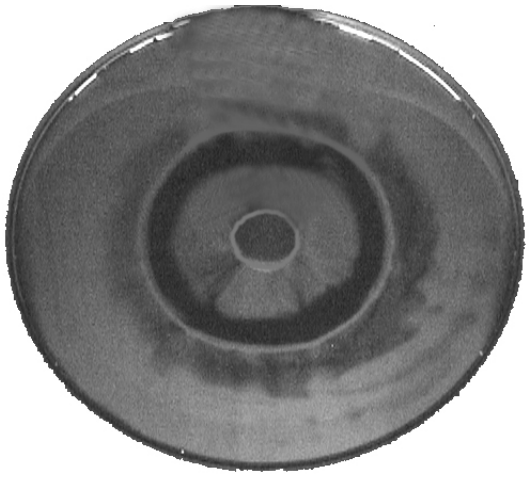

(b) Ra=3,760 (ΔT=5.0℃) & Time Periodic (t_p=1.53 sec)

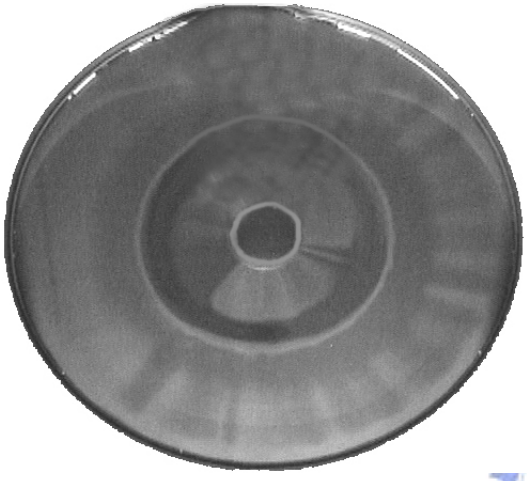

(c) Ra=7,520 (ΔT=10.0℃) & Steady

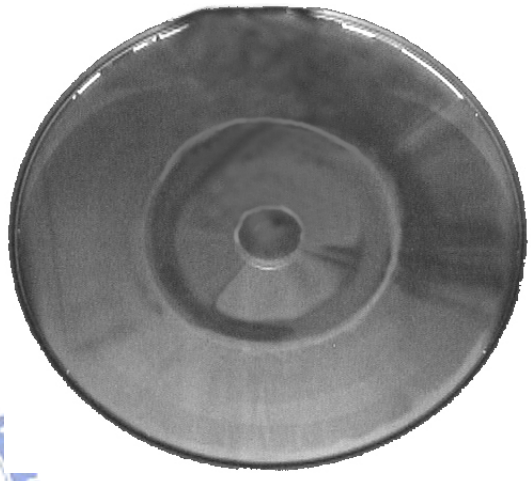

(d) Ra=11,270 (ΔT=15.0℃) & Steady

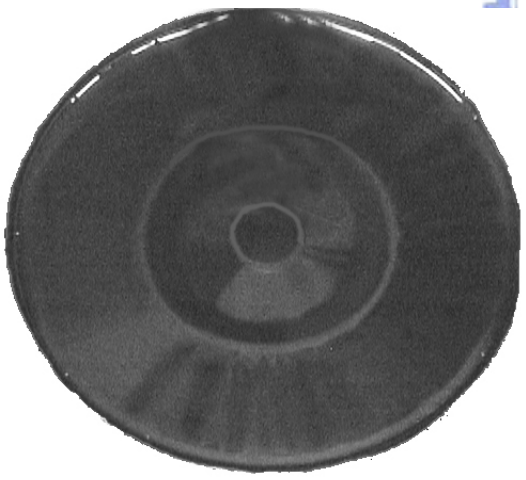

(e) Ra=15,030 (ΔT=20.0℃) & Steady

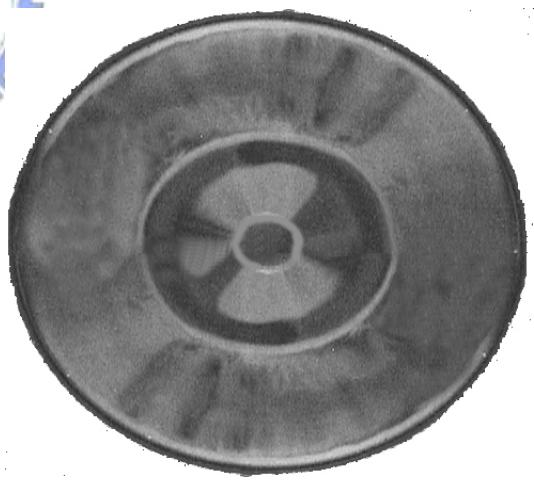

(f) Ra=18,790 (ΔT=25.0℃) & Steady

Fig. 4.44 Top view flow photos taken at midheight of the chamber at steady state or at certain instant in the statistical state for Re_j=879 (Q_j=6.5 slpm) and H=20.0 mm for various Ra.

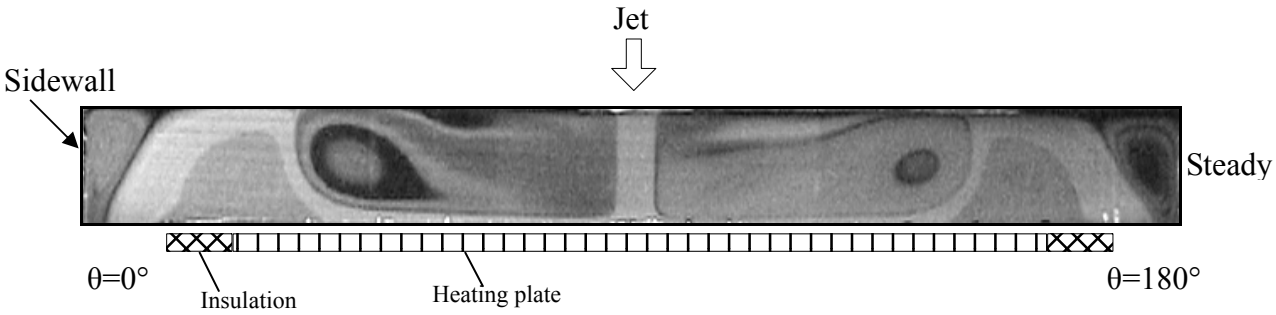

(a) Ra=0 (ΔT=0℃)

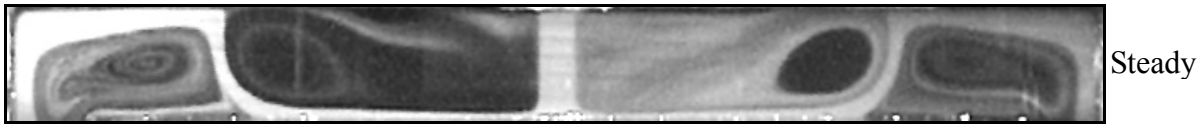

(b) Ra=12,680 (ΔT=5.0℃)

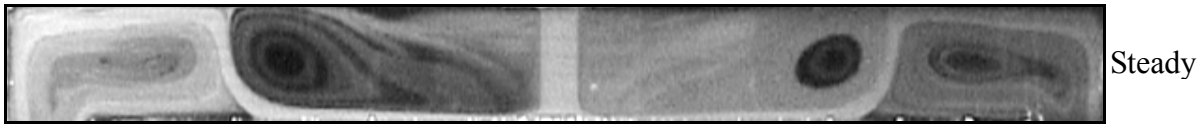

(c) Ra=25,370 (ΔT=10.0℃)

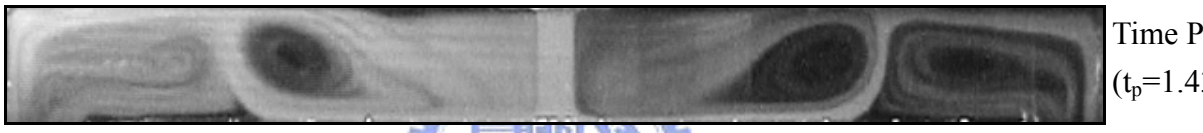

(d) Ra=38,050 (ΔT=15.0℃)

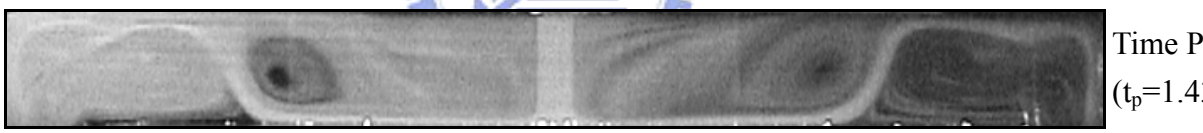

(e) Ra=50,730 (ΔT=20.0℃)

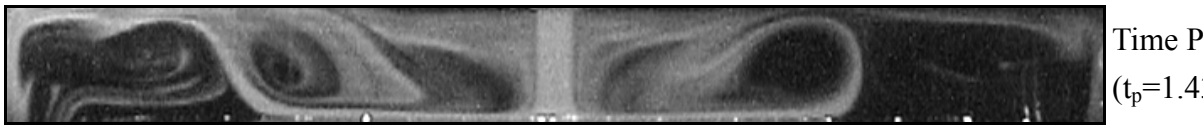

(f) Ra=63,420 (ΔT=25.0℃)

Fig. 4.45 Side view flow photos taken at the cross plane θ=0° & 180° at steady state or at certain instant in the statistical state for Re_j=676 (Q_j=5.0 slpm) with various Ra at H=30.0mm.

(a) Ra=12,680 (ΔT=5.0℃) & Steady

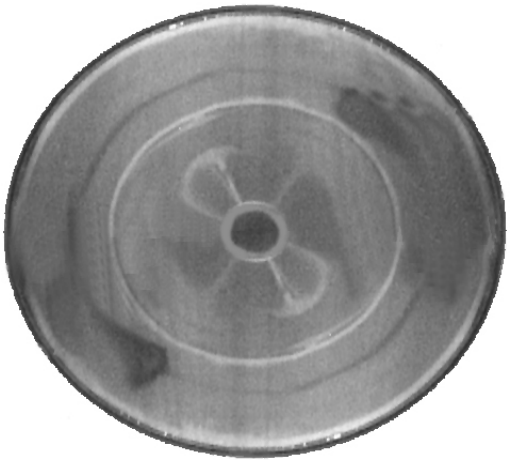

(b) Ra=25,370 (ΔT=10.0℃) & Steady

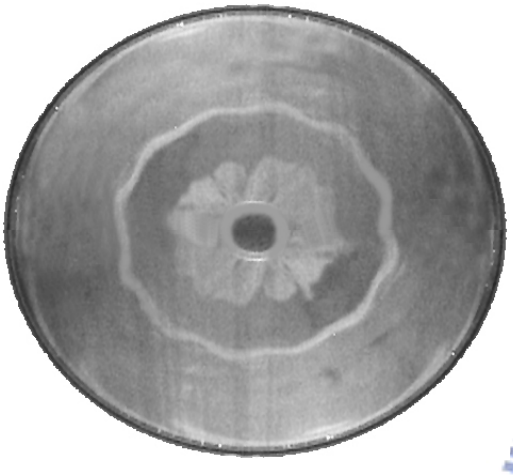

(c) Ra=38,050 (ΔT=15.0℃) & Time Periodic (t_p=1.43 sec)

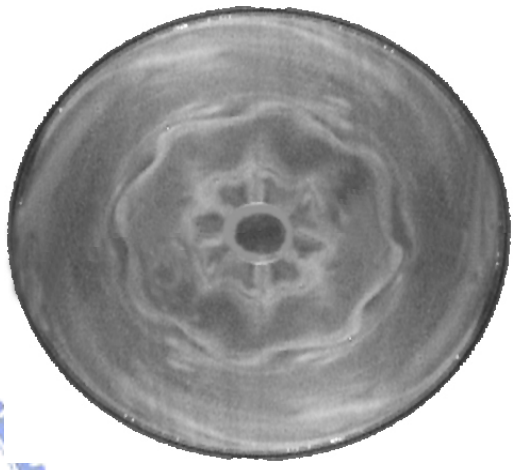

(d) Ra=50,730 (ΔT=20.0℃) & Time Periodic (t_p=1.43 sec)

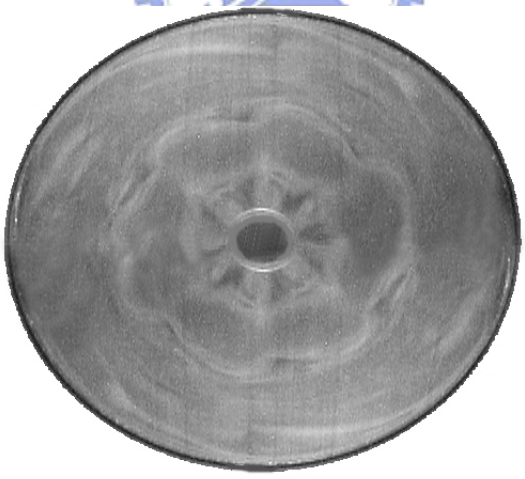

(e) Ra=63,420 (ΔT=25.0℃) & Time Periodic (t_p=1.43 sec)

Fig. 4.46 Top view flow photos taken at midheight of the chamber at steady state or at certain instant in the statistical state for Re_j=676 (Q_j=5.0 slpm) and H=30.0 mm for various Ra.

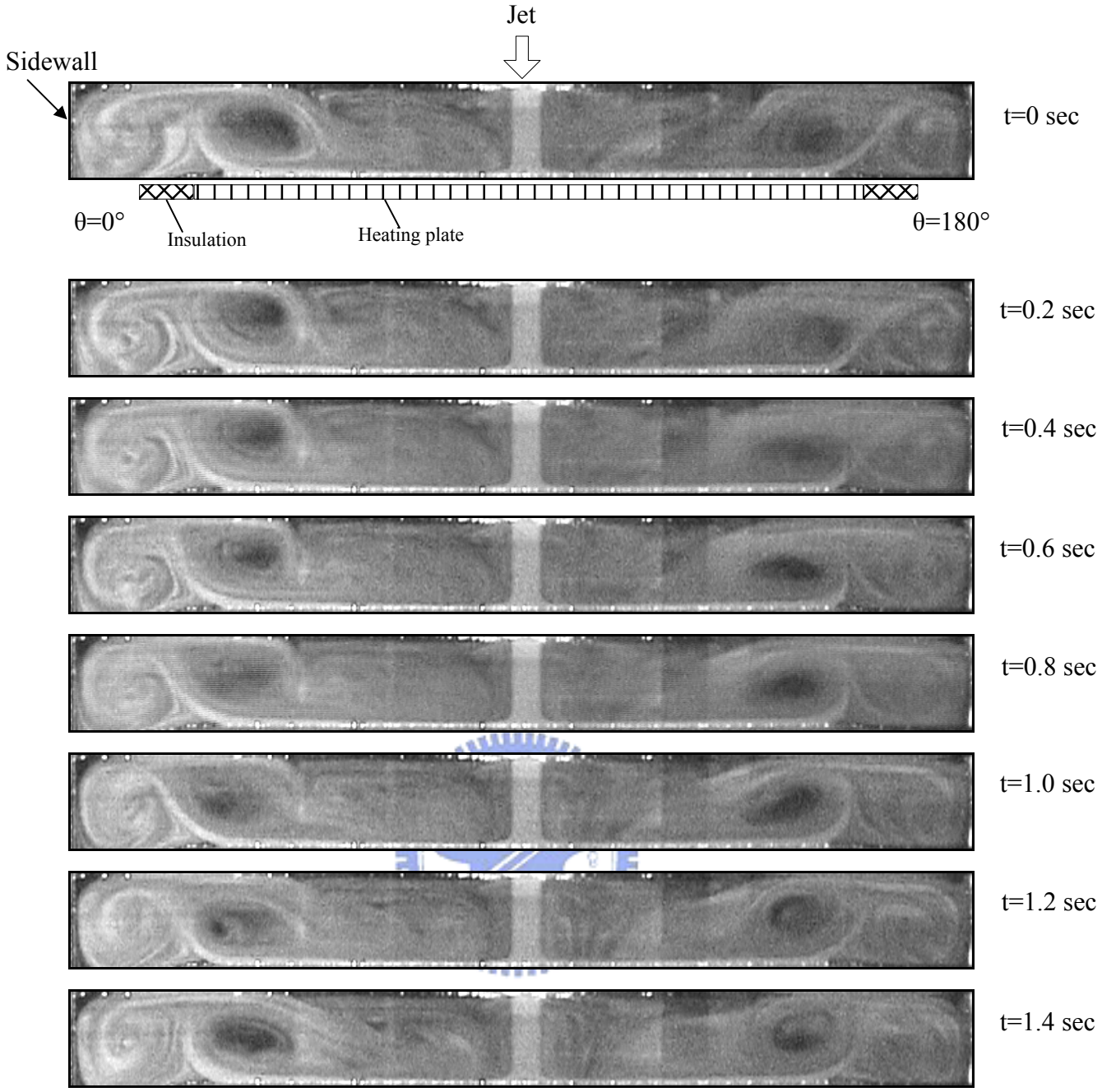

Inertia-driven nonperiodic flow

Fig. 4.47 Nonperiodic vortex flow for H=30.0 mm and Ra=0 ($\Delta T = 0$℃) at Re_j=1,217 (Q_j=9.0 slpm) illustrated by side view flow photos taken at the vertical plane $\theta = 0°$ & $\theta = 180°$ at selected time instants.

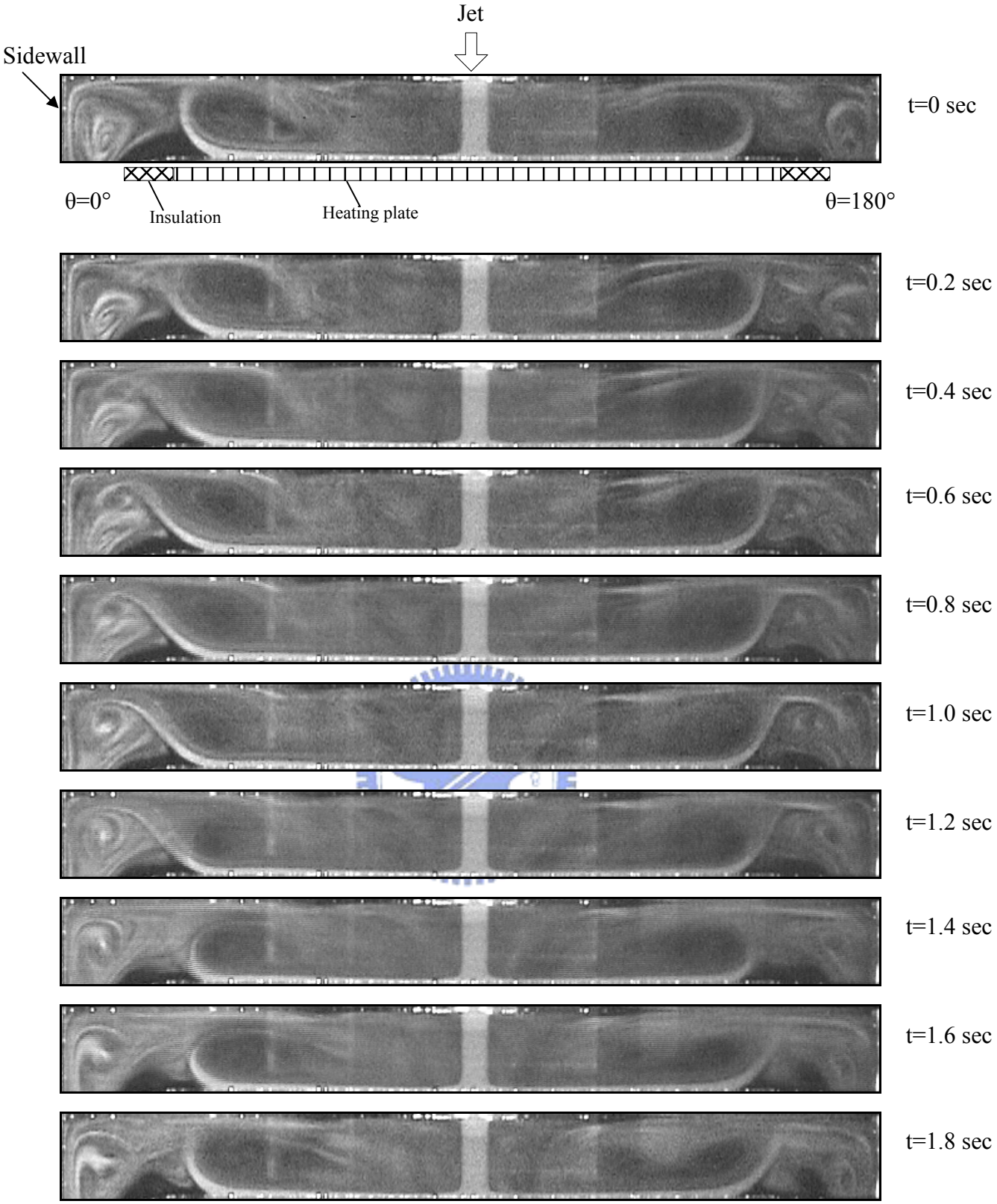

Inertia-driven nonperiodic flow

Fig. 4.48 Nonperiodic vortex flow for H=30.0 mm and Ra=38,050 ($\Delta T = 15.0$℃) at Re_j=1,217 (Q_j=9.0 slpm) illustrated by side view flow photos taken at the vertical plane $\theta = 0°$ & $\theta = 180°$ at selected time instants.

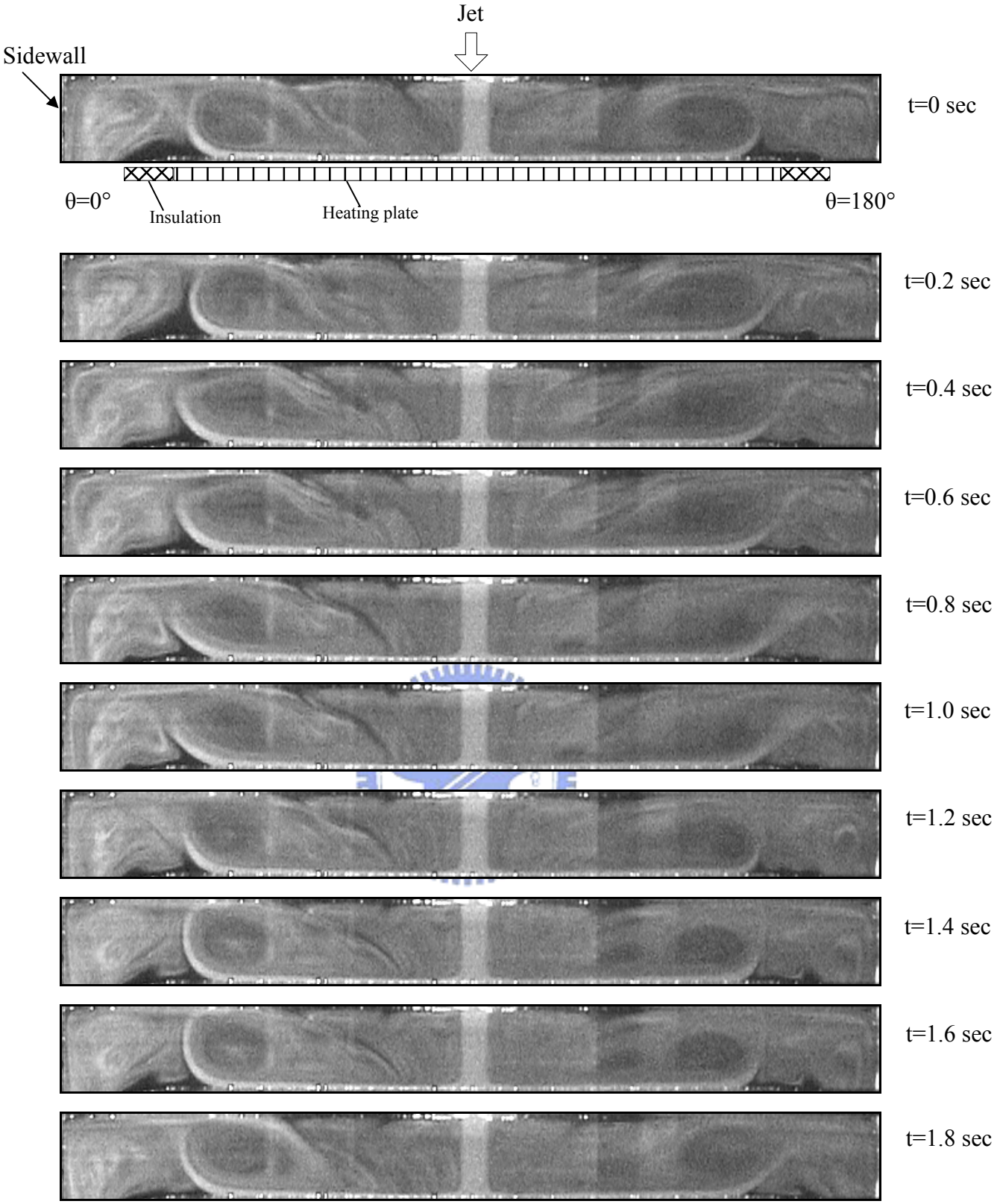

Inertia-driven nonperiodic flow

Fig. 4.49 Nonperiodic vortex flow for H=30.0 mm and Ra=38,050 ($\Delta T = 15.0$℃) at Re_j=1,285 (Q_j=9.5 slpm) illustrated by side view flow photos taken at the vertical plane $\theta = 0°$ & $\theta = 180°$ at selected time instants.

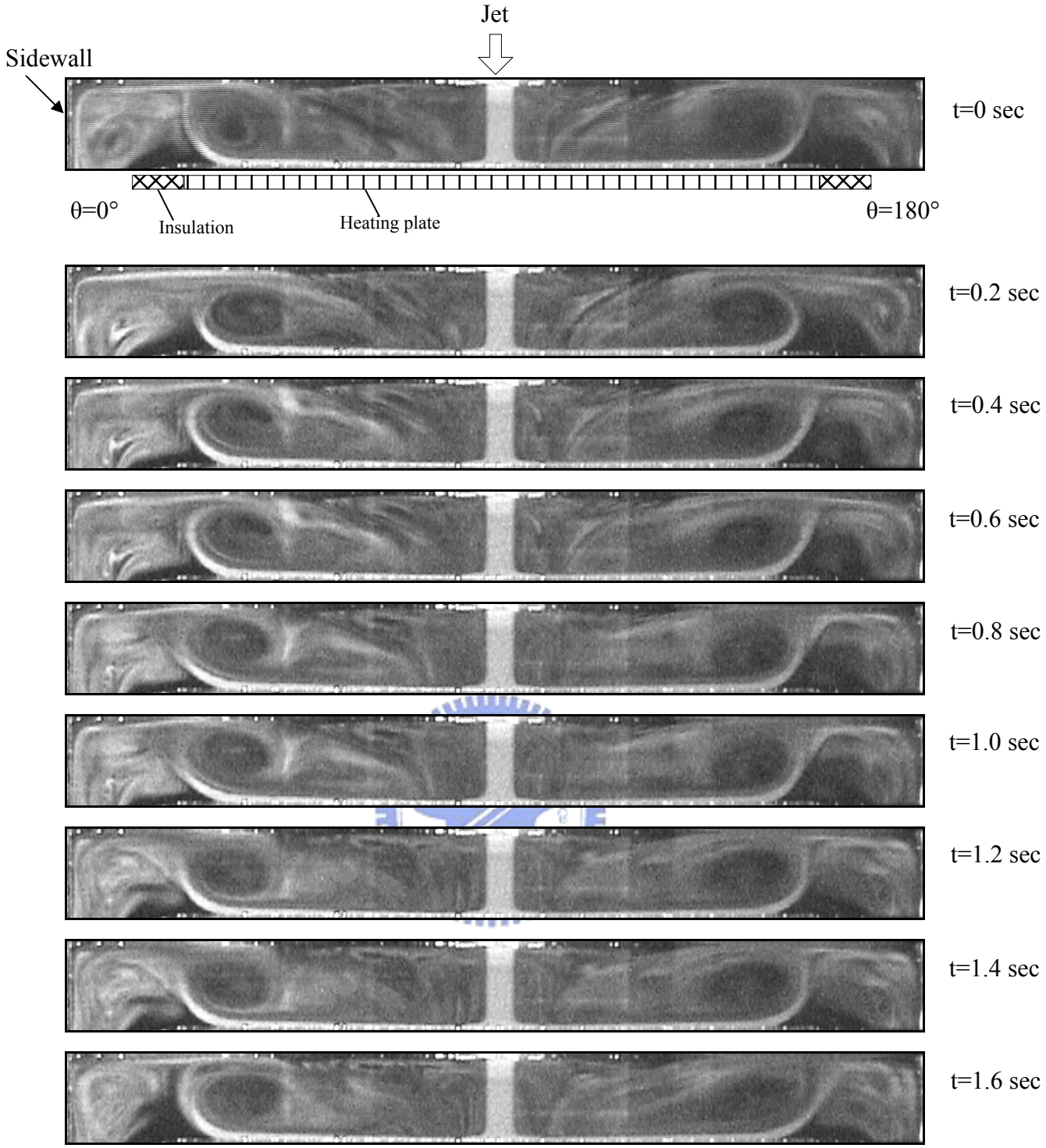

Inertia-driven nonperiodic flow

Fig. 4.50 Nonperiodic vortex flow for H=30.0 mm and Ra=38,050 ($\Delta T = 15.0$℃) at Re_j=1,352 (Q_j=10.0 slpm) illustrated by side view flow photos taken at the vertical plane $\theta = 0°$ & $\theta = 180°$ at selected time instants.

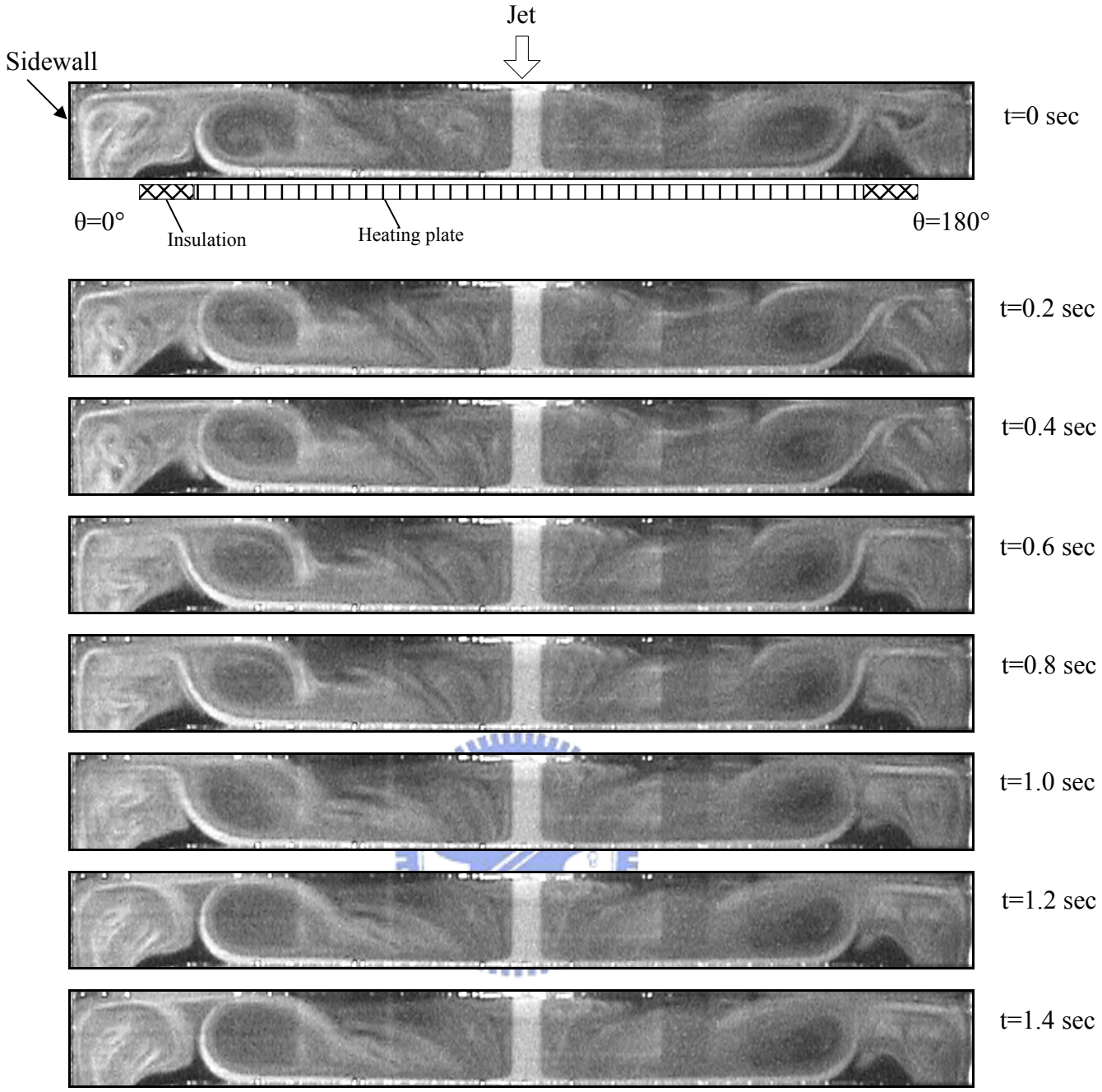

Inertia-driven nonperiodic flow

Fig. 4.51 Nonperiodic vortex flow for H=30.0 mm and Ra=38,050 ($\Delta T = 15.0$℃) at Re_j=1,420 (Q_j=10.5 slpm) illustrated by side view flow photos taken at the vertical plane $\theta = 0°$ & $\theta = 180°$ at selected time instants.

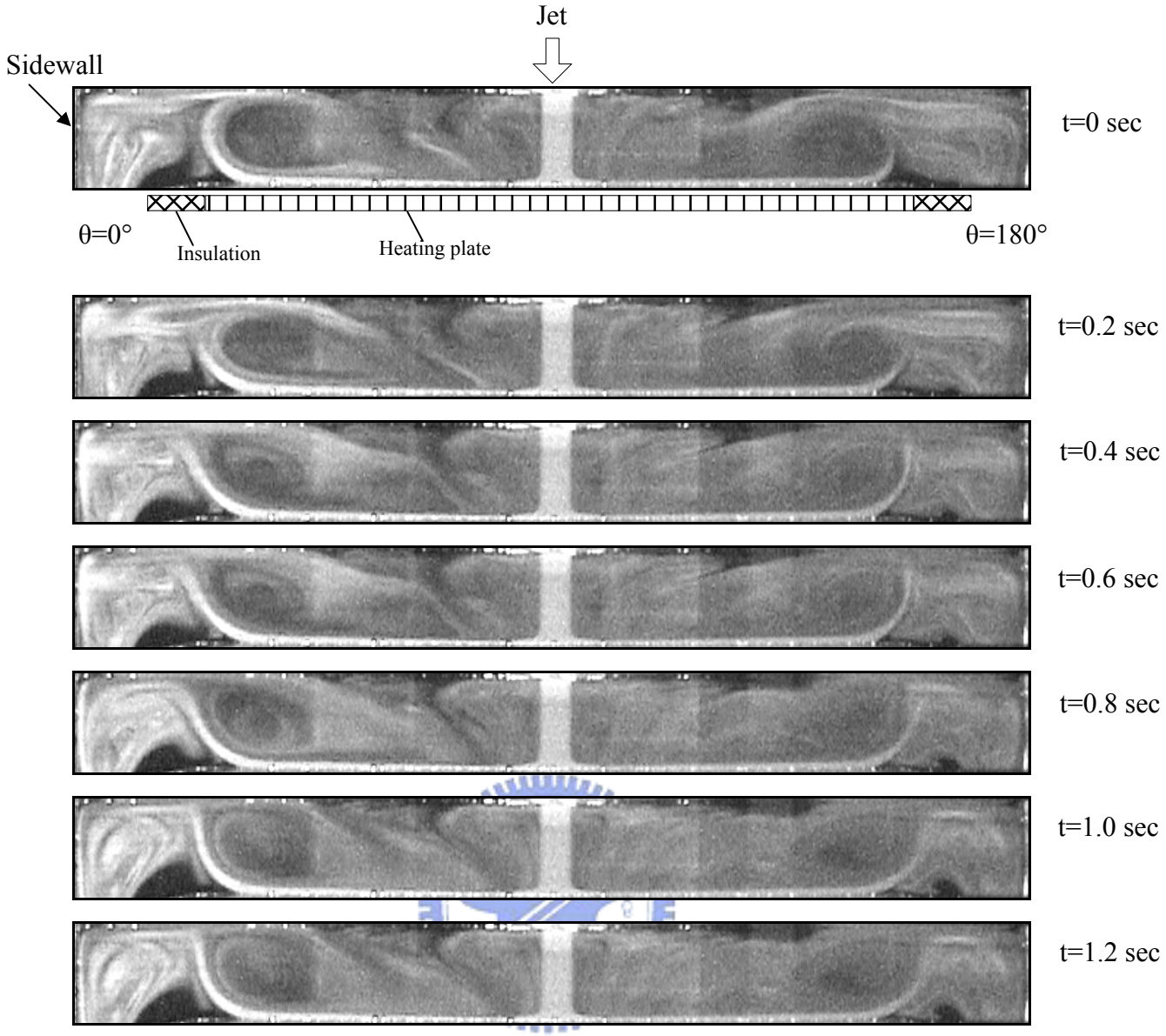

Inertia-driven nonperiodic flow

Fig. 4.52 Nonperiodic vortex flow for H=30.0 mm and Ra=38,050 ($\Delta T = 15.0$℃) at Re_j=1,488 (Q_j=11.0 slpm) illustrated by side view flow photos taken at the vertical plane $\theta = 0°$ & $\theta = 180°$ at selected time instants.

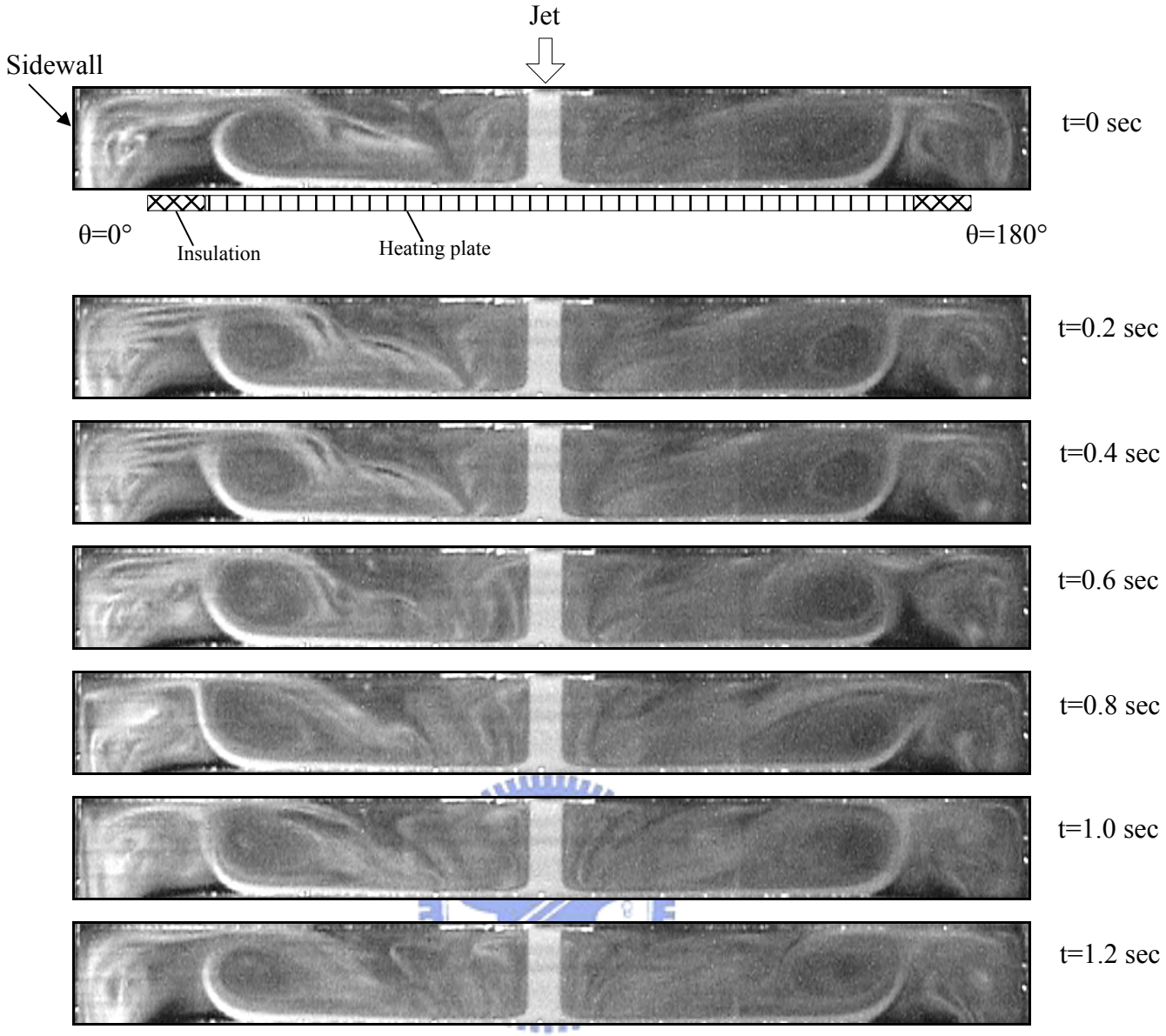

Inertia-driven nonperiodic flow

Fig. 4.53 Nonperiodic vortex flow for H=30.0 mm and Ra=38,050 ($\Delta T = 15.0$℃) at Re_j=1,623 (Q_j=12.0 slpm) illustrated by side view flow photos taken at the vertical plane $\theta = 0°$ & $\theta = 180°$ at selected time instants.

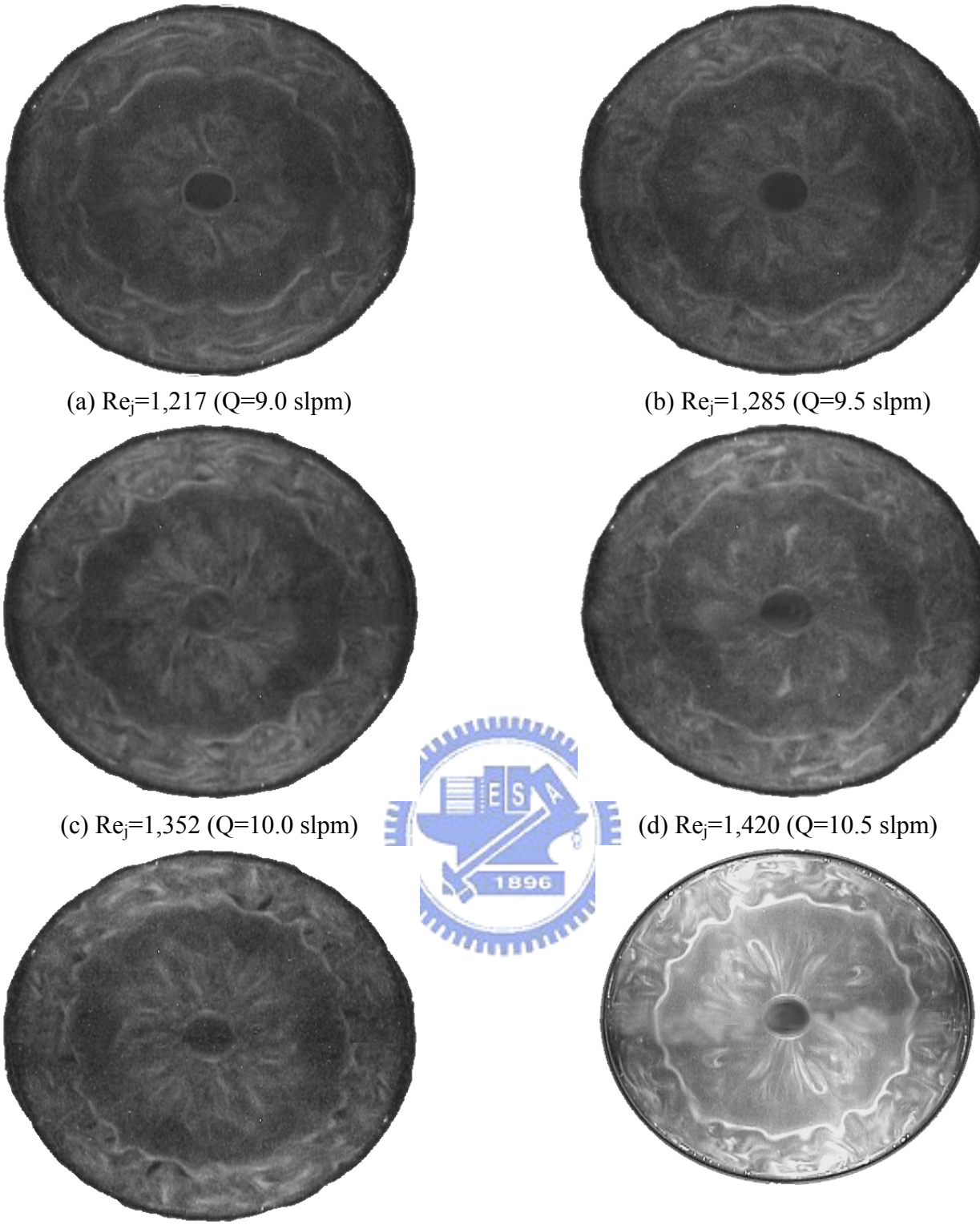

(a) Re_j=1,217 (Q=9.0 slpm)

(b) Re_j=1,285 (Q=9.5 slpm)

(c) Re_j=1,352 (Q=10.0 slpm)

(d) Re_j=1,420 (Q=10.5 slpm)

(e) Re_j=1,488 (Q=11.0 slpm)

(f) Re_j=1,623 (Q=12.0 slpm)

Fig. 4.54 Top view flow photos taken at midheight of the chamber with Ra=38,050 (ΔT=15.0℃) and D_j=10.0 mm at H=30.0 mm for Re_j=(a)1,217, (b)1,285, (c)1,352, (d)1,420, (e)1,488 and (f)1,623.

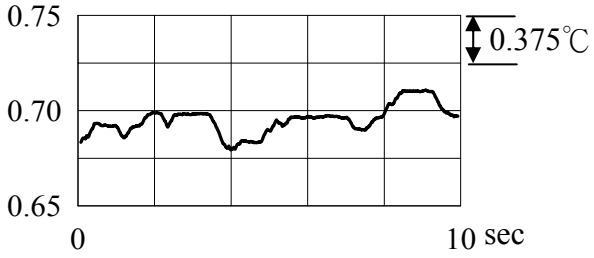

(a)Q_j=9.0 slpm

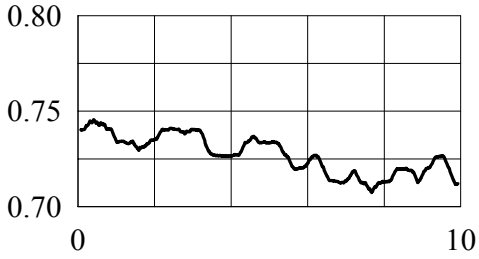

(b)Q=9.5 slpm

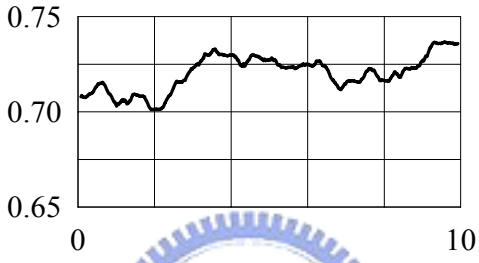

(c)Q=10.0 slpm

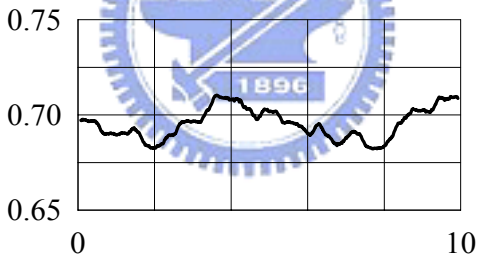

(d)Q=10.5 slpm

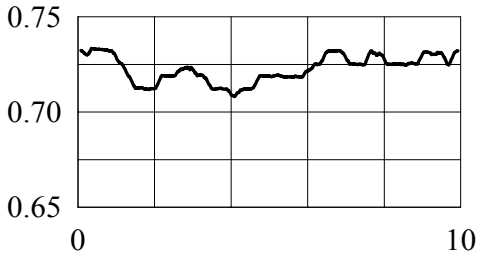

(e)Q=11.0 slpm

Fig. 4.55 The time records of non-dimensional air temperature for Ra=38,050 ($\Delta T = 15.0$℃) with H=30.0 mm at location (R, Z)=(0.68, 0.67) and $\theta = 0°$ for various Reynolds numbers Re_j= (a)1,217, (b)1,285, (c)1,352, (d)1,420 and (e)1,488.

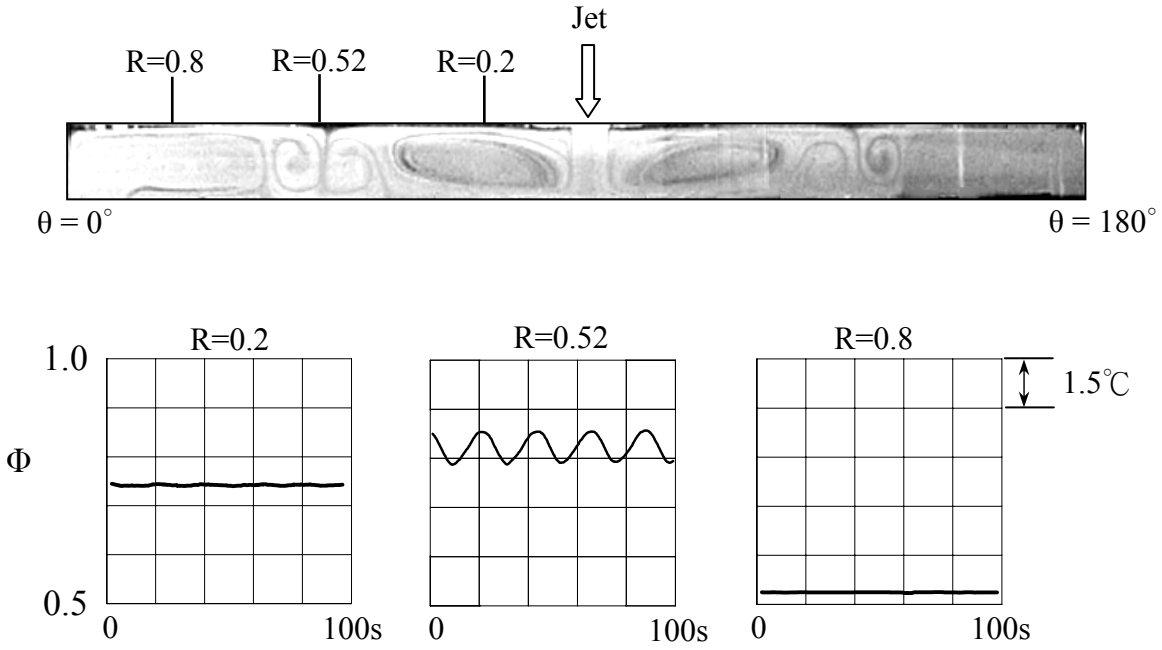

Fig. 4.56 Side view flow photos at the cross plane θ =0° & 180° at certain time instant in a typical periodic cycle and time records of air temperature at selected locations in the middle horizontal plane Z=0.5 with H=20.0 mm for Re_j=135, Ra=11,270 & D_j=10.0 mm (t_p=21.1 sec).

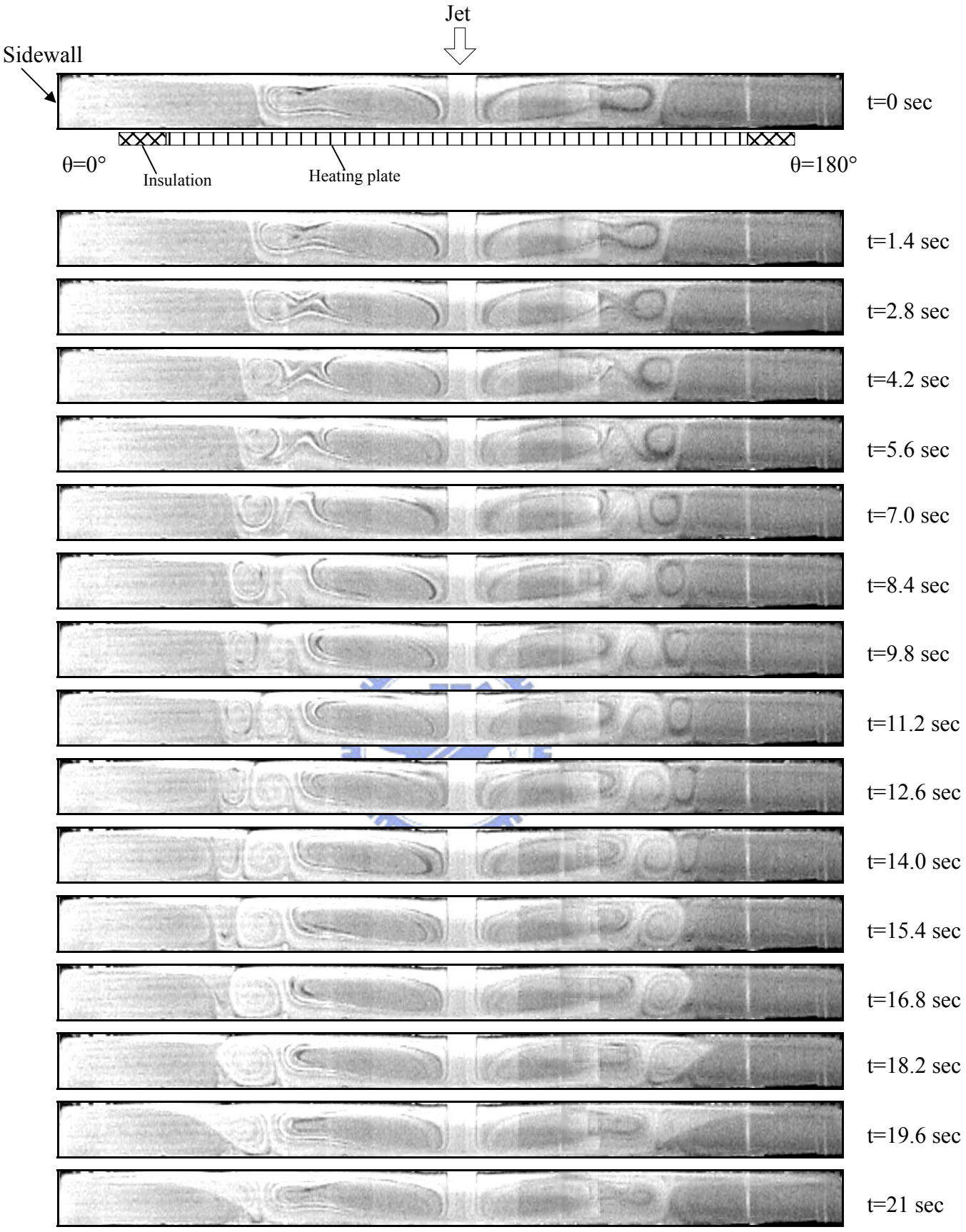

Fig. 4.57 Time-periodic vortex flow for H=20.0 mm and Ra=11,270 ($\Delta T = 15.0$℃) at Re_j=135 (Q_j=1.0 slpm) illustrated by side view flow photos taken at the vertical plane $\theta = 0°$ & 180° at selected time instants in a typical periodic cycle (t_p=21.1 sec).

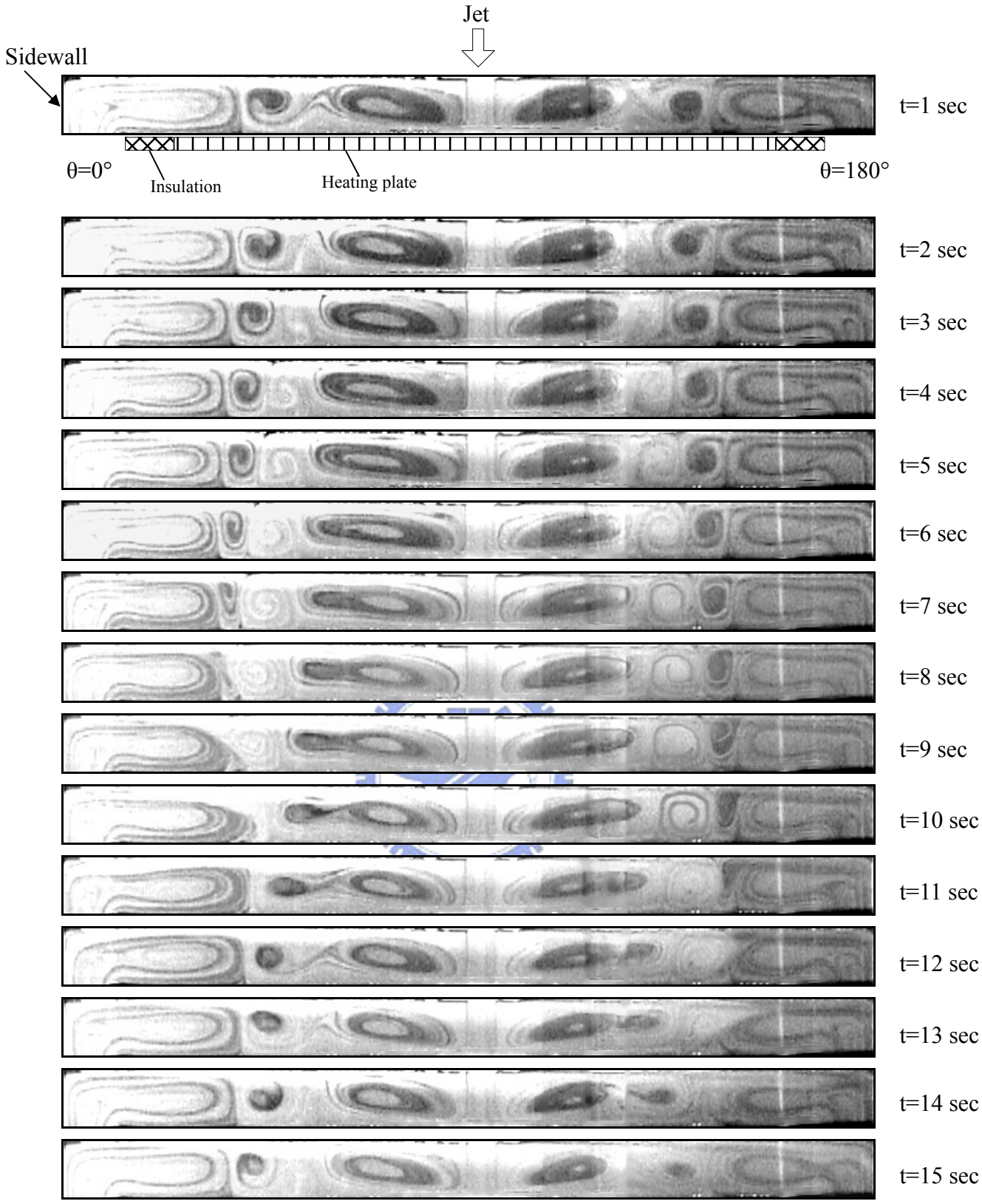

Fig. 4.58 Nonperiodic vortex flow for H=20.0 mm and Ra=15,030 ($\Delta T = 20.0$℃) at Re_j=135 (Q_j=1.0 slpm) illustrated by side view flow photos taken at the vertical plane $\theta = 0°$ & 180° at selected time instants in the statistical state.

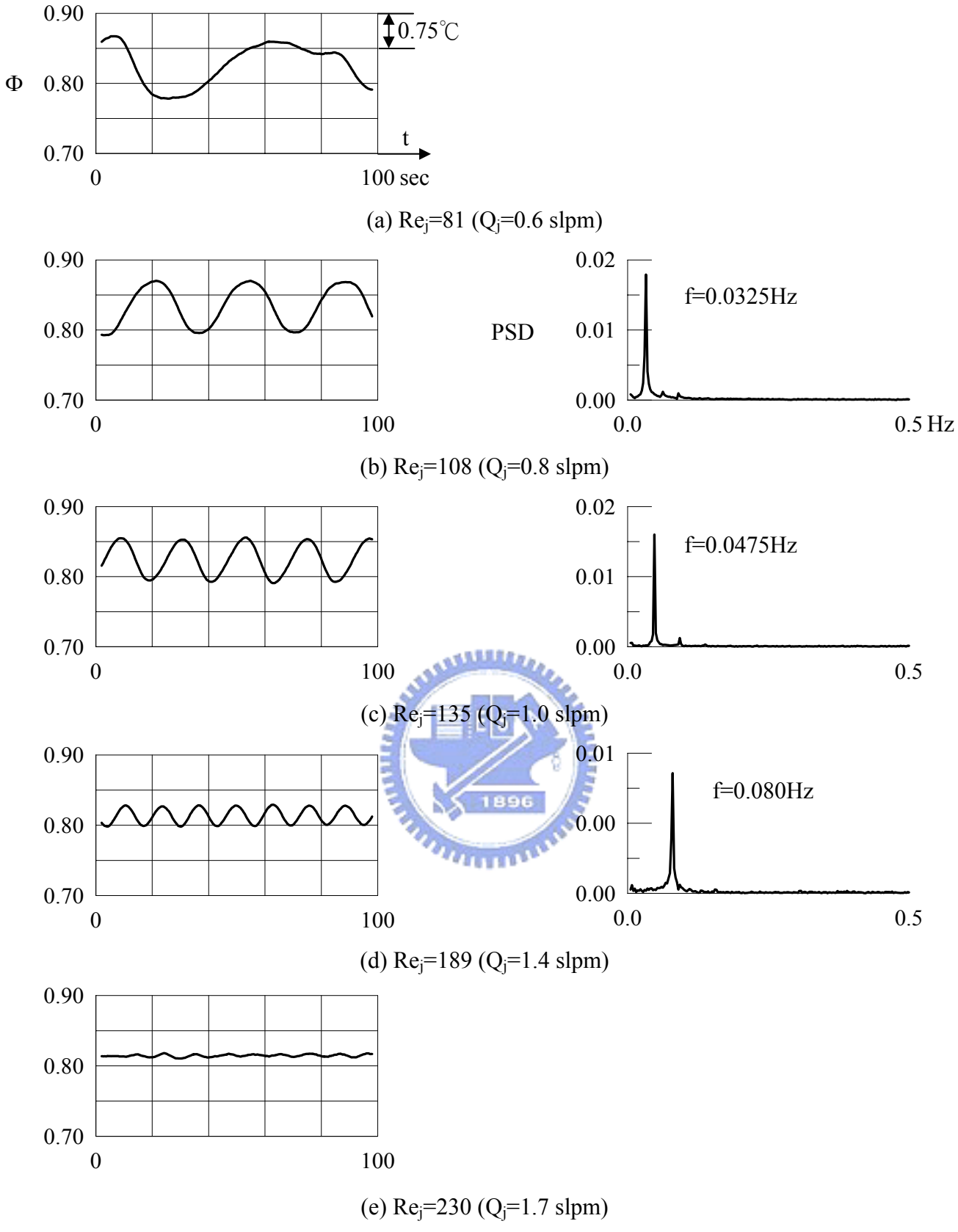

Fig. 4.59 The time records of non-dimensional air temperature and the corresponding power spectrum densities for Ra=11,270 ($\Delta T = 15.0$ ℃)at location (R, Z)=(0.52, 0.5) for $\theta = 0°$ with H=20.0 mm for various Reynolds numbers Re$_j$= (a)81, (b)108, (c)135, (d)189 and (e)230.

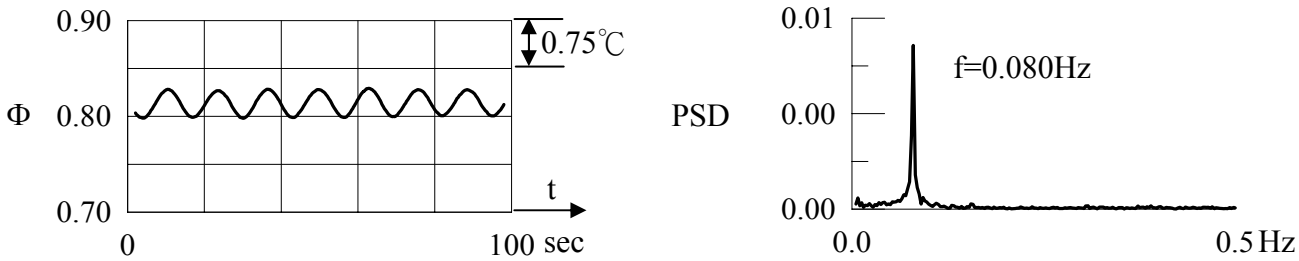

Ra=11,270 ($\Delta T = 15.0$ ℃) & Re_j=189 (Q_j=1.4 slpm)

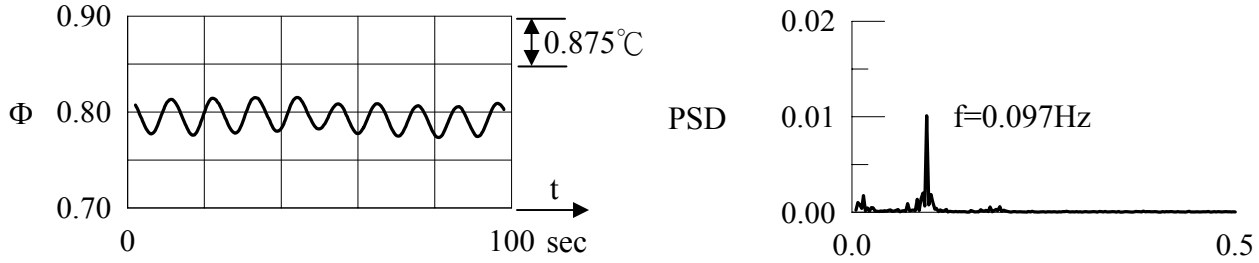

Ra=13,150 ($\Delta T = 17.5$ ℃) & Re_j=189 (Q_j=1.4 slpm)

(a)

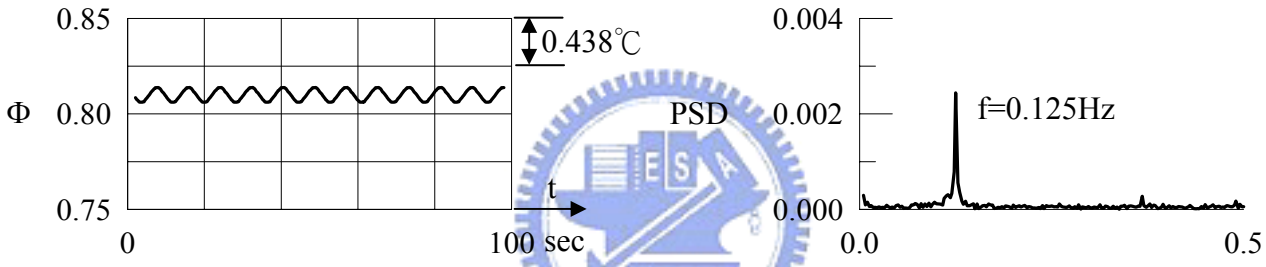

Ra=13,150 ($\Delta T = 17.5$ ℃) & Re_j=257 (Q_j=1.9 slpm)

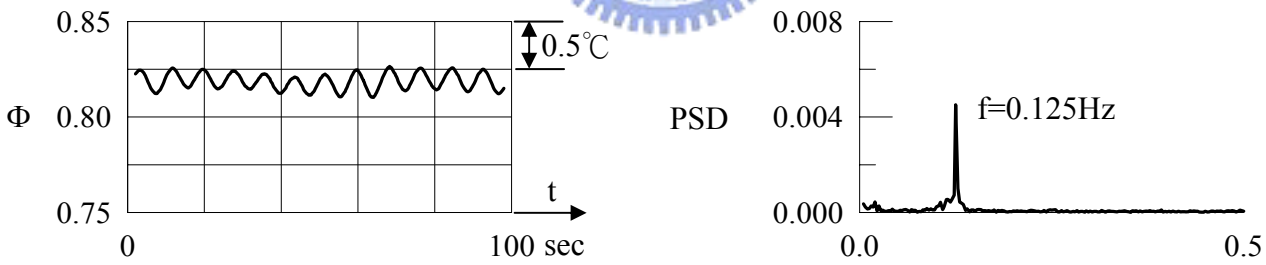

Ra=15,030 ($\Delta T = 20.0$ ℃) & Re_j=257 (Q_j=1.9 slpm)

(b)

Fig. 4.60 The time records of non-dimensional air temperature and the corresponding power spectrum densities for fixed Re_j for various Rayleigh numbers with H=20.0 mm at location (R, Z) = (0.52, 0.5) on the vertical plane $\theta = 0°$.

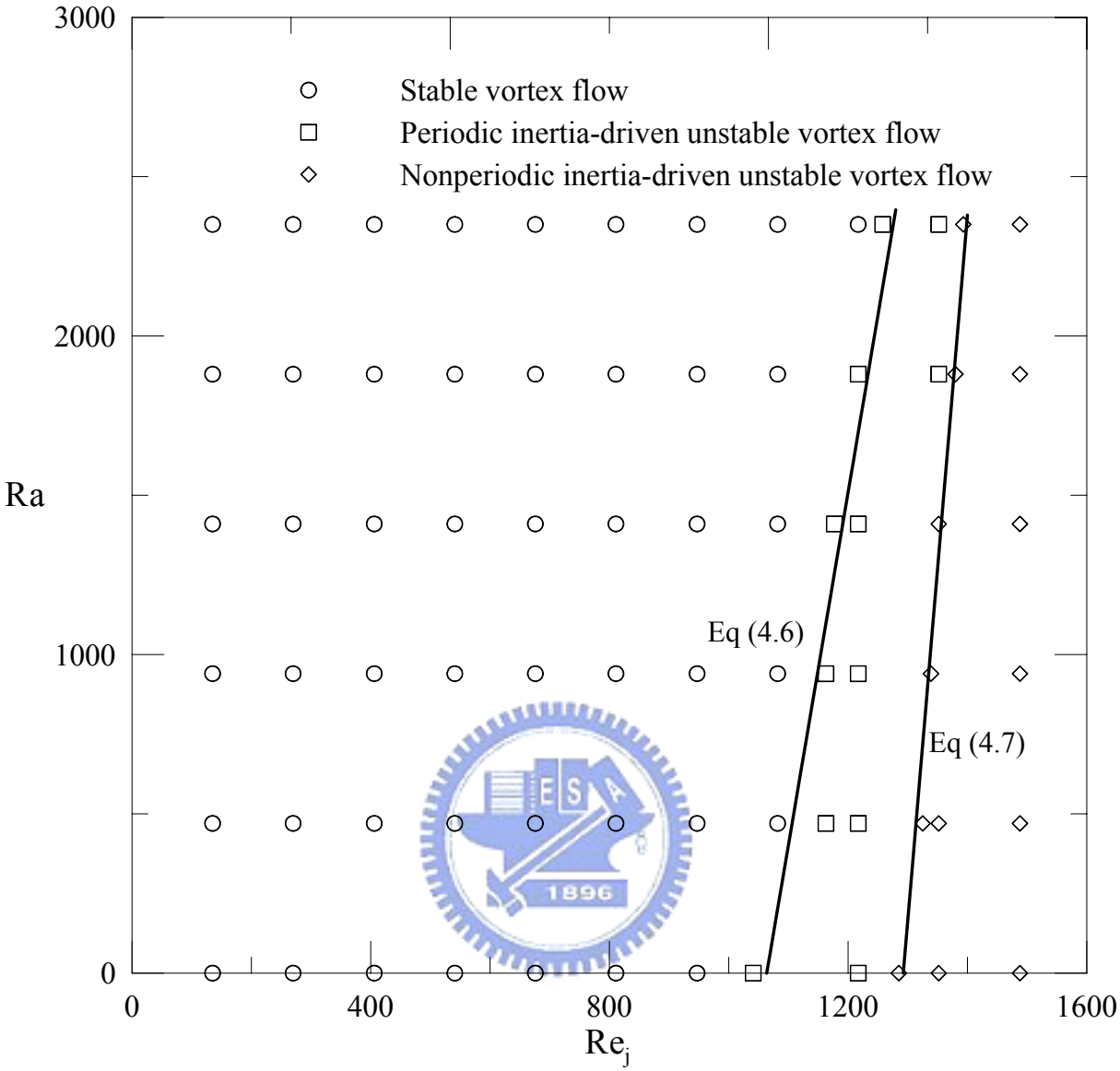

Fig. 4.61 Flow regime map delineating the temporal state of the vortex flow for H=10.0 mm.

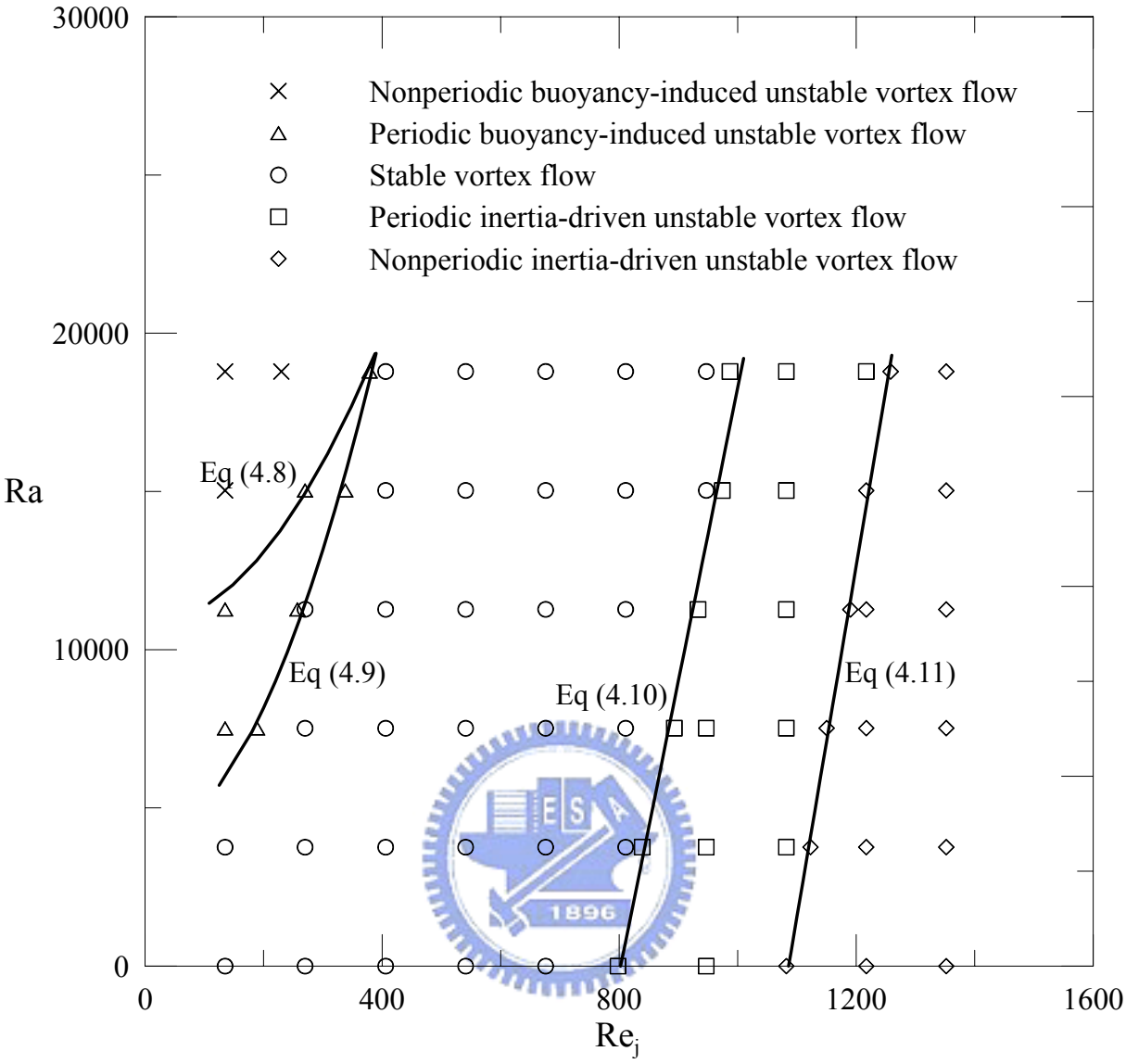

Fig. 4.62 Flow regime map delineating the temporal state of the vortex flow for H=20.0 mm.

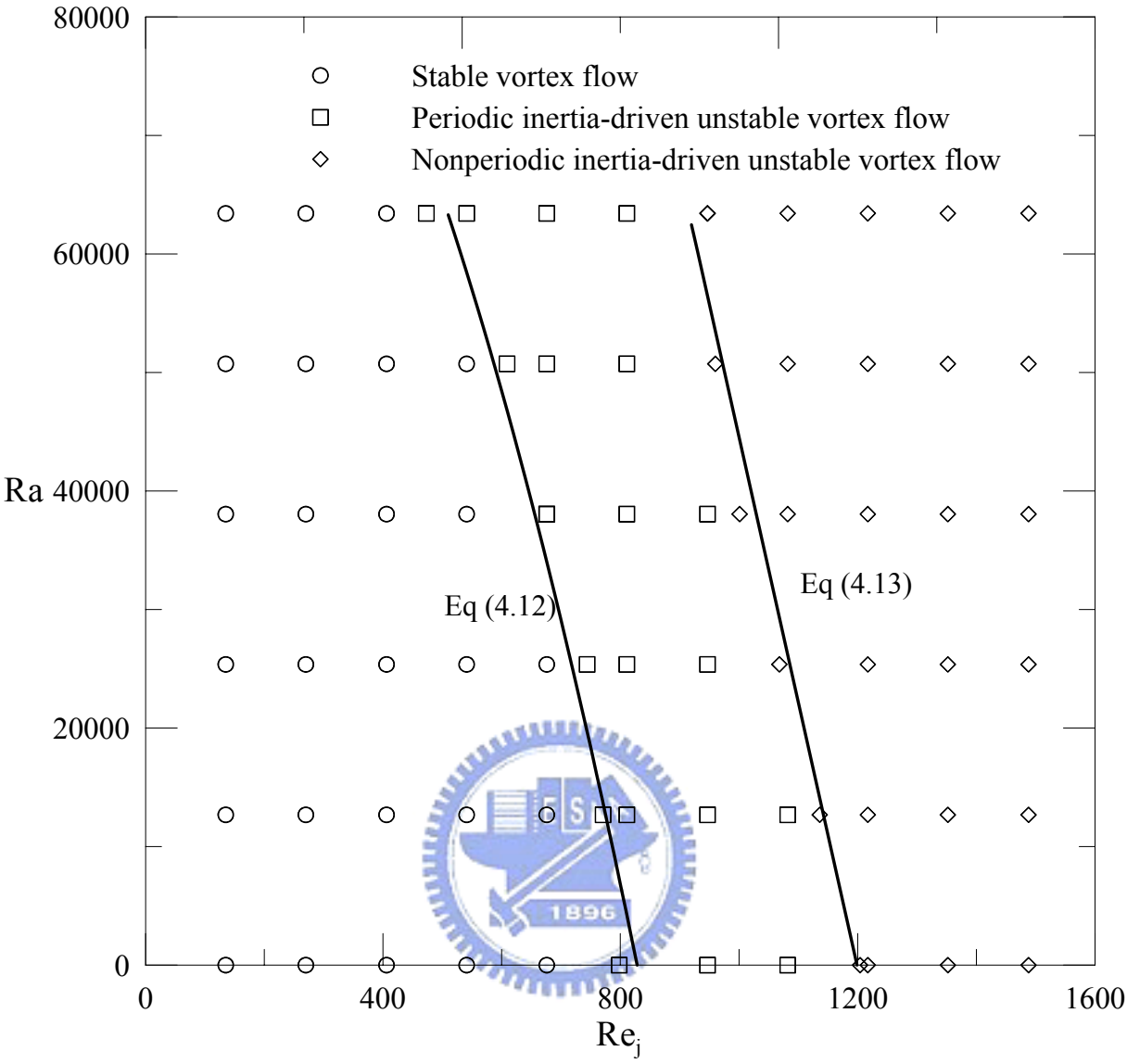

Fig. 4.63 Flow regime map delineating the temporal state of the vortex flow for H=30.0 mm.

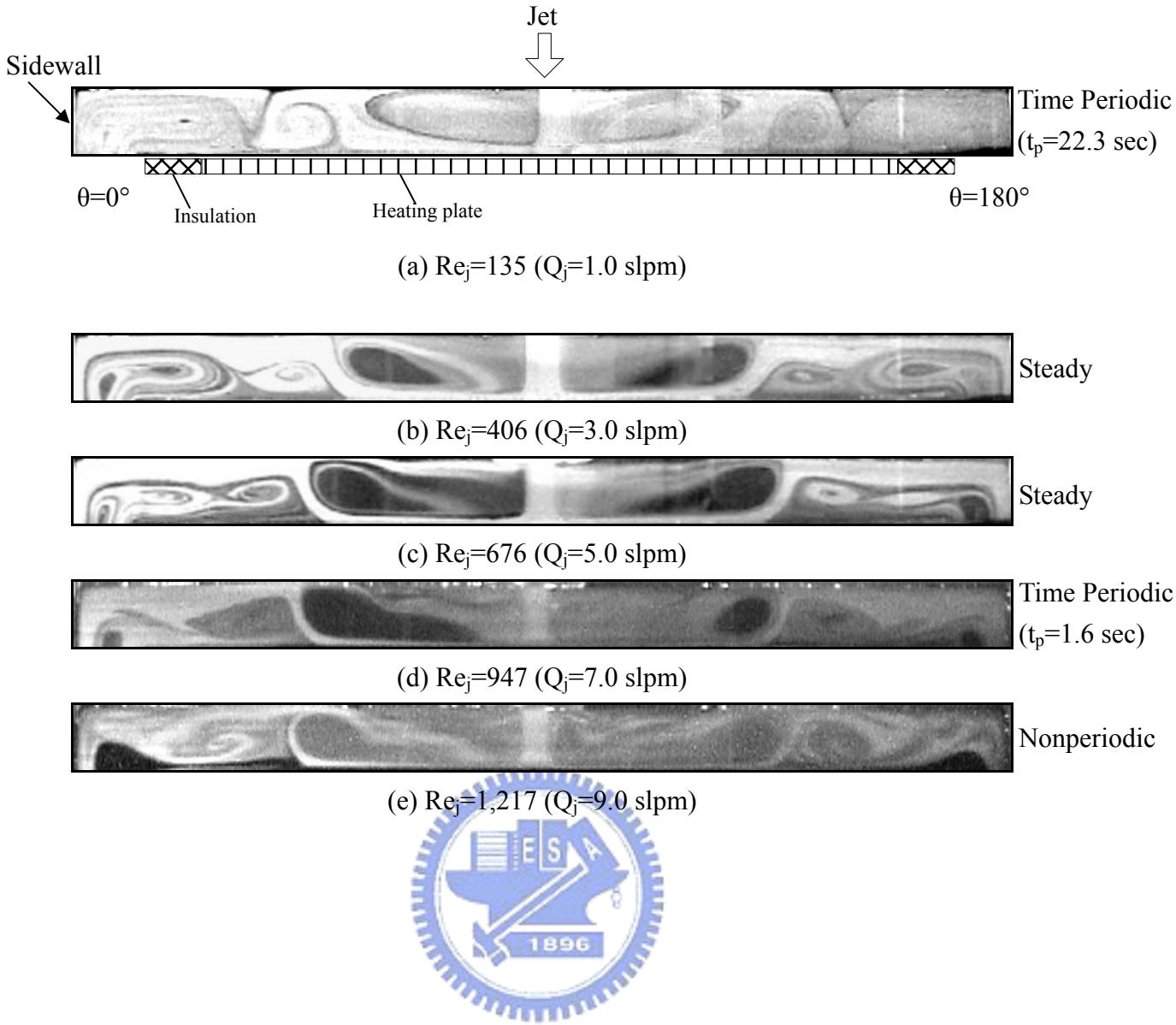

Fig. 4.64 Side view flow photos taken at the cross plane θ=0° & 180° at steady state or at certain instants in the statistical state for Ra=7,520 (ΔT=10.0℃) for various Re_j at H=20.0mm.

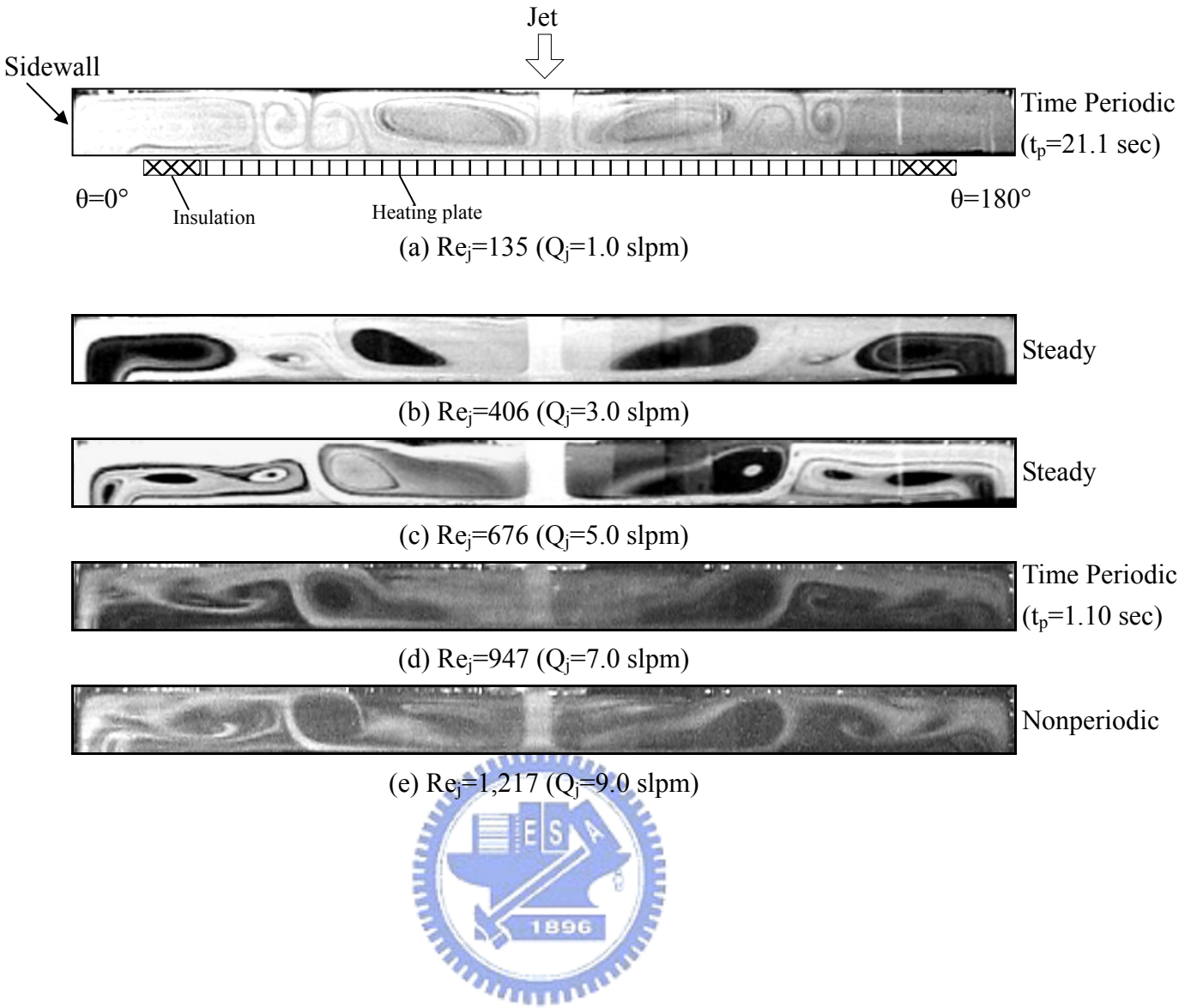

Fig. 4.65 Side view flow photos taken at the cross plane θ=0° & 180° at steady state or at certain instants in the statistical state for Ra=11,270 (ΔT=15.0℃) for various Re_j at H=20.0mm.

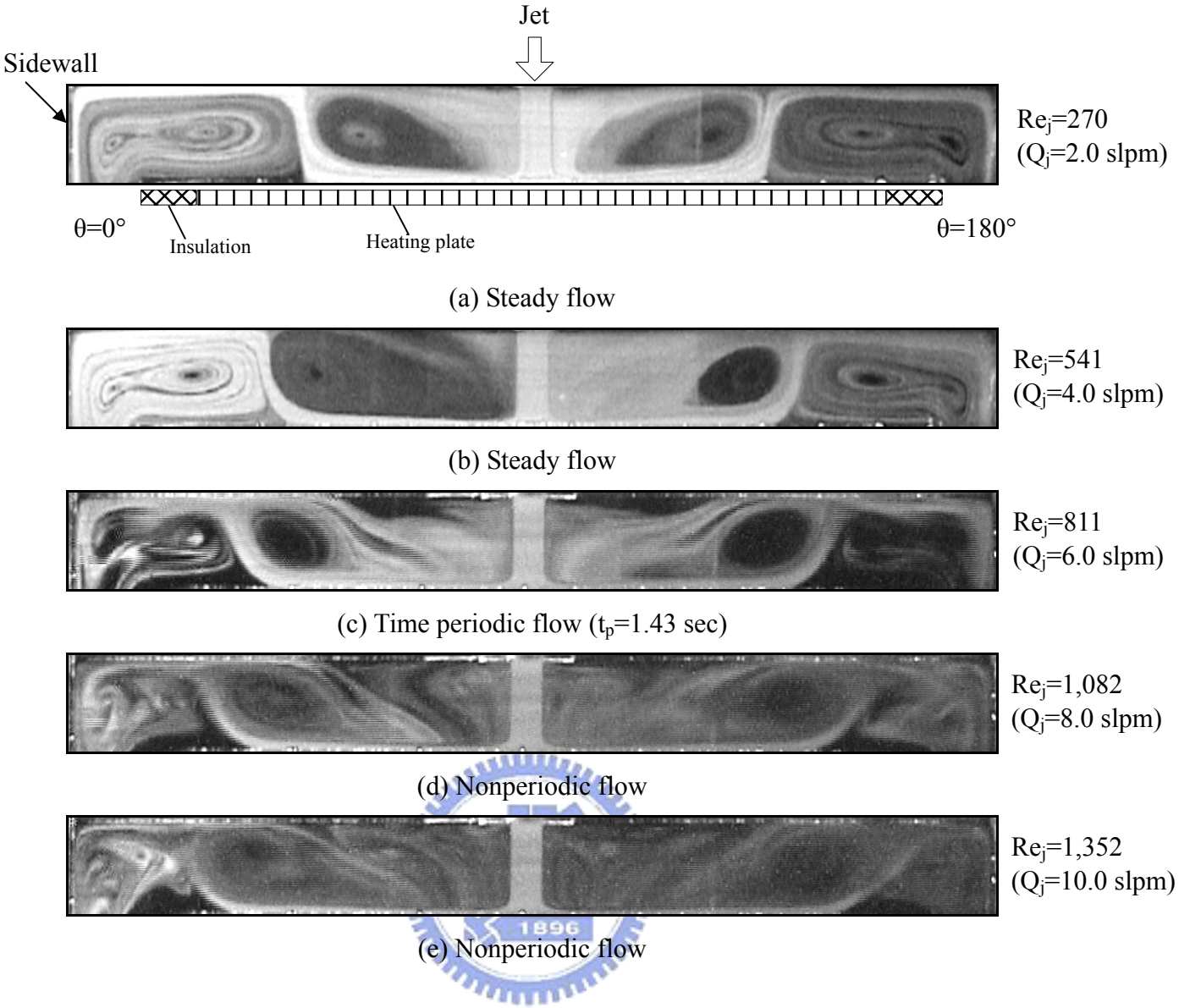

Fig. 4.66 Side view flow photos taken at the cross plane θ=0° & 180° at steady state or at certain instants in the statistical state for Ra=25,370 ($\Delta T = 10.0$℃) for various Re$_j$ at H=30.0mm.